Surface Finish on A356-T6 Cast Parts using Additive Manufactured Sand Molds

by

Caitlyn Rodomsky

Submitted in Partial Fulfillment of the Requirements

for the Degree of

Master of Science

in the

Mechanical Engineering

Program

YOUNGSTOWN STATE UNIVERSITY

May, 2018

Surface Finish on A356-T6 Cast Parts using Additive Manufactured Sand Molds

Caitlyn Rodomsky

I hereby release this Thesis to the public. I understand that this **Thesis** will be made available from the OhioLINK ETD Center and the Maag Library Circulation Desk for public access. I also authorize the University or other individuals to make copies of this thesis as needed for scholarly research.

Signature:

_____
Caitlyn Rodomsky, Student   Date

Approvals:

_____
Dr. Brett Conner, Thesis Advisor   Date

_____
Dr. Jason Walker, Committee Member   Date

_____
Dr. Virgil Solomon, Committee Member   Date

_____
Dr. Salvatore A. Sanders, Dean of Graduate Studies   Date

ABSTRACT

The objective of this research is to determine if surface finish influences the mechanical properties of cast heat treated aluminum (A356-T6). Binder jetting of sand allows for complex molds to be designed and printed to decrease the amount of time, cost and material. This project is separated into three phases. First phase of the project is the development of a benchmark casting and evaluation of surface roughness. In this phase, the surface finish of several angles of print orientation were compared. Certain angles produced a very noticeable stair step feature. Second phase of the project characterizes the static tensile and fatigue properties of A356-T6 cast flat bars from molds of four print orientation angles (0°, 5°, 15°, 30°). Lastly, the third phase of the project is fluid penetrant inspection (FPI) testing. The intent of this phase is to determine if stair step features would affect the outcome of this common nondestructive evaluation process.

Table of Contents

List of Figures

List of Tables

1.0 Introduction

1.1 Additive Manufacturing

Additive manufacturing often referred to as 3D printing is a relatively new manufacturing approach. 3D printing allows for production of three-dimensional parts using computer aided design (CAD) software. Additive manufacturing allows for complexity, customization and low volume of all parts [1]. Complexity specifies the intricacy of the part's geometry or the complexity in manufacturing the part. Customization allows for parts to be made directly without a lot post-processing and made for one specific purpose. With the aid of the tools above, additive manufacturing decreases cost of parts since it produce parts that are near net-shape. Using complexity with 3D printing capabilities, a once multiple piece part assembly can be printed as one part.

There are multiple types of material used in additive manufacturing to construct parts. A few examples are sand, plastics, and metals. Within additive manufacturing, there are seven different processes categories [2]. These categories consist of Vat photopolymerization, material jetting, binder jetting, material extrusion, powder bed fusion, sheet lamination and directed energy deposition. The method used in this study is binder jetting.

Binder jetting is a layer by layer process that involves two different types of consumables. These materials consist of a powder based material and a liquid binder. The binder material operates as a glue-like substance between layers of the power base material. When using binder jetting for sand printing, the sand is spread uniformly over the build volume or previously sand layer by a recoater. Next, a furan binder is placed where the part interconnects the sand layer by using an inkjet head spray. As multiple layers of sand

are placed on one another, the build volume lowers in the negative z-direction to construct the part. This method is repeated until the part is complete [3]. After completion of sand printing, the part is extracted from the build box and unbounded sand. Binder jetting can also be used for metals, ceramics as well as plaster. But the main focus of this study is on sand printing.

Sand printing processes can be seen in the 3D printing machine designed and fabricated by ExOne called the S-Max. The S-Max is a sand printer which using IC-80 Oklahoma sand and a 371381 Eniroset 3D Jet Resin (International) Binder. The sand has an 83 grain fineness number (GFN) which is an average grain size of a granular material [4]. The build volume is 70.9 x 39.4 x 27.6 (l x w x h) inch. The printer including one job box, is 271. x 138.6 x 112.6 (l x w x h) inches and weighs 14,330 pounds. The build speed of the S-Max is 2.12 to 3.00 ft^3/h. The printer deposits a layer of sand that is 0.28 mm thick on the xy plane and before a build is started, three layers of sand is placed on the build plate. This constitutes that the parts do not adhere to the build plate and cause damage to it. The main purpose of the S-Max is to produce huge sand molds and cores for the casting industry.

1.2 Casting

Metal casting is a significant component of the manufacturing sector. Today in the United States, there are 1,978 metal casting facilities. The total amount of metal in global production in 2004 was 79.75 million metric ton. In 2008, the total amount of metal in global production was 93.45 million metric ton and in 2012 the total amount of metal was 98.27 million metric ton. Then in 2016, the global production in metal casting was 104.4 million metric tons which exceeded the previous years. This metal includes aluminum, iron, copper, steel, zinc, nickel, magnesium, cobalt, other nonferrous, superalloys, lead and

titanium. An increase in metal casting has arose in the last ten years and continue to increase in the years to come [5][6]. Casting allows for metal such as A356-T6 to be heated up to a molten metal state to be used in a casting pour and then allow to set to solidify into a solid metal state. A mold is used to direct and contain the molten metal geometry until it solidifies. These cast parts can be seen in automobiles, planes, trains, etc. This process dates back centuries and is still used frequently today.

The casting process is initiated with a design of a metal part which is often created in a CAD program. The gating system is also assembled in the drawing. A gating system as stated in [7], "leads the pure molten metal to flow through a ladle to the casting cavity, which ensures proper and smooth filling of the cavity". The gating system consists of a sprue, runner, gates, sprue basin, pour basin, and risers. The pour basin is located at the top of the gating system. This is where the molten metal first enters the mold. It has a larger diameter than the sprue to consume the molten metal and control the flow. The molten metal flows from the pour basin into the sprue. A sprue is a long funnel that conveys the molten metal into the mold. At the bottom of the sprue is the ceramic foam filter. A filter is used to remove any unwanted debris, gas or material from the molten metal to have a cleaner metal for casting to prevent inclusions in the part [8]. The sprue basin is used to catch any extra metal as the molten metal starts to enter the runner. Molten metal flows from the sprue and into the runner. The runner is normally tapered and has a rectangular cross section to decrease the flow and the material needed. Molten metal enter the casting through openings called gates. Risers are placed in the cope (i.e. the top) of the mold to ensure the part will fill completely. A riser operates as a basin to back fill the part with molten metal to account for shrinkage of the metal during the solidification process. Risers

can either be open or blind. An open riser is open to the atmosphere at the top of the cope to whereas a blind riser is not exposed to the atmosphere and therefore still contains a cavity within the mold [9]. Vents are used in casting to prevent air bubbles and gas pores from forming within the casting. Vents are channels open to the atmosphere that allow air bubbles and gases from the casting to escape and ensure a quality casting [10]. The open risers and vents aid in knowing when filling of the mold is complete since they open to the atmosphere.

Once the part with a gating system is constructed, a mold is designed that contains the cavity for the metal part. In most cases, a mold consists of a cope and a drag which are the top and bottom of a two part mold [11]. In some instances, the mold can consist of more than two parts to compensate for easy cleanout of the cavity. In this project, the mold is a three-part mold. Therefore, a cope and drag make up the top and bottom of the mold while the cheek is the in between piece. A core can be inserted into the drag of the mold to create holes and cavities within the final casting. Cores in this project are constructed from a sand mixture; however, they can also be ceramic or metal [7]. Cores aid in the fabricating single complex parts instead of having to weld multiple parts together [7]. Cores can also strengthen the cavity within the mold. The parting plane separates the cope and the drag. Multiple part molds with cheek(s) have multiple parting planes. The intersection of the parting plane with the casting is called the parting line. A parting plane enables the clean out of excess unbound sand from the mold. Clean out is necessary since the molten metal needs to be free of debris and loose material for a quality casting.

Once the mold is designed, the mold is manufactured using 3D sand printing. In this case, the mold is additively manufactured by the S-Max sand printer. Once a physical

mold is ready, the metal is melted in a furnace. When the molten metal reaches the pour temperature (which is higher than the melting temperature), it is ready to be poured into the mold containing the cavity of parts. After solidification occurs, the sand mold is broken, and the casting is complete. Post-processing on these parts is the same process taken for conventional casting. The gating system is machined off to have a finished cast part [12].

There are many different casting processes which include sand casting, plaster mold casting, die casting, investment casting, etc [12]. However, the focus of this project is sand casting. Sand casting is the process of constructing a sand mold that contains a cavity for the molten metal to be poured into and solidified for a casting part to be manufactured. Five steps are used to construct a complete sand casting. These steps include patternmaking, core making, molding, melting and pouring and cleaning [13]. Patternmaking is the process of using material such as wood or plastic to form the outer perimeter of the cast part. The pattern must account for the shrinkage of the metal during solidification. The interior cavity of the cast part is designed using a core. A core is used to resemble the interior of a part where molten metal would be displaced [14]. A core is formulated by using a core box technique where sand is mixed with resin binders to develop the core. Then the core is blown into a core box and allowed to set and harden to form a strong constructed core [15]. Once the patternmaking and core process are complete, a mold is designed using the cope and drag features. The cavity is formed by inserting the pattern into the mold and packing sand around it. The core is inserted into the drag if needed. Once the cavity of the part is developed, the gating system is placed within the mold. The gates and runner are placed in the drag while the sprue is placed in the cope.

After this process is complete, the cope is placed on top of the drag and clamped together so that no extra molten metal flows out of the mold [7]. Metal is then heated up to its liquid form to be poured into the mold containing the cavity. Then the metal is contained in the mold until it is completely solidified. After solidifying, the casting is removed from the sand mold by a process called shakeout. The cleaning process pertains to machining the gating system from the cast part [7].

Three-dimensional (3D) sand casting is a recent development in the casting world. The process of 3D sand casting is the same as the conventional sand casting. However, instead of a pattern being constructed and inserted into the sand mold to form the cavity, the mold containing the cavity is designed in a CAD software and then additively manufactured using a 3D sand printer to reduce the number of steps in the process. It saves time and reduces cost by eliminating hard patterns and core boxes. It allows for intricate castings to be designed without a lot of post processing taking place. 3D sand casting is utilized for low volumes of parts that need to be rapidly cast and contain multiple sets of detail in the design. 3D sand casting eliminates the physical storage of the molds. Since 3D sand molds and cores are designed using a CAD software, they can be stored on a hard drive and accessed when needed rather than hard tooling taking up space in the storage area in a foundry.

To maximize new methods in casting, ExOne developed a large sand printer to 3D print sand molds and cores to be used in a foundry to assist in metal casting. This sand printer is known as the S-Max which can be seen below in Figure 1.

Figure 1: ExOne S-Max Sand Printer

An S-Max can contain two build boxes to improve efficiency. While one box is used for printing, the other box can be cleaned out. This printer can print large sand molds and cores. The build volume is 70.9 x 39.4 x 27.6 in (l x w x h) and the printer weights 14,330 lbs. This S-Max prints layer by layer which means that a layer of sand is placed on the build box x-y coordinate system. Then binder (furan) is jetted to location of the part. A full layer of binder is not placed on the layer of sand but only where the part was placed in the build box. The furan binder is only used in the layer by layer process of the binding of the part and not of the entire build box. Binder acts like glue holding the sand in place for the part. Furan binder does not need any further heating for the curing process since it cures at room temperature. After the binder is placed on the sand layer, another sand layer is place onto that until it is built up in the z-axis and the part is formed. Once the build is complete, a vacuum is used to clean out the loose sand in the build box and the parts are removed and loose sand is brushed off the part [16]. Utilizing this type of additive manufacturing allows for intricate geometries to be cast from complex sand molds and cores.

1.3 Material A356-T6

A heat-treatable aluminum alloy is used in this study. This alloy is known as A356-T6. A356 is a standard aluminum casting alloy. The A356 alloy designation is given by the U.S Aluminum Association (AA). The AA created a system to organize multiple variations of different aluminum alloys. The numbering system formulated by the AA is called "Pink Sheets" which contain a three-digit numbering system including one decimal place to distinguish from these aluminum alloy variations. A three-digit number without the decimal place is categorized as a casting in which it means that this aluminum alloy can be used for the casting process. However, many alloys contain the same three-digit number. But by placing a letter in front of the three-digit number differentiates between a slight chemical makeup of the alloy compared to the other alloys using the same three-digit numbering system. This difference in composition can change the casting and mechanical properties of a part [17].

The aluminum A356 chemical composition is comprised of 0.25 copper (Cu) max, 0.20 to 0.45 magnesium (Mg) max, 0.35 manganese (Mn) max, 6.5 to 7.5 silicon (Si), 0.6 iron (Fe) max, 0.35 zinc (Zn) max, 0.25 titanium (Ti) max, 0.05 other (each) max and the balance is aluminum. Aluminum A356 mechanical properties consist of 0.2% proof stress of 185 (N/mm), tensile stress as 230 (N/mm), elongation as 2%, brinell hardness as 75, endurance limit as 56, modulus of elasticity as 71 and shear strength as 120. The density of A356 is 2.685 g/cm, the specific heat is 963 (J/kg), and the latent heat of fusion is 389 (kJ/kg) [18].

The aluminum alloy has a face-center cubic (FCC) crystal structure as shown in Figure 2. A FCC crystal structure is visualized as a single rectangular structure in which atoms are placed on all eight corners and then an atom in all centers of each square which can be seen below in Figure 2.
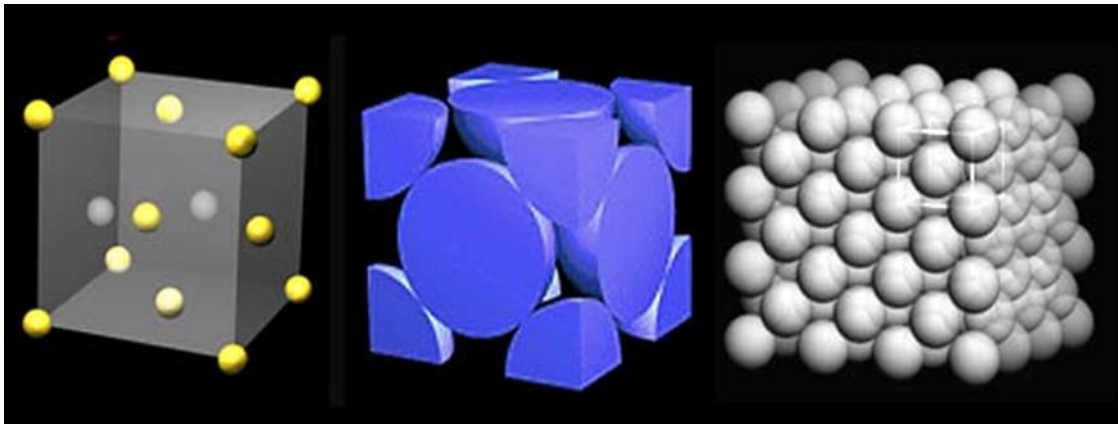
Figure 2: FCC Crystal Structure [19]

These atoms are closely packed together and has a packing factor of 0.74 [20]. A phase diagram can be seen below in Figure 3 [21].
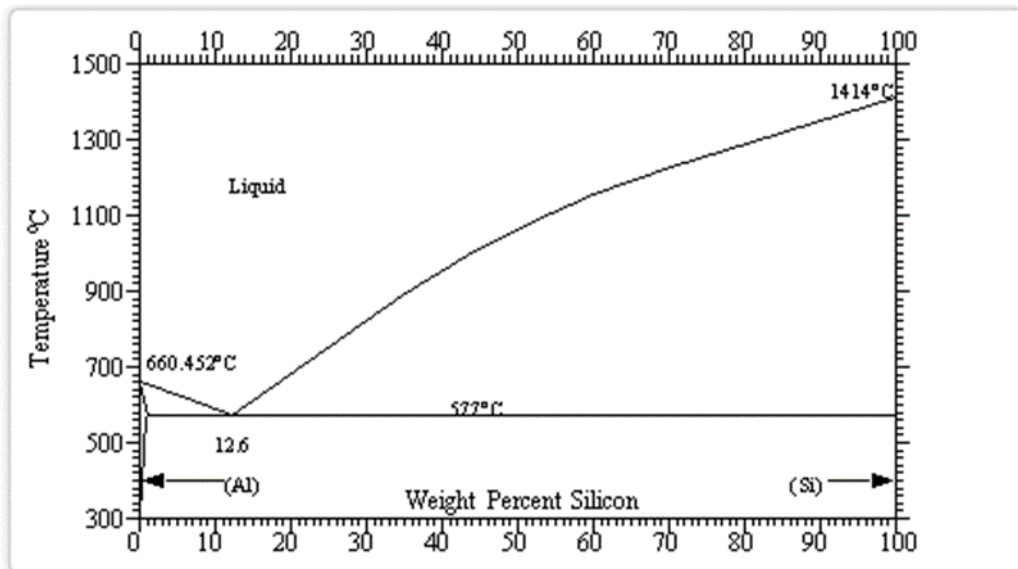
Figure 3: Phase Diagram of A356-T6

An aluminum-silicon phase diagram is shown in Figure 3. A356 is an aluminum silicon alloy. The phase diagram demonstrates the different phases (liquid and solid phases) of A356 and the temperatures in which these phases occur. The phase diagram is a binary phase diagram that demonstrates a solid solution of silicon in aluminum, solid solution of aluminum in silicon and then a liquid phase as well as three two-phase regions. The liquidus temperature of A356 is 615 degrees Celsius and the solidus temperature is 555 degrees Celsius.

The heat treatment process of an aluminum alloy improves the mechanical properties of the cast part. Sand casting is one of two casting processes that can be heat treated after pour. This is because it requires less post-processing and the cast part can be used in the as-cast condition. T6 is categorized as the temper of the type of aluminum alloy. As stated, "solution treat and age artificially. In castings, T6 commonly describes optimum strength and ductility" [17]. This heat treatment process consists of three different phases: solution, quench and age. The solution phase comprises of the casting be heated back up to the eutectic temperature to create a solid homogeneous solution. This eutectic temperature can be seen on the phase diagram at roughly 577 degrees Celsius. It is located approximately between the liquidus and solidus temperatures. The next phase of the heat treatment process is quenching. Quenching is the process of taking the casting that was recently heated up to the eutectic temperature and immediately cooling it mainly in a water bath which allows for the solution to stay at room temperature. The last step in the heat treatment process is aging. This is as it states, letting the casting naturally age with time and cool down to increase the hardness and strength of the casting.

1.4 Surface Roughness

The surface roughness of the casting affects the mechanical properties and appearance of the casting. In general, surface roughness can influence the fatigue performance of the casting. Surface features can act as stress concentrators and act as locations for crack initiation. There are multiple surface profiles used to determine the characteristics of a part. They consist of the actual profile, measured profile, primary profile, roughness profile, and waviness profile. Each of the profile measures different parameters to understand the surface roughness of a part such as maximum height, average height, highest peak, skewness, root mean square tilt etc. of a given profile. The roughness profile can be described as "the profile resulting from electronic high-pass filtering of the primary profile with a cut-off wavelength. This process removes the longer wavelength components. The parameters are designated R and evaluated within the evaluation length ln, which generally consist of five sampling lengths lr. The sampling length corresponds to the cut-off wavelength of the profile filter" [22].

The main roughness metrics used in this study are the arithmetic mean roughness (R_a) and the root mean square height (R_q). The arithmetic mean roughness as stated by Keyence "indicates the average of the absolute value along the reference length" which demonstrates that the arithmetic mean roughness is the average roughness height value for a given length. The root means square height as stated by Keyence "indicates the root mean square along the reference length" which displays the standard deviation for the height of the profile for a given length.

Characterizing the surface roughness of a cast part especially the arithmetic mean roughness and the root mean square height could help to better understand the mechanical properties of an A356-T6 casting. One method to achieve a low Ra and Rq value for

surface roughness of a cast part would be to add an extra step to machine, grind, or polish the surface. The machining step adds cost and time to the manufacturing process. It is important to understand when it is needed. Alternatively, what is the effect on mechanical properties if the surface is left as-cast. It should be noted that in complex casting geometries enabled by 3D sand printing such as lattices, it might be impossible to access surfaces for machining.

As will be shown in this report, there are unique surface features resulting from 3D sand printing that will affect the surface topology. Stair step features result from steps created in the mold during the layer-by-layer printing process. There is a need to determine the geometries when the stair step features are most prevalent, the adequately of existing surface roughness metrics to measure stair step features, mechanical properties, and whether the features impact the efficacy of common casting inspection methods.

1.5 Objective of Project

The project will utilize an ExOne S-Max 3D sand printer to produce molds and determine if surface roughness influences the mechanical properties of cast A356-T6. The purpose of this project is to determine if surface features from the additive manufacturing of molds will affect the static tensile and fatigue properties of cast A356-T6. The research will also determine examine the findings from dye penetrant inspection testing on flat bars containing sand printed surface features.

The objective of the project is to determine if the surface roughness influences the mechanical properties of a casting using additively manufactured sand printed molds. The following research questions will be addressed in this project:

1.) What are the surface features of the casting that are associated with the printing angle? Can we quantify the surface roughness as a function of printing angle?

2.) What is the effect of the printing angle of the static tensile and bending fatigue properties of the casting?

3.) Do surface features affect the detectability of linear defects using fluorescent penetrant inspection (FPI) testing?

2.0 Literature Review
2.1 Heat Treatment

Within the heat treatment process, there lies certain temperatures and length of time to carry out an acceptable process. This process is rather expensive since the heat treatment process tends to span a length of time. A study was conducted by Mooler, Govendar and Strumpf in *The T6 Heat Treatment of Semi-Solid Metal Processed Alloy A356*. The study examines cast steel plates (4 mm x 80 mm x 100 mm) in which was heat treated at a temperature of 540 degrees Celsius with varying time of 30 minutes up to 6 hours. The increments of time were broken up into 30 minutes, 1 hour, 2 hours, 4 hours, and 6 hours. Next step in the process was to quench the casting. This was done by a water bath at 25 degrees Celsius. The last step of the process was the aging in which was artificially aged at temperature variation of 160, 180, and 190 degrees Celsius. Because of this study, it was found that since artificially aging was used, that the longest time to heat treat the casting at 540 degrees Celsius is between one to two hours. After two hours, the casting starts to lose it hardness and strength properties. However, the artificial aging between the temperature variation is determined by Arrhenius-type equation. These equations define the maximum artificially aging time to determine best results of the mechanical properties for the casting. [23]

Another study that exhibits a heat treatment process is contained in *Fatigue behavior of A356-T6 aluminum cast alloys. Part I. Effect of casting defects* by Wang,

Apelian and Lados. This examines not only heat treatment on aluminum alloys but also portrays the fatigue behavior of a heat-treated cast part. These fatigue properties rely upon the chemical makeup of the heat-treated aluminum alloy and its defects. This material is A356, however, it contains 0.4% Mg more than what is contained in an original chemical compound of A356-T6. Next, a pour was performed with two different types of molds, a steel wedge mold and an end-chill sand mold. Both molds provide samples for fatigue testing. The test specimen size was 13 mm x 13 mm x 127 mm. Once the casting was complete, it was heat treated using a T6 temper. This constitutes a 540° C heat treatment solution for 10 hours and then quenched at room temperature. The heat treatment solution took place in an air circulated furnace while the quenching took place in a water bath. Next, the casting was naturally aged for 20 hours at room temperature and then artificially age for six hours at 170° C. [24]

Within the Effect of solidification cooling rate on the fatigue life of A356.2-T6 cast aluminum alloy carries out the procedure of a heat treatment process. The test specimen used are cast aluminum alloy ingots for reciprocating-bending, high-cycle axial and low-cycle axial fatigue testing. The ingots were cut into thin pieces each of which were 4mm thick. To contain an as-cast surface during the heat treatment process, the flat surface of the ingot was placed downward. To constitute a T6 temper, the thin ingot pieces were heat at 540° C for twelve hours. Next, the ingot pieces were placed in a water quench at 71° C and then lastly, aged for 4 hours at 155° C. [24]

2.2 Bending Fatigue

As demonstrated in *Fatigue Behavior of A356-T6 aluminum cast alloys. Part I. Effect of casting defects* by Wang, Apelian and Lados, bending fatigue took place on test specimens of standard E455 ASTM that contained round bar geometry. These samples

had a parallel gauge section of 20 mm long with a 7.6 mm diameter. The test specimens were machined and polished at Westmoreland Mechanical Testing and Research prior to fatigue testing. Then the fatigue test specimens were evaluated in a servo-hydraulic Instron (8511) machine. A load frequency of 55 Hz was placed on the fatigue specimens under pull-pull and pull-push loading. The two stress amplitudes used were 70 and 100 MPa and the stress ratios used were 0.1, 0.2, -1. The configuration of the machine on the round bar test specimens is a ASTM E 1012-99 standard. Qualitative and quantitative metallographic analysis was done on the test specimens. Then using a scanning electron microscope, microfractographic examination was conducted on these specimens as well. In conclusion to this study, fatigue life as well as the critical defect size are the most detrimental to fatigue properties of A356-T6. The critical defect sizes caused stress concentration on the surface of a casting which then caused a fatigue crack at that point. This also included the porosity of the casting which lead to most of the defects on the surface. The fatigue life depended on where that crack initiates in comparison to what kind of crack is formed. [24]

To have a better understand of fatigue properties of an aluminum cast heat-treated alloy (A356-T6), *Effect of friction stir processing conditions on fatigue behavior and texture development in A356-T6 cast aluminum alloys* by Tajiri, Uematsu, Kakiuchi, Tozaki, Suzuki and Afrinaldi was examined. This study conducts A356-T6 under friction stir processing to reshape the heat-treated aluminum alloy to better function under fatigue loading. The test specimens were a modified E466 ASTM standard which can be seen below in Figure 4.
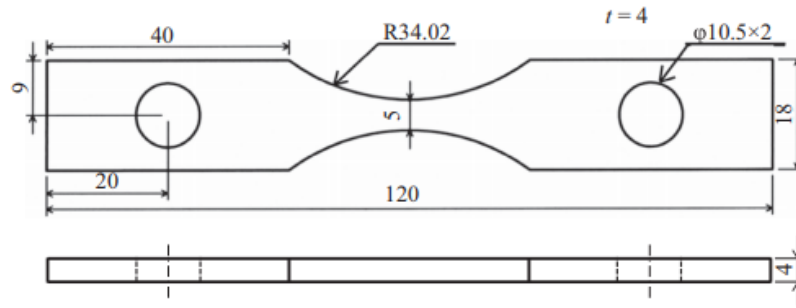
Figure 4: Modified E466 ASTM Standard Test Specimen

These parts were then machined, and the gauge area was mechanically polished before the bending fatigue testing took place. A SIMADZU TB-10 plane bending fatigue machine was used to conduct the testing of the material containing the friction stir processing and the as-received material. The frequency used on both testing was at 33.3 Hz with a load ratio of -1. An S-N curved was formulated from the data pulled from the plane bending fatigue testing of the friction stir processing material as well as the as-received material. This demonstrated that during high cyclic fatigue loading, the material containing the friction stir processing produced higher stress amplitudes per number of cycles to failure compared to that of the as-received material which contained lower results. In conclusion, the defects on the cast surface was reduced with the friction stir processing of A356-T6 as well as the fatigue properties of this material. [25]

The solidification process during the casting procedure has an affect on the fatigue life of a cast aluminum alloy. A study conducted by B. Zhang, W. Chen, and D. R. Poirier examines the *Effect of solidification cooling rate on the fatigue life of A356.2-T6 cast aluminum alloy*. This paper analyzes cast aluminum ingot test specimens used for reciprocating-bending fatigue testing. This specimen can be found below in Figure 5.
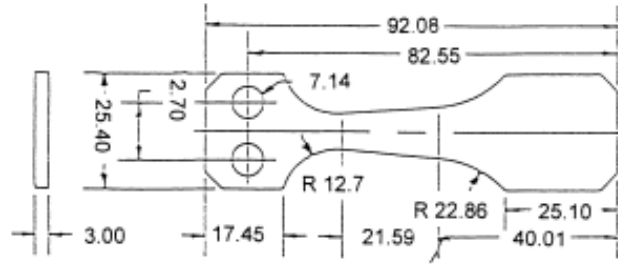
Figure 5: Cast Aluminum Ingot Test Specimen for Reciprocating-Bending Fatigue Testing

The parameters used for the reciprocating-bending fatigue testing are as follows. For a load frequency of 20Hz, a strain ratio of R=-1 and R=0.15 was used. The strain ratio of R= -1 is a completely reverse strain ratio applied with the load frequency for this fatigue testing. Also, a load frequency of 25Hz was applied with a strain ratio of R=0.1. The strain ratio of R=-1 contained an adjusted maximum strain for low and high cyclic fatigue testing. For a low fatigue testing with strain ratio of R= -1, the adjusted maximum strain of 0.004 was used and for a high fatigue testing of strain ratio of R= -1, the adjusted maximum strain of 0.0016 was used. Then for low fatigue testing with strain ratio of R=0.15, an adjusted strain of 0.0082 was used and for high fatigue testing with strain ratio of R=0.1, an adjusted strain of 0.0016 was used. These results can be seen below in Figure 6.
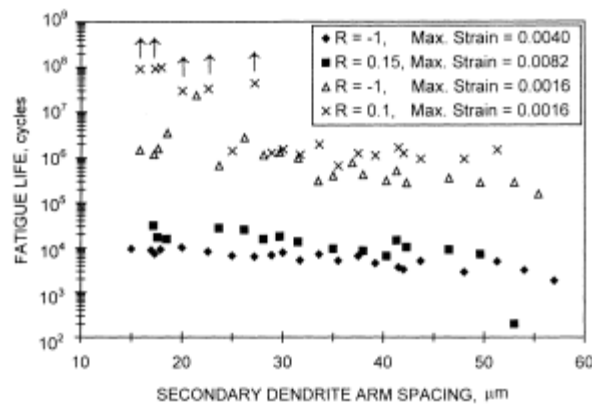
Figure 6: Fatigue Life vs. Secondary Dendrite Arm Spacing

17

This chart demonstrates that for R=-1 with maximum strain of 0.004 and R=0.15 with maximum strain of 0.0082, both have the lowest fatigue life per secondary dendrite arm spacing. For an increase in fatigue life per secondary dendrite arm spacing, a strain ratio of either R=-1 with maximum strain of 0.0016 or R=0.1 with maximum strain of 0.0016 must be used. [26]

Plane bending fatigue testing can be performed on test specimens to determine the fatigue life of a part. This can be seen in a study called *Fatigue crack paths and properties in A356-T6 aluminum alloy microstructurally modified by friction stir processing under different conditions* by A. Tajiri, Y. Kakiuchi and Y. Suzuki. This paper examines the fatigue life of a cast heat treated aluminum alloy. It is determined that a fatigue crack is directly related to the casting defects on or within the cast part. This yields to minimize the life span of a cast part and can be tested using plane bending fatigue testing. It is noted that the fatigue life can be improved using the friction stir processing technique which aids in the strengthening of the material properties of the alloy before testing. During the experimental procedure of this study, the gauge section of the cast ingots was polished using a #2000 grade emery paper and then buffered for a finer finish. The paper consisted of three different test parameters for the given testing. This contained a low strain specimen (L), a high strain specimen (H) and an as cast specimen after the friction stir processing took place. The plane bending fatigue testing was performed on a SIMADZU TB-10 machine under a load frequency of 33.3Hz and a load ratio of R=-1. Along with the plane bending fatigue testing, a hardness test was also conducted. This hardness test was performed on a micro-Vickers hardness tester for a load of 2.49 N and a dwell time of 30

seconds. The results of the plane bending fatigue testing can be found in an S-N curve below in Figure 7.
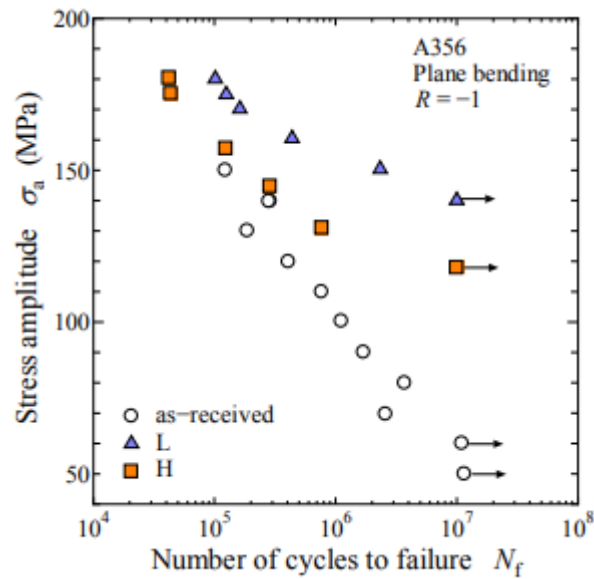
Figure 7: Bending Fatigue S-N Curve

From the chart above, the test specimens that contained friction stir processing had a larger stress amplitude compared to the as-cast parts. This means that the friction stir processing improved the fatigue life of the aluminum heat treated cast parts. In conclusion, this study demonstrated that friction stir processing eliminated most casting defect to produce a higher life span of the cast part. [27]

The fatigue life of a cast part is directly related to the casting defect on or within the part. This can be seen in a study by M. Avalle, G. Belingardi, M.P. Cavatorta, and R. Doglione called *Casting defects and fatigue strength of a die cast aluminum alloy: a comparison between stand specimens and production components*. The most detrimental defect in a casting is porosity. Porosity is used to describe a void or hole on or within the cast part. Porosity on a part is demonstrated as gas bubbles on the surface of the metal part and can be known to have gas bubbles entrapped within the part. To test this theory, this

study constructs different fatigue testing on different test specimens to illustrate how the casting defects pertain to the fatigue life. The material consists of an aluminum alloy which is EN AC-46000-UNI EN 1706 and is mainly found in automotive components. The first test specimen can be found below in Figure 8 for bending fatigue testing.
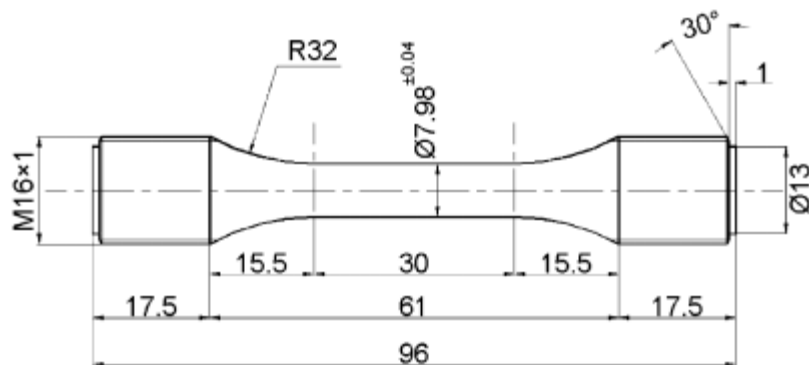
Figure 8: Bending Fatigue Test Specimen

These test specimens were tested as cast and the only post processing on this part was to minimize the flash on the part's surface. Bending fatigue testing was performed on these test specimens. This consisted of a cantilever rotating bending testing machine at a frequency of 100Hz and a fatigue strength of $2x10^6$ cycles. A second set of fatigue testing took place on test specimens pulled off the production line and can be seen below in Figure 9.

Figure 9: Test Specimens from Production Line

Again, there was no post processing on this part and was tested as cast. These cast parts were tested in a hydraulic testing machine at a frequency of 25Hz and a fatigue strength of $2x10^6$ cycles. The minimum load used for all testing (both bending and fatigue testing) was Pmin = 0.5 kN which was kept constant throughout testing. Another parameter for both testing (bending and fatigue testing) was the placement and dimensions of the sprue and runner in the gating system which consisted of three different designs of placement and three different parts tested for each bending fatigue testing and hydraulic testing. The different placement of the sprue and runner within the gating system arose other defects on or within the casting. It was assumed that this was caused from the location of the sprue relative to the part. The location of the sprue relative to the part caused different fatigue properties in relation to the porosity of the part. Mainly the fatigue testing, introduced the casting defects within the part. [28]

2.3 Fatigue

Today, metallic parts can be manufactured using additive manufacturing processes. This can be demonstrated in *Additive manufacturing of fatigue resistant materials: Challenges and opportunities* by Yadollahi and Shamsaei. The main purpose of this paper is not to focus on the fatigue parameters but rather take a closer look into the challenges of using additive manufacturing to construct a metal part to the determine the fatigue life of the metal part. The additively manufactured parts are relative the same in mechanical properties from fatigue testing as the conventionally fabricated parts. This is because of the process taken when constructing an additively manufactured part. During this process, the material undergoes high cooling rates which increases a better microstructure when compared to conventionally cast parts. The main cause of fatigue failure is due in part to the microstructure presented in the material. However, though additive manufacture parts

21

conclude a shorter fatigue life, it isn't due to the fact of the chemical make up of the material but rather to the microstructure present on the surface of the casting known as surface roughness. Surface roughness was found to cause high stress risers on the casting and constitute in a shorter fatigue life of the cast part since additive manufacture process of metals contain a powder base material which results in voids on the surface. The larger the void on the surface of the casting, the shorter the life span of the cast part. The surface roughness of a part can pertain to the grain size of the powder used, the equipment, the parameters, and build orientation. An example to test the surface finish of a cast metal part was to use an Inconel 718 test specimen additive manufactured at a 45° angle which consisted of an overhang side. These specimens exhibits a higher surface finish on the overhang side of the Inconel 718 test specimen. To improve the surface finish on the overhang side, the test specimen can be machined or polished which will also increase the fatigue life of the part. Cracks propagate on the surface due to surface defects which is caused by the stress risers on the as-cast material. However, the material used in additively manufactured parts can have an effect on the fatigue life of a cast part. Parts printed in the vertical direction had a higher average surface finish (Ra=38um) compared to parts printed in the horizontal direction that had an average surface finish of Rq = 31um. In conclusion, changes made in the orientation of an additively manufactured parts on the build plate can be detrimental to the fatigue behavior of that part since these parts may contain overhangs that can cause high surface finish and a short fatigue life. The material used for additively manufactured parts can also have an effect on the fatigue behavior of a part since it contains properties such as ductility that causes a short fatigue life. [29]

Understanding how fatigue life can be influenced by surface finish can be seen in a study by Wang, Zhang, Sun, Liu, Shi, and Lu called *Giga-fatigue life prediction of FV520B-I with surface finish*. This study predicts that surface finish causes the fatigue life of a part instead of the internal inclusions within the material. Cracks initiate from the high stress concentrations areas found on the surface of a part. These high stress concentrations areas consist of deep grooves on the surface of a part or an imbalance in material that causes impurities which lowers the fatigue life of a part. This paper formulates a relationship between fatigue life and surface quality of a part. The material used in this study is a martensitic stainless steel called FV520B-I that operates under a frequency of 20kHz and a stress ratio of $r = -1$. The fatigue testing was conducted on a USF-2000 ultrasonic fatigue testing system. The test specimen can be seen below in Figure 10.

Figure 10: Fatigue Life Test Specimens

SEM (scanning electron microscope) testing was conducted during the test process that demonstrated that fatigue failures can occur on the surface due to the surface quality of a part. A chart of fatigue life to surface roughness can be found below in Figure 11.
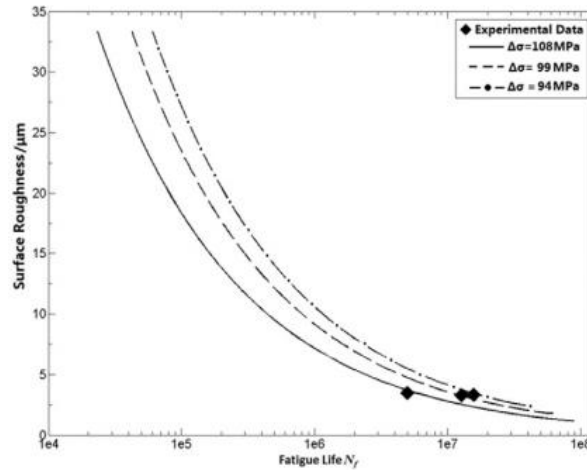
Figure 11: Fatigue Life to Surface Roughness

This chart shows the relation to fatigue life and surface roughness under three different amplitudes during testing. This state that the higher the surface roughness the shorted the fatigue life of the part which is to be assumed. [30]

To determine the fatigue life of a casting, experimental work and statistical modeling was performed in a study called *Statistical modeling of microstructure and defect population effects on the fatigue performance of cast A356-T6 automotive component* by Yi, Lee, Lindley and Fukui. Cast aluminum alloys especially A356-T6 can be seen in the automotive industry since A356-T6 has a high strength to weight ratio and is low in cost. Large defects such as cracks on the surface can decrease the fatigue properties of A356-T6. In this study, high cycle fatigue testing was performed to demonstrate that cast A356-T6 machined test specimens can have a long fatigue life. These test specimens were developed from a permanent A356 cast mold that contained the automotive cast parts in which were machined to fit the parameters of this study and then T6 heat treated using standard parameters. Fatigue testing was conducted on an Amsler Vibrophore machine using machined round specimens that contained a gauge diameter of 5mm. The load ratio

used was R = -1 and a frequency of 70Hz. Then the specimens after fatigue testing were examined using an SEM to determine information about the defects found that initiated the failure. It was found that porosity in the casting was the main defect to cause the failure in the automotive components. Below in Figure 12 is the S-N curve formulated from the results of this testing.
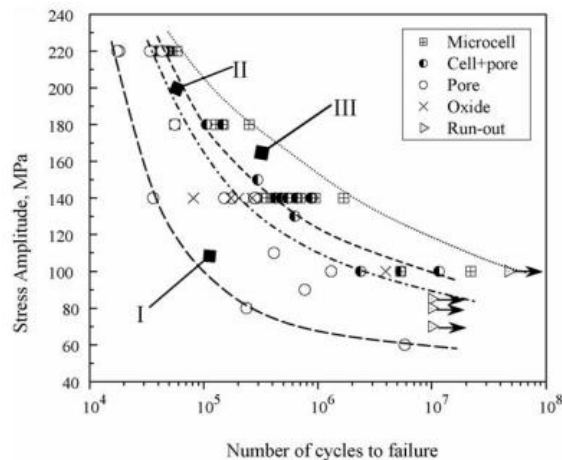
Figure 12: S-N Curve

The S-N curve contains the number of cycles to failure versus the stress amplitude of the fatigue testing. In conclusion, defects such as porosity, oxide films and the microstructure of the material does affects the fatigue performance of A356-T6. [31]

A comparison of traditional and additive manufacture process with two different types of material (AlSi10Mg and Ti6Al4V) for fatigue testing can be found in a study called *A comparison of fatigue strength sensitivity to defects for materials manufactured by AM or traditional processes* by Beretta and Romano. Defects are known to formulate during the manufacture process which is known to reduce the fatigue life of a part. However, surface roughness is categorized as short cracks on the surface of a part and therefore remains a defect on the material. The difference between traditional and additive

manufactured processes are the microstructure of the material and the solidification process. This is because traditional processes result in parts being machined after fabrication and containing a smooth surface to whereas additive manufacture parts tend to have a high surface finish which act as stress risers on the surface of the material. The smoother the surface, the higher the fatigue life since the smoother surface doesn't contain the high stress concentrators on the surface of the part which leads to a longer life of the part. In this study, two materials are compared using additive and traditional manufacturing. The two materials used are AlSi10Mg and Ti6Al4V since this material is frequently used in additive manufacture parts and will produce the best comparison between the two processes. The two stress ratios used were R = -1 and R = 0.1 for fatigue testing of the two materials using the two different manufacturing processes. It was found that the failure of the part was due to the surface defects found on the part. These results were formulated from a literature review performed in the study. Results of square root of area versus the Stress Amplitude for R = 0.1 can be found below in Figure 13.
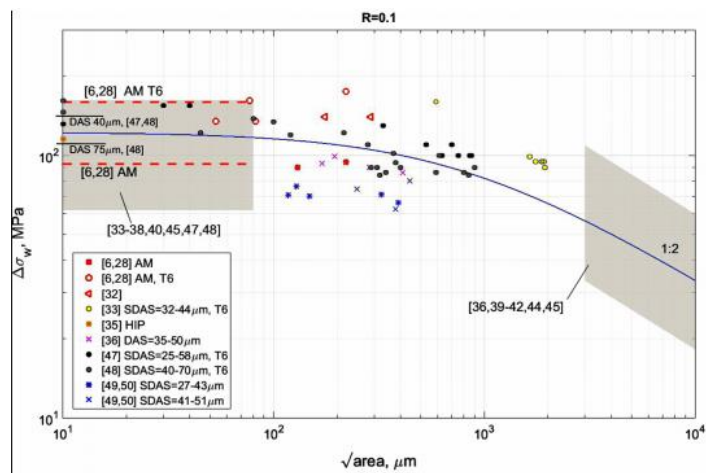
Figure 13: Square Root of Area vs. Stress Amplitude

It can be seen from the results that the manufacturing processes, both additive and traditional, are very similar and that additive manufacturing may be better suited for certain part than traditional manufacturing. [32]

In the paper, *the effect of porosity on the fatigue life of a cast aluminum-silicon alloy* by Gao, Yi, Lee and Lindley, it studies how the microstructure of a material can have an effect on the fatigue properties of a cast part. Both porosity and the microstructure impact the way the material fails during fatigue testing. Since the automotive and aerospace industry is producing light components for a vast decrease in weight and cost, it can be seen that cast aluminum is starting to take the place of traditional cast material such as iron or forged steel. However, the cast aluminum demonstrates a low fatigue life and in which can be detrimental to the automotive and aerospace industry for the lack of safety. Porosity and gas bubbles occur during the solidification process in which trapped gas and shrinkage of the material take place causing a decrease in the fatigue life. Most porosity and gas bubbles develop on or near the surface of the cast part which causes fatigue cracks due to high stress concentration areas. The experimental aspect of this study was to develop a wedge that was cast and undergo a standard T6 heat treatment. Once the cast was developed, it was divided into twelve similar pieces which was split into two categories. These two categories consisted of parts having identical microstructure and defect population. In order to determine which of the twelve pieces went into which category, a scanning electron microscope (SEM) was used. After, high cycle fatigue tests were conducted on an Amsler Vibrophore fatigue machine. The load frequency used was 70Hz with a stress ratio of 0.1 with a maximum amplitude of 120MPa. The results of the testing demonstrated that the fatigue cracks were due to irregular shaped pores found near or on

the surface of the casting. In conclusion, the experimental data determines that the casting defects found on or near the surface of the test specimen are the main cause of the fatigue life of a cast part. [33]

2.4 Tensile Fatigue

Tensile fatigue testing on a heat treated aluminum alloy can be demonstrated in a study by Roy, Nadot, Maijer and Benoit called *Multiaxial fatigue behavior of A356-T6*. This paper conducts a fully reverse cyclic loading using tensile and torsion loading of test specimens. Cast aluminum alloys are starting to replace cast iron parts due to the cast aluminum alloy light weight property as well cost reduction. There has been a relation made between the microstructure of the material and the fatigue properties. Fatigue cracks propagate within a part in the surface quality of that part is relatively smooth and contain no defects. But for fatigue to occur on a part is mainly due to porosity, gas pores and shrinkage of the material being used. To have a better understanding of the fatigue cracks due to the surface quality of a part, tension, tension-torsion and torsion fatigue testing was conducted. A wedged shape casting was produced and cylindrical round tensile bars were extruded from the casting. The wedged shaped casting was used to vary the range of parameters and defects on a cast part. Towards the bottom of the wedge which was considered the point, a more refined casting was produced which contained the highest cooling rate. Towards the top of the wedge which was considered a rectangular base, a coarser microstructure was produced and consisted of a lower cooling rate for solidification. The tensile testing consisted of a fully reverse cyclic loading, R = -1, with a sinusoidal signal and a load control. The tension-torsion was performed under 11Hz on an Instron servohydraulic test machine. The pure tension and torsion testing was conducted on an Amsler-Vibraphore machine at 45Hz. All fatigue testing was performed under high

cyclic loading which consisted of 10^6 cycles and then again but for a higher stress amplitude. It was found from the testing that the fatigue plane was normal to the applied stress for the pure tension. Thus from SEM testing, the fatigue did not occur from the microstructure of the material. However, pure torsion did demonstrate fatigue cracks irrelevant to the direction of the applied stress and had very different results compared to the pure tension. Pure torsion indicated that multiple crack planes collided together to form the fatigue failure of the test specimens. From these results, it was found that many of the initiated sites from the fatigue testing resulted in defects on the surface of the parts. These defects include porosity, shrinkage and gas pores. In conclusion, it was found that fatigue cracks propagate from either from gas bubbles or shrinkage found on the surface of a part. [34]

Long and small fatigue cracks on castings have been determine using multiple stress amplitudes on A356-T6. This can be seen in a study called *Integrated Experimental, Analytical, and Computational Design for Fatigue Crack Growth Resistance in Cast Aluminum Alloys* by Spangenberger and Lados. A356-T6 alloy microstructure was altered to fit the different characteristics in this study to determine the long and small crack growth. The material consist of a Mg-Si precipitation strengthened and to refine the grain size, Al, 5% of Ti and 1% of B was added to the material. For experimental work, a ASTM standard E647 was used for the long crack growth fatigue testing. This consisted of a rectangular test specimens with dimensions of 63.5 x 61 x 10 mm with a stress ratio of R = 0.1, 0.5 and 0.7. These test specimens were used for compact tension fatigue testing. For small crack growth fatigue testing, this consisted of a corner flaw tension specimens with a gage cross-sectional area of 10 x 5mm and notch size between 200 and 300 μm. These test specimens

were tested with a stress ratio of R = 0.1 and a cyclic frequency of 20Hz. The modifications made to the material allows for the material to control the crack growth by using the smaller grain size. For the long crack growth, the two different grain sizes used were 500 and 1300 μm at the three stress ratios. This resulted in a larger grain size material which has a higher crack growth. This also demonstrated that the Sr-modification in the material increased the toughness of the material which resulted in a higher fatigue life of the casting. The results for the small crack growth fatigue testing used 500μm grain size which resulted in a longer fatigue life due to the small grain size. [35]

3.0 Methodology and Procedure

3.1 Phase 1 – Benchmark Casting
The first phase of this project is to design and manufacture a benchmark casting. A benchmark casting acts as a standard to evaluate surface roughness and surface features. The various surfaces of a casting parts will have multiple print orientation angles.

3.2 Keyence Microscope
The Keyence Microscope VK-X200 series is a non-contact 3D laser scanning confocal microscope used to scan surfaces for analysis. The Keyence Microscope enables high resolution and high magnification imaging, and high accuracy surface scanning technique.. The VK-X200 series has two different programs used to scan and compile data. These programs consist of the VK-Viewer which allows for accurate scanning of an object and the VK-Analyzer which analyzes data that was assembled from the scan.

The Keyence Microscope VK-X200 Series Viewer package measures a 3D image object with an accelerated laser scanning approach. It has a 16-bit photomultiplier that allows the laser light to be captured and processed for measurement data for any given object [36]. The 16-bit photomultiplier allows the scanner to collect 65,536 shades to then

build an image to be evaluated. The Keyence Microscope has a high accuracy scanning technique that enables a 0.5nm linear module that is embedded into the software to improve the z-resolution of any scan. The Keyence Microscope has a dual laser light source which is able to capture a 2D image as well as a 3D height image. These images are then assembled together to form the scan. Each of these images are captured using the high-speed scanner which then scans the layer in the X-Y direction. The Keyence Microscope has a tool to assemble multiple images together to form a scan. This is called the automatic image assembly. As stated in [39] "automatic image assembling is a technique to automatically perform a series of tasks to collect multiple image data by moving the measurement area and assembling the data into one image". The multiple scans taken in the X-Y direction are then assembled together in the Z-direction to form to height of the scan. The height resembles the surface roughness of a part. The white laser light source captures the height of the scan while the laser light source captures the resolution of the scan. The measurement principle for surface roughness is assembled using a RPD algorithm which is unique to the Keyence software. This allows for interpolation of the data points to achieve an accurate reading. The RPD algorithm is an interpolation of the received reflected light intensity from the laser feature of the microscope versus the position of the Z axis.

The Keyence Microscope has three different magnifications for viewing a test specimen which include 10x, 15x and 20x. When scanning with precision and high magnification, it results in small images. However, the Keyence Microscope allows for multiple small images to be stitched together to form one image that is better for analysis. This enables a wider field of view to keep track of what part of the specimen is being

analyzed as well as a bigger image for accurate results. If a test specimen has complex geometry in which the received laser light is unable to detect, a second scan is performed to collect missing data .

The Keyence Microscope VK-X200 Series Analyzer package measures the scans generated in the Viewer package by using 42 known roughness parameters. These parameters are then used to compare surface quality of multiple scans. The parameters outputs are seen in Table 1.

Table 1: Parameters from the Keyence Microscope

Parameter	Abbreviation
Highest Peak	Rp, Pp, Wp
Lowest Valley	Rv, Pv, Wv
Average Height	Rc, Pc, Wc
Maximum Height	Rz, Pz, Wz
Total Height	Rt, Pt, Wt
Arithmetic Mean Roughness	Ra, Pa, Wa
Root Mean Square Height	Rq, Pq, Wq
Kurtosis	Rku, Pku, Wku
Skewness	Rsk, Psk, Wsk
Element Average Length	RSm, PSm, WSm
Root Mean Square Tilt	$R\Delta q, P\Delta q, W\Delta q$
Load Length Ratio	Rmr (c), Pmr (c), Wmr (c)
Profile curve Cut Level Height	$R\delta c, P\delta c, W\delta c$
Load Curve	BAC
Relative Load Length Ratio	Rmr, Pmr, Wmr
Probability Density Function	ADF

There are numerous tools used to measure the surface quality of a scan which consist of the automatic measurement, individual and multiple line roughness measurement, surface roughness measurement, profile viewer, etc. These tools output the roughness parameters, however, not every tool outputs all 42 roughness parameters. Each tool outputs roughly 15-20 different parameters depending upon the tool being used.

The tool used in this project was the multiple line roughness tool. This tool allows for multiple profile lines to be applied on the scan to determine the different surface parameters for each given line. The multiple lines were then averaged together to achieve one value for all the surface parameters. Some of the surface parameters obtained from this tool are as follows: horizontal distance, highest peak (Rp), lowest valley (Rv), total height (Rt), average height (Rc), arithmetic mean roughness (Ra), root mean square height (Rq), skewness (Rsk), kurtosis (Rku), etc. The worksheet that is formulated from this tool contains a 3D image of the scan with the one main line on it, a top view of the 3D image that contains all the lines, the actual cross section profile 2D graph, the profile curve 2D graph and the load curve/probability density function (BAC/ADF) 2D graph. The data of all the different surface parameters for each line are provided as well as an average, maximum, minimum, standard deviation and 3sigma. The CSV file can be exported as an excel document for further analysis of the data. The CSV file will also contain the values for all the lines placed on the scan for comparison purposes.

The Keyence Microscope is a non-contact microscope. It is unable to construct a straight line like conventional contact profilometer. Therefore, the confocal microscope is able to scan using a laser build into the microscope that scans along the XY axis. The objective lens then moves in the Z axis to capture the height. Multiple layers of scans on the XY plane are compiled together until the measurement range is met. Once this is met, the scan is complete. This scan outputs a measurement profile which is a sideways bell curve. This demonstrates the received reflected light intensity to the position of the Z axis. This curve is generated by a build in RPD algorithm into the microscope program. A normal conventional microscope collects a set of data points and then compile the sideway

bell curve to describe the surface roughness. The RPD algorithm, assembles these data points and interpolates in between the data points to find a best fit curve line to pull the detected focal point position. This value is what is given in the parameters depending upon what tool is being used.

The Keyence Microscope is used in this project because the project contains test specimens that are hard to generate results using a profilometer. This is because the test specimens are 3D sand printed parts that are then cast. The sand contains multiple peaks and valleys in a given scan that would be hard for a profilometer to measure. The profilometer drags a needle across a given length of a test specimen. Since sand is being used, the profilometer's needle will become dull and will give inaccurate results. The Keyence Microscope is a non-contact microscope that allows for a surface to be scan without the instrument becoming dull to give accurate results.

The two main parameters used in this project are the average mean roughness (Ra) and the root mean square height (Rq) to determine the surface quality of two casting that used a 3D sand printed mold that contained one mold that was coated and another mold that was non-coated. The average mean roughness is the computation of the absolute value of the average roughness of the reference length. This can be seen in Figure 14. [36]

$$Za = \frac{1}{\ell r} \int_o^{\ell r} \left| Zn \right| dx$$

*Za indicates Ra, Pa, and Wa.

Reference length ℓr

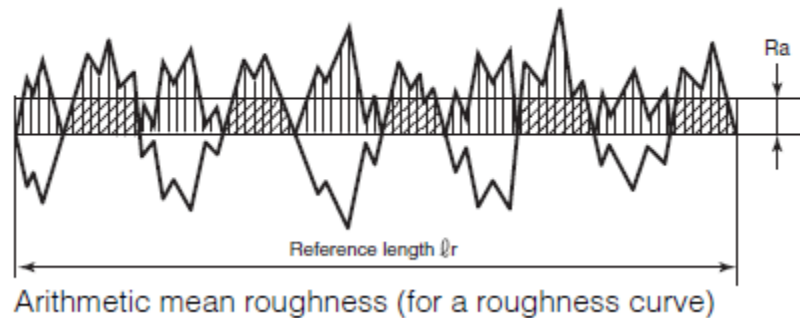Arithmetic mean roughness (for a roughness curve)

Figure 14: Ra Calculation

This is the average of the surface quality that contains the peaks and valleys and the average mean roughness calculates the average of these peaks and valleys for a given length. The root mean square height is the square root of the calculated average that is squared over the reference length or described as the variance of the average height from the mean line. This can be seen below is Figure 15. [36]

$$Zq = \sqrt{\frac{1}{N} \sum_{n=1}^{N} Z_n^2}$$
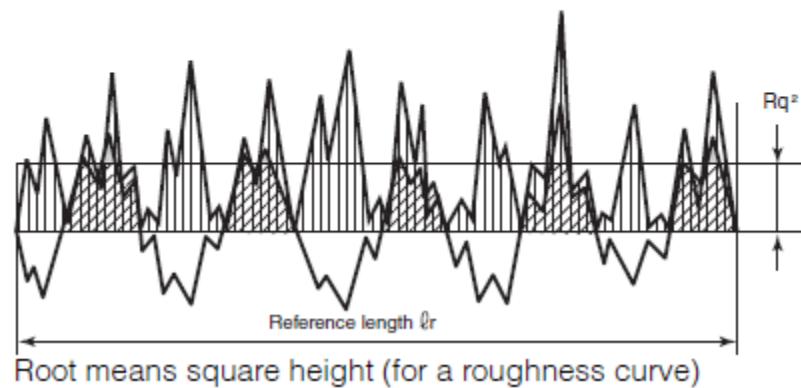
*Zq indicates Rq, Pq, and Wq.

Root means square height (for a roughness curve)

Figure 15: Rq Calculation

Ra and Rq are common metrics for measuring the surface roughness of a specimen.

3.3 Phase 2 – Fatigue Testing

The second phase of this project is to perform static tensile and fatigue testing on cast specimens. The fatigue specimens were on cast flat bars with dimensions of 4 x 2 x 0.25 inches. The tensile bars were ASTM E8/E8m-09 standard sheet-type. The testing was conducted to determine the mechanical properties of cast A356-T6 using additive manufactured sand molds. Specimens, molds and casting were designed. The new cast

parts were designed at four out of the six different print angle orientation to focus in on the stair step feature effect. These four angles were 0°, 5°, 15°, and 30°. No coating to improve surface finish was used on the molds since the focus of the second phase is to determine the mechanical properties of the cast A356-T6 parts at different print orientation angles that contain stair step features.

3.4 Phase 3 – Fluorescent Penetrant Inspection Testing

The third phase of this project is to perform fluorescent penetrant inspection testing on the flat static bars with dimensions of 4 x 2 x 0.25 inches. Fluorescent penetrant inspection testing is implemented by placing a dye on the casting to find surface defects and surface cracks. This is a non-destructive inspection test. In this project, the dye is placed on the as-cast surface that contained the stair step features. The as-cast surface means that this surface wasn't machined until smooth. The fluorescent penetrant inspection testing required the design of new riser and gating for the cast specimens. Twenty-one specimens were needed for the testing total for all seven print orientation angles. These angles included 0°, 5°, 10°, 15°, 20°, 25° and 30°.

4.0 Results and Discussion

4.1 Phase 1 – Benchmark Casting Results

The first phase of the project is on the surface finish of the benchmark casting using the Ra and Rq values. The benchmark casting can be seen below in Figure 16.
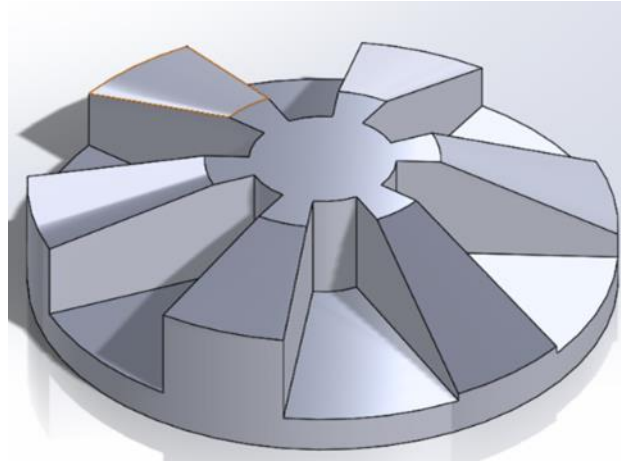

Figure 16: Benchmark Casting

This benchmark casting is a round four-inch casting that contains six different print orientation angles. These angles consist of 5°, 10°, 15°, 20°, 25° and 30° print orientation angles. There are two castings per mold: one upward facing and one downward facing. This allowed comparison of the six different print orientation angles. Printing the mold upwards consists of the cavity being printed in the positive z-direction as seen in the figure above. Printing the mold downwards consists of the cavity being printed in the negative z-direction which can be seen if the figure above was flipped 180°. The main purpose in designing a benchmark casting is to determine the size and space of stair step features and the surface roughness metrics of the part surfaces cast at different print angle orientations in the mold.

The angle of print orientation for the benchmark casting is taken from the x-y plane. This can be seen below in Figure 17.
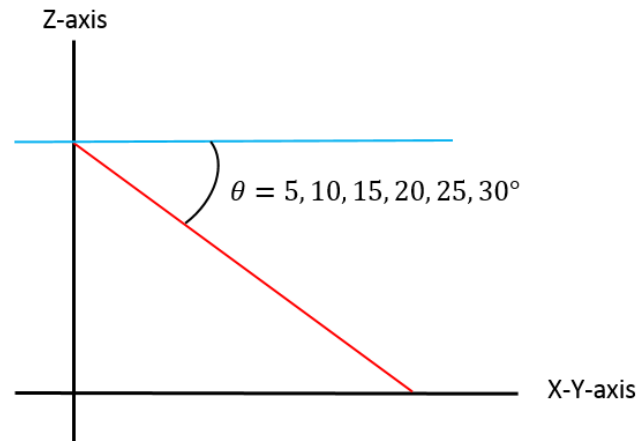

Figure 17: Angle of Print Orientation

The angle of print orientation was taken in the x-z plane. In additive manufacturing, height is represented in the z-direction. Since 3D printing is a layer by layer process, one layer is laid down in the x-y plane and multiple layers are combined to form the height of the part in the z-direction. .

Once the benchmark casting was designed, a gating system was added to the design of the casting. This gating system consisted of a one pour cup, one sprue, one sprue basin, two gates to feed the casting, and two tapered feeders/vents as seen below in Figure 18.
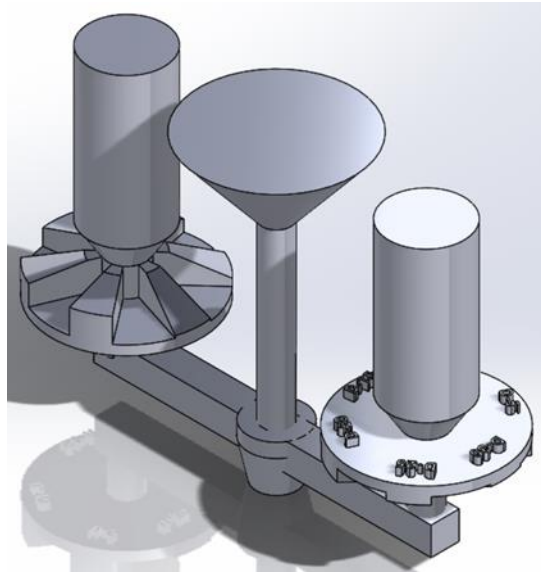
This design does not include a tapered runner since the parts are located at the end of the runner and all molten metal must flow through the part without it solidifying before filling the part. The pour cup has dimensions of 2 inches high, and a circular diameter of 0.75 inches with a 40° draft outward. The runner has dimensions of 9 x 0.75 x 0.75 inches (l x w x h). The sprue has dimensions of 0.75 in diameter and 5 inches in height. The sprue basin is located at the bottom of the sprue with dimensions of 1.5 inches in diameter which is 1.375 inches with a draft inward of 12°. Lastly, the gates consist of 0.75 inches in diameter and a height of 1.25 inches with an 8-inch gap between the two gates.

The mold was designed based on the cavity of the part. Since the geometry prevents a flat parting line, a staggered parting line that ran at the bottom of the two parts can be seen below in Figures 7, 8, and 9.
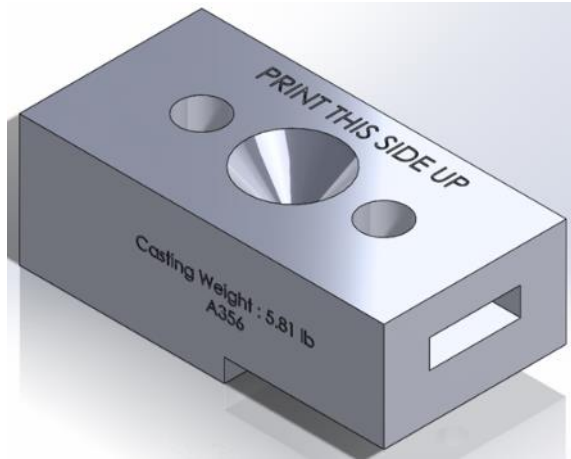
Figure 20: Cope of Benchmark Casting
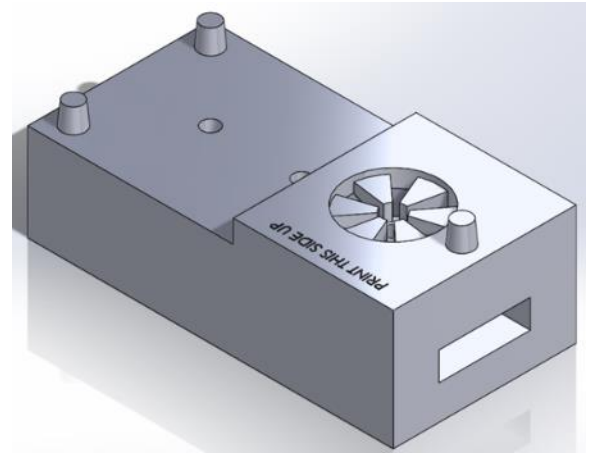
Figure 19: Drag of Benchmark Casting
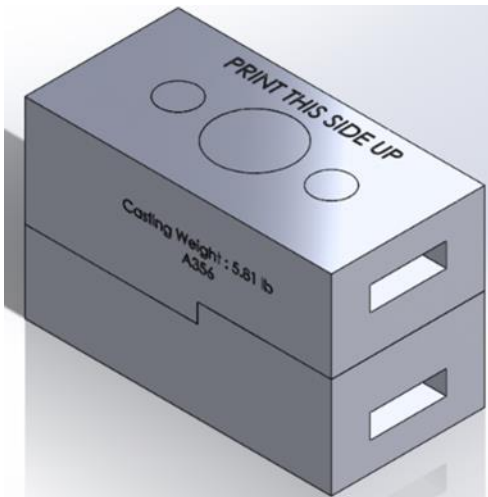
Figure 21: Mold for Benchmark Casting

This mold contained lifting holds on both sides of the mold for the cope and drag. These are inserted to help lift the mold for cleaning and assembly. The pegs on the cope are designed to assist with assembling the. The pegs are tapered to prevent the mold from rubbing sand-on-sand and distributing debris throughout the casting. Lastly, a casting weight of 5.81 lbs. is inserted on the cope so ensure that only that amount of molten metal is used so that extra material is not wasted.

Two molds were fabricated during phase one of this project. The mold design was the same for both, however, one mold contained a coating located on the print orientation

angle slope of the benchmark casting. The purpose of the coating was to determine if the coating improved the surface finish of the cast A356 part. The coating on the sand mold may increase the smoothness of the surface finish of the casting and therefore decrease the post processing on the cast part. The coating used was Dura Kota 4482 from HA International LLC. It is light-blue in color and premixed. Dura Kota is a water-based material coating with a typical density of 19.80 lbs./gal and a Zircon refractory system [38]. The coating was applied using a generic paint brush from Home Depot and placed on the print angle slope of the benchmark casting.

After the casting with a gating system was designed and a mold was constructed, the files were sent to Humtown Products in Leetonia, Ohio to be printed on the ExOne S-Max sand printer. The sand used is IC-80 Oklahoma which has a grain fineness number (GFN) of 83. The grain fineness number is the average size of a granular material [4]. The higher the GFN the finer the sand and the smoother the cast part is. The GFN number is crucial in sand casting since it can lead to potential casting defects [39]. The binder used is 371381 Eniroset 3D Jet Resin (international). Below in Figures 22 and 23 are the sand molds printed from Humtown Products.

Figure 22: Inside Sand Mold of Benchmark Casting

Figure 23: Sand Printed Molds

Figure 24 the US screen analysis from Humtown Products. A screen analysis is a particle size variation. A comparison for better understanding of a micron can be compared to an inch can be seen in Table 2. One micron is equivalent to 0.0000394 inches.

CUSTOMER:	Humtown						
ATTN:	Mark			FAX:			

	12/9/2016	12/9/2016	Keener				
SAMPLE DATE:	12/9/2016	12/9/2016	Keener				
TEST DATE:	12/9/2016	12/9/2016					
SAMPLE ID:	Unimin Incast 80	Ex One	730 Wedron				
MOISTURE: [%]							
COMPACTABILITY:							
PERMEABILITY							
SPECIMAN WEIGHT [GR]							
MLD.HDNS. B SCALE:							
GREEN COMP. STR.							
GREEN SHEAR [PSI]							
25 MIC. CLAY [%]							
METH. BL. CLAY [%]							
L.O.I. AT 1800F. [%]							
VCM AT 1200 F. [%]							
ADV							
WORKING BOND	0.00	0.00	0.00	0.00	0.00	0.00	0.00
AVAILABLE BOND	0.00	0.00	0.00	0.00	0.00	0.00	0.00
MIXING EFF.	0.00	0.00	0.00	0.00	0.00	0.00	0.00
25 MIC. / MB CLAY	0%	0%	0%	0%	0%	0%	0%
US SCREEN							
6	0.0%	0.0%	0.0%				
12	0.0%	0.0%	0.0%				
20	0.0%	0.0%	0.0%				
30	0.0%	0.0%	0.0%				
40	0.2%	0.0%	0.0%				
50	1.4%	2.0%	2.2%				
70	10.8%	15.0%	14.7%				
100	39.9%	48.9%	47.5%				
140	33.5%	27.5%	28.8%				
200	12.6%	5.8%	6.4%				
270	1.6%	0.8%	0.4%				
PAN	0.0%	0.0%	0.0%				
AFS	88.28	79.8	80.0				

Figure 24: Humtown Product US Screen Analysis

Table 2: Conversion Table of US Mesh to Micrometers

US Mesh	µm
12	1680
20	841
30	595
40	420
50	297
70	210
100	149
140	105
200	74
270	53

The pour took place at Bliss Hall at Youngstown State University's foundry. There are multiple steps in a pour. First, the metal was heated to a temperature of 1450° Fahrenheit in a crucible to melt the metal and prepare it for pouring. The metal was heated to this certain temperature (called the pour temperature) to increase the flow of the material, so no solidification took place while filling the cavity within the mold. This was to ensure that the entire casting was filled completely. The temperature of the aluminum during the pour was between 1350 and 1400°Ft. The molten metal decreased by approximately 50° F because it was cooled by the atmospheric temperature while moving the crucible filled with molten metal from the oven to the place of pour. The casting took thirty hours to solidify and cool before it was broken away from the sand mold. The casting within the sand mold was dropped from a height of four feet to break the sand mold and retrieve the casting. Below in Figure 25 is the benchmark casting.

Figure 25: Benchmark Casting

There were four different benchmark castings which consisted of a non-coated up, non-coated down, coated up and coated down. The non-coated up included no coating on

the print orientation angles and was printed up along the z-axis. The non-coated down included no coating on the print orientation angles but the angles were printed down along the z-axis. The coated up consisted of coating along the print orientation angles and the angles were printed up along the z-axis. Lastly, coated down consisted of coating along the print orientation angles but was printed down along the z-axis.

The Keyence microscope, VK-X200, was used to obtain the Ra and Rq values found with the different casting print orientation angles to determine the smoothest of each casting print angle orientation. The VK Viewer was used to create a magnified image of a surface that is 0.04 by 0.4 inches with a varying height and then it was scanned using the camera to laser feature. The camera feature is used to capture the image and the laser is used to accurately determine the surface quality of the casting. Once the scan was complete, the VK Analyzer was used to analyze the scan made in the VK Viewer. There are multiple tools in the VK Analyzer used to achieve the surface finish of a cast part. The tools used in this project was the multiple line surface roughness tool. The scan was inputted into the display area and a single two-point line was placed vertically in the middle. Next, a range of lines were selected which demonstrate the amount of lines preceding from the single vertical line just made. A range of five profile lines for this project.

The measurements of Ra and Rq were taken on all six angles of the benchmark casting using the Keyence Microscope multiple surface roughness line tool. The scans were in the center of each of the print orientation angles. Two scans were taken per print orientation angle and then averaged to formulate the Ra and Rq values. The values of the

top and bottom were averaged together to achieve the Ra and Rq values for either the coated or non-coated. The four different casting results can be seen below in Figure 26.

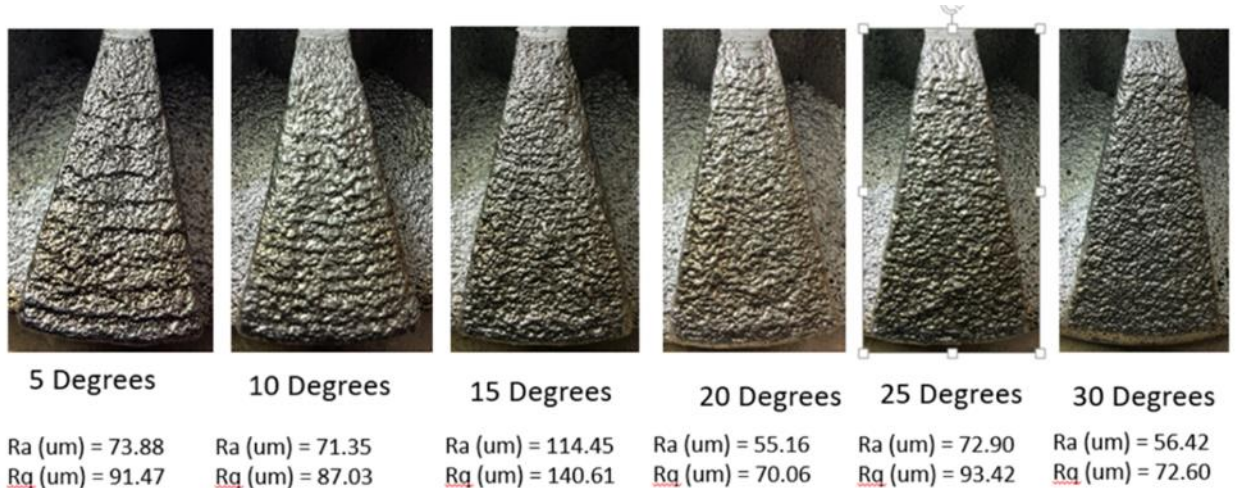Above in Figure 26 it can be seen that in the lower degrees, the casting print

5 Degrees	10 Degrees	15 Degrees	20 Degrees	25 Degrees	30 Degrees
Ra (um) = 73.88	Ra (um) = 71.35	Ra (um) = 114.45	Ra (um) = 55.16	Ra (um) = 72.90	Ra (um) = 56.42
Rq (um) = 91.47	Rq (um) = 87.03	Rq (um) = 140.61	Rq (um) = 70.06	Rq (um) = 93.42	Rq (um) = 72.60

Figure 26: Non-Coated Up Results

orientation angles contain a stair step effect. The most visual stair steps can be seen in both the 5° and 10°. As it progresses to 30°, stair steps are not as visible to the naked eye. Besides stair steps, other surface defects can be seen on the surfaces of the print orientation angles. These can be seen in the bottom left hand corner of the 15° and 20° angles. There is also an elevated defect at the bottom middle of the 25° angle. These are either caused by the cleanout of the molds, packaging or transportation.
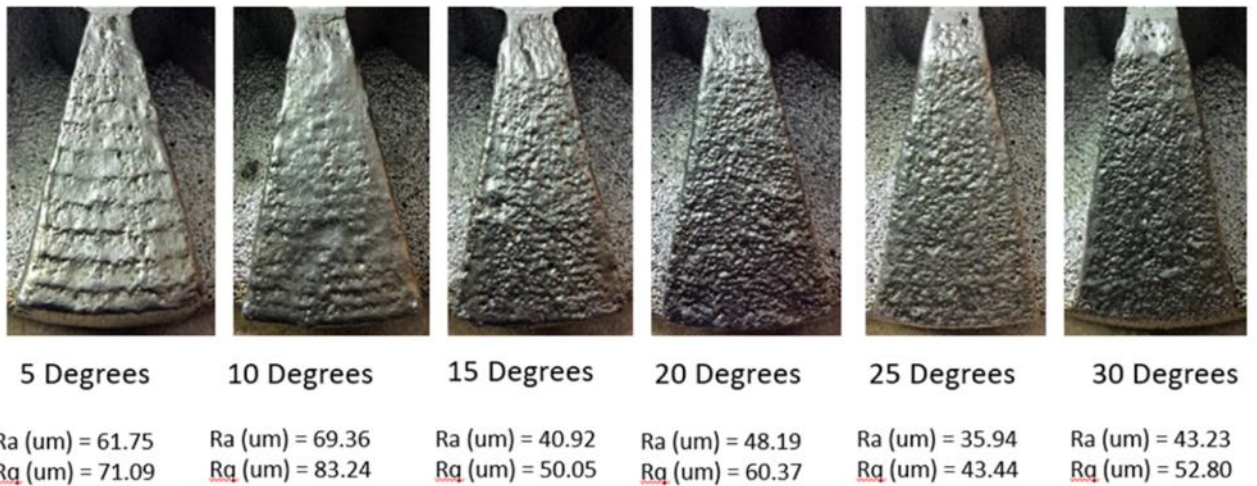
5 Degrees	10 Degrees	15 Degrees	20 Degrees	25 Degrees	30 Degrees
Ra (um) = 61.75	Ra (um) = 69.36	Ra (um) = 40.92	Ra (um) = 48.19	Ra (um) = 35.94	Ra (um) = 43.23
Rq (um) = 71.09	Rq (um) = 83.24	Rq (um) = 50.05	Rq (um) = 60.37	Rq (um) = 43.44	Rq (um) = 52.80

Figure 27: Coated Up Results

Above in Figure 27, it can be seen the coated print orientation angles. Again, a stair step effect can be seen using the naked eye for the first few angles. The coating does seem to improve the surface quality of the print orientation angles by comparing the Ra and Rq values to the uncoated specimens above. However, on the 5° and 10°, the coating was applied very heavily and therefore caused inaccurate Ra and Rq values. Also seen on the 10°, there is a large defect in the middle of the cast print orientation angle. This could have been caused by cleanout of the molds by accidently brushing that area too hard or using the air brush too close. These defects were not caused by packaging or transportation because the coating was applied after cleanout and before packing.
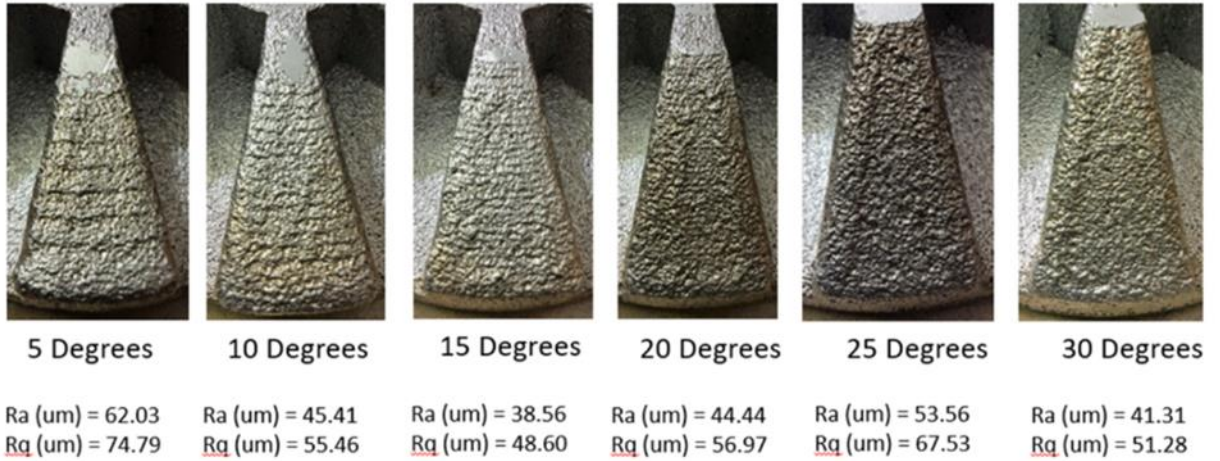
47

5 Degrees	10 Degrees	15 Degrees	20 Degrees	25 Degrees	30 Degrees
Ra (um) = 62.03	Ra (um) = 45.41	Ra (um) = 38.56	Ra (um) = 44.44	Ra (um) = 53.56	Ra (um) = 41.31
Rq (um) = 74.79	Rq (um) = 55.46	Rq (um) = 48.60	Rq (um) = 56.97	Rq (um) = 67.53	Rq (um) = 51.28

Figure 29: Non-Coated Down Results

Above in Figure 28, it can be seen the non-coated print orientation angles. These print orientation angles were printed down within the mold. The casting that was printed in the downward orientation contained less surface roughness. This is because when the mold was printing, these print orientation angles had a longer time to dry so therefore no loose sand was extracted when the mold was cleaned out. Also, more sand sat on top of the mold which caused these print orientation angles to be compress so that no loose sand would cause defects on these angles. The stair step effect is still visual in the non-coated down benchmark casting. It can also be seen line indents on the 20°, 25° and 30° angles. This can be caused by heavily brush strokes during clean out. But no defects were seen in the previous degrees.
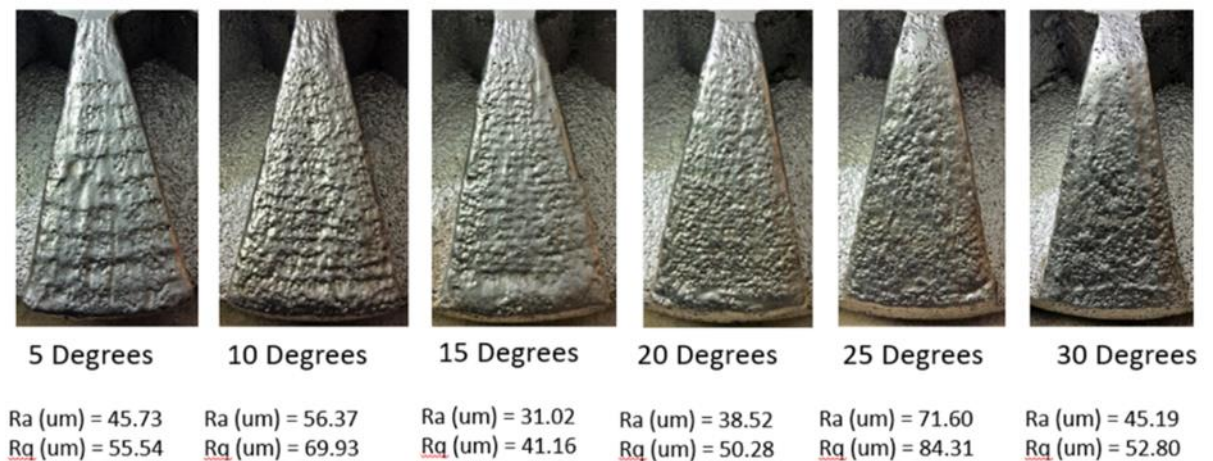

5 Degrees	10 Degrees	15 Degrees	20 Degrees	25 Degrees	30 Degrees
Ra (um) = 45.73	Ra (um) = 56.37	Ra (um) = 31.02	Ra (um) = 38.52	Ra (um) = 71.60	Ra (um) = 45.19
Rq (um) = 55.54	Rq (um) = 69.93	Rq (um) = 41.16	Rq (um) = 50.28	Rq (um) = 84.31	Rq (um) = 52.80

Figure 28: Coated Down Results

Above in figure 28, it can be seen the coated down print orientation angles. Since the Ra and Rq values were lower on the non-coated down print orientation angles, the coating was proven to worsen the surface quality of the part. This is caused by the excessive amount of coating placed randomly on the print orientation angle. The coating was brushed on and not evenly distributed throughout the entire angled surface. This can be seen on the print orientation angle at 5° and 15°. It can also be seen around the edges of 20°, 25° and 30°. The scans were only taken from the center of the part so therefore, the edges were not included in the measurements. No brush stroke lines can be seen on these angles so therefore the coating itself is what caused the high Ra and Rq values.

The results of the Keyence data on the benchmark casting were recorded in Microsoft Excel. The results were used to determine which of the angles contain the worst and best surface qualities as well as to compare between the coated and non-coated using the Ra and Rq values. However, it was concluded that the stair step effect at different angles does not influence the casting. Hand calculations of Ra and Rq were formulated to compare to the Keyence results. This was completed to determine how a stair step piecewise function compared to that of the surface finish stair step effect seen in all angles. These hand calculations can be seen below.

Surface Roughness Hand Calculations
Arithmetic mean roughness (Ra) – indicates the average of the absolute value along the reference length

$$Ra = \frac{1}{\ell_r} \int_0^{\ell_r} |Z_n| dx \quad (1)$$

$$Ra = \frac{1}{n} * sum(abs(Z_i - Z_{mean})) \quad (2)$$

$$Z_i = total\ height$$

$$Z_{mean} = average\ height$$
$$N = 20$$

Root mean square height (Rq) – indicates the root mean square along the reference length

$$Rq = \sqrt{\frac{1}{N}\sum_{n=1}^{N} Z_n^2} \quad (3)$$

Below in Figure 30 is an image of one stair step to determine the distance of one stair step per angle.
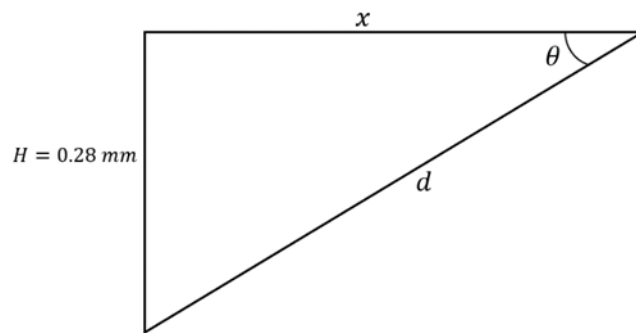

Figure 30: Demonstration of a Single Stair Step Feature

Solve for d (distance) to determine the distance of one stair step per angle.

$$sin\theta = \frac{0.28mm}{d} \quad (4)$$

$$d = \frac{0.28}{sin\theta}$$

θ used in this project relates to the angle orientation of print which consist of 5°, 10°, 15°,

20°, 25° and 30°. The distance for one stair step at the given angle can be found below.

5° has a one stair step distance of 3.2126 mm

10° has a one stair step distance of 1.6125 mm

15° has a one stair step distance of 1.0818 mm

20° has a one stair step distance of 0.8190 mm

25° has a one stair step distance of 0.6625 mm

30° has a one stair step distance of 0.5600 mm

The arithmetic mean roughness and the root mean square height will be calculated using an analytical. The maximum allowed distance of the line profile given by the Keyence measuring tool is 0.5 inches or 12.7 mm. This is the distance which is used to determine the number of stairs per given angle of length 12.7mm.

Ra and Rq Calculation for 5°

$$Number\ of\ Stairs = \frac{12.7\ mm}{3.2126} = 3.9683\ stairs\quad (5)$$
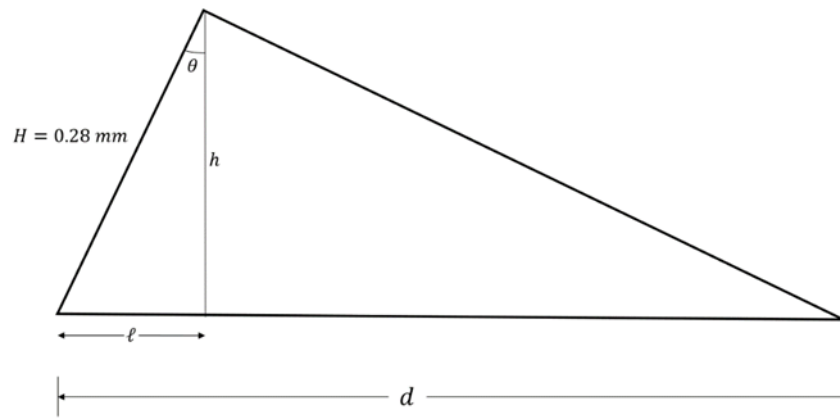
Figure 31: Determining Distance of Stair Step Feature

The number of steps per angle can be found in Table 3 below.

Table 3: Number of Steps per given angle

Degree	Distance of Step (mm)	Number of Step
5°	3.213	3.95
10°	1.613	7.88
15°	1.082	11.74
20°	0.819	15.51
25°	0.663	19.17
30°	0.560	22.68

Next, ℓ and h are found to determine the equations of the piecewise function over the given

reference length of 12.7 mm.

$$sin5° = \frac{\ell}{0.28 \; mm} \qquad \rightarrow \qquad \ell = 0.0244 \quad (6)$$

$$cos5° = \frac{h}{0.28 \; mm} \qquad \rightarrow \qquad h = 0.2789 \quad (7)$$

Now, equations of the piecewise function are found below. There are eight equations use

to make up the piecewise function. These eight equations are formulated by achieving the

slope of each individual line and using the slope-intercept form to accomplish a line.

Equation of line 1a:
$$points: (0,0) \; and \; (0.0244, 0.2789)$$

$$slope \; (m) = \frac{0.2789 - 0}{0.0244 - 0} = 11.4317 \quad (8)$$

Slope intercept form:

$$y - y_1 = m(x - x_1) \quad (9)$$

$$y - 0.2789 = 11.4317(x - 0.0244) \quad (10)$$

Therefore, the equation of line 1a:

$$y = 11.4307x \quad (11)$$

Equation of line 1b:

$$points: (0.0244, 0.2789) \; and \; (3.2126, 0)$$

Same procedure is used to obtain,

$$y = -0.0875x + 0.2811 \quad (12)$$

The same method is carried out through all eight equations of the piecewise function and

the remaining equations are as follows:

$$\text{2a:} \quad y = 11.4307x - 36.7211 \quad (13)$$

$$\text{2b:} \quad y = -0.0875x + 0.5622 \quad (14)$$

$$\text{3a:} \quad y = 114307x - 73.4420 \quad (15)$$

$$\text{3b:} \quad y = -0.0875x + 0.8433 \quad (16)$$

$$\text{4a:} \quad y = 11.4307x - 110.1629 \quad (17)$$

$$\text{4b:} \quad y = -0.0875x + 1.1244 \quad (18)$$

Twenty points were used to determine an accurate Ra and Rq value with increments of 0.635 mm. To calculate the Ra and Rq value, a Z_{mean} was calculated based on the $\frac{height\ (h)}{2}$. In this case, $Z_{mean} = 0.1395\ mm$.

The Ra and Rq values are as followed for 5°:

$$\text{Ra} = 70.6963$$

$$\text{Rq} = 81.1921$$

The same procedure is carried out for all remaining angles (10°, 15°, 20°, 25° and 30°) to achieve the Ra and Rq values. A table can be found below in Table 4.

Table 4: Hand Calculated Ra and Rq Values for all six print angle orientations

	5°	10°	15°	20°	25°	30°
Ra	70.6963	68.9462	65.5840	63.4241	63.5790	61.3527
Rq	81.1921	80.0084	76.1107	73.3769	73.1960	75.8372

Once this table was constructed, it was then compared to the results from the Keyence Microscope and the profilometer results. It was compared to the non-coated cast since there was no way to demonstrate and formulate equation that had a coating to compare to. These results can be seen below in Table 5.

Print Angle Orientation	Calculate Ra (µm)	Keyence Non-Coated Cast Ra (µm)	Percentage Difference
5°	70.6963	67.9562	3.88%
10°	68.9462	58.6709	14.90%
15°	65.584	76.1618	16.13%
20°	63.4241	50.2092	20.84%
25°	63.579	63.9646	0.61%
30°	61.3527	49.5921	19.17%

Above it can be seen that the calculated Ra value decreases while the print angle orientation increase. However, the Keyence data has a variation per increase in print angle orientation. This may be due to clean out of the mold before pour or a defect on the surface. Thought some angles contain high percentage difference between the hand calculated Ra and the Keyence non-coated cast Ra, they were what was expected and accounted for especially with the casting containing sand particles surface finish compared to calculated smooth piecewise stair step function.

Table 6: Percentage Difference of Hand Calculations to Experimental for Rq

Print Angle Orientation	Calculate Rq (µm)	Keyence Non-Coated Cast Rq (µm)	Percentage Difference
5°	81.1921	83.1300	2.39%
10°	80.0084	72.1100	9.87%
15°	76.1107	94.7700	24.52%
20°	73.3769	64.7300	11.78%
25°	73.196	81.7900	11.74%
30°	75.8372	63.3600	16.45%

Above in Table 5, it can be seen that the calculated Rq value decreases while the print angle orientation increase. The percentage difference between the experimental and the calculated value are increasing while print angle orientation is increasing except for angle at 15°. This could be due in part from the clean out of the mold at this angle that caused the streaks seen in the above figures by a generic Home Depot paint brush or there could have been a defect on that angle during print. Overall, the percentage difference was

small relative to calculating a piecewise stair step function to that of a 3D sand printed mold containing the stair step effect with a surface roughness attached.

4.2 Phase 2 – Fatigue Testing Results

The second phase of the project's focus is redesigning the casting with gating system and molds to cast specimens for static tensile and fatigue testing. A new cast was first developed for the four different print orientation angles. The four different print orientation angles chosen was 0°, 5°, 15°, and 30°. 0° is the baseline because there are no stair steps at this angle. The print orientation angle of 5° is where the stair step effect is most defined. The print orientation angle of 15° is a transition angle of still seeing the stair step effect but blending into a no stair step effect. Lastly, the print orientation angle of 30° visually shows no stair step effect.

A gating system was constructed and was the same for all four angles. This is because the specimens themselves didn't change just the print orientation angle so therefore the gating system was able to be used for all four angles. The gating system was designed based on calculations from the Principles of Foundry Technology. Some standards from the book states that the sprue size vary from 10mm² for work below 12kg poured weight to about 50mm² for heavy casting. The width and depth of the sprue well are about 1 ½ times those of the runner. Lastly, a ratio must be set. An example of a gating ratio is 1:3:3 which means 1 is the sprue diameter, 3 is three times the sprue diameter for the cross section of the runner and 3 is three times the sprue diameter for the cross section of the gates. The cross section of the runner and the gating is the flow path in which the molten metal will take. Below are the calculations used to design and construct the gating system.

The first calculation is to determine the pour rate of the molten metal.

$$R = b\sqrt{W} \quad (19)$$

$$R = the\ pour\ rate$$

$$b = dependent\ on\ the\ wall\ thickness\ (Constant)$$

$$W = weight\ of\ casting$$

The value of b is dependent on the wall thickness of the casting. In this project, it is 0.25 inches. From the Principles of Foundry Technology, the value of b is 0.87 by interpolation. Therefore,

$$R = 0.87\sqrt{4.88kg} = 1.92\frac{kg}{s} \quad (20)$$

Next, the adjusted pour rate is calculated.

$$Ra = \frac{R}{k*c} \quad (21)$$

$$Ra = adjusted\ pour\ rate$$

$$k = metal\ fluidity$$

$$c = constant\ depending\ upon\ straight\ or\ tapered\ sprue$$

The value of R can be found from the first calculation. The value of the metal fluidity is taken as unity since this project isn't cast iron. The value of c which is the friction in the gating system is dependent on a straight or tapered sprue. In this case, a taper sprue is used. Therefore,

$$Ra = \frac{1.92\ kg/s}{1*0.9} = 2.14\frac{kg}{s} \quad (22)$$

56

After the pour rate and adjusted pour rate are calculated, the area of the sprue can be calculated. This calculation is important since it the determining factor for the gating ratio. This equation can be found below.

$$As = \frac{Ra}{\rho\sqrt{2gH}} \quad (23)$$

$$As = area\ of\ sprue\ base$$

$$\rho = density\ of\ the\ molten\ metal$$

$$g = gravity$$

$$H = height\ of\ sprue\ which\ is\ assumed\ 10\ inches$$

Everything in this equation is already given above or a set value.

$$As = \frac{2.14}{2700\sqrt{2*9.81*0.254}} = 3.55\ x\ 10^{-4}\ m^2 \quad (24)$$

Since all values are found that is needed, a gating ratio is used to find the cross section for the gates and the runner. The gating ratio used in this project is 1:3:3. This is demonstrated below.

$$1:3:3$$

$$355mm^2\ x\ (3*355mm^2)\ x\ (3*355mm^2)$$

$$355\ x\ 1065\ x\ 1065\ mm^2$$

The casting contains ten gates so therefore the cross section for one gate can be found below.

$$\frac{1065}{10} = 106.5\ mm^2$$

The casting with a gating system was designed. There were four different casting which can be seen below that contain a gating system in figures 32, 33, 34, and 35.
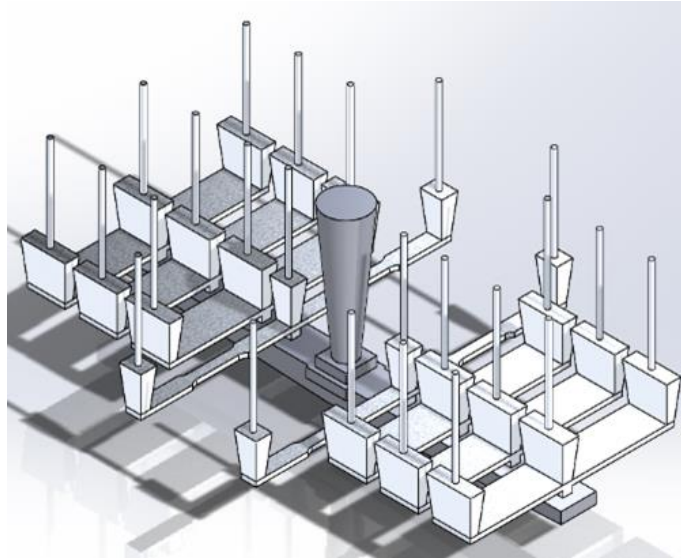
Figure 32: Drawing of 0° Casting in Solidworks
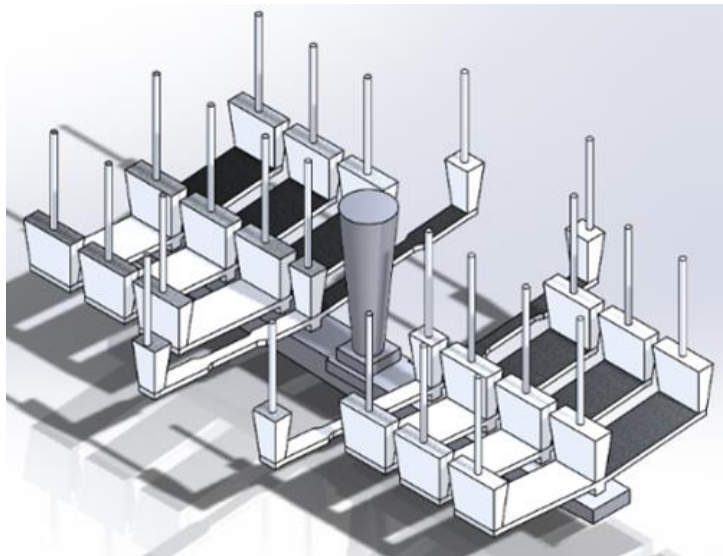
Figure 33: Drawing of 5° Casting in Solidworks
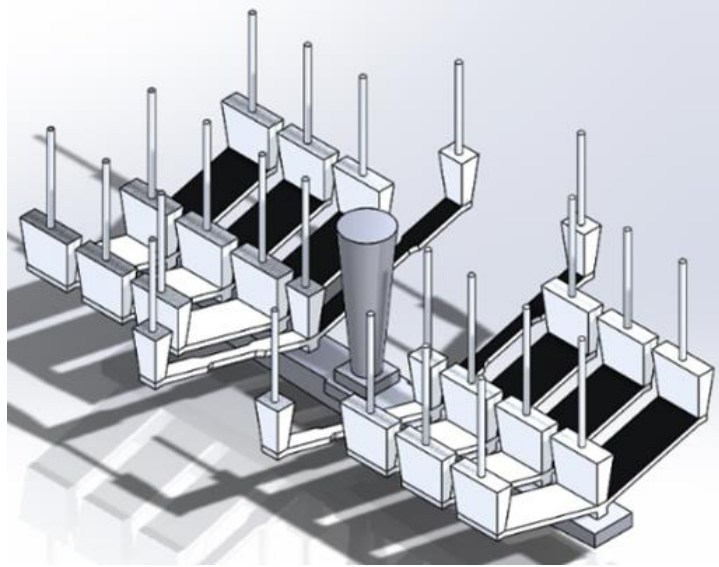
Figure 34: Drawing of 15° Casting in Solidworks
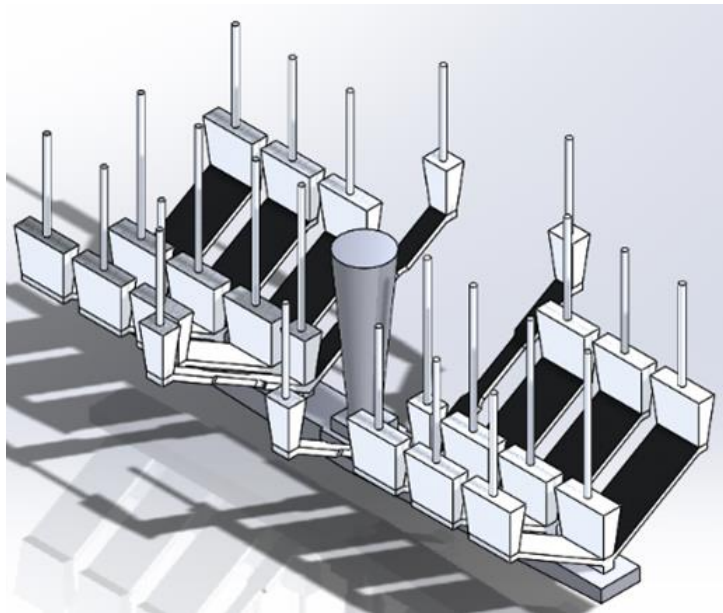
Figure 35: Drawing of 30° Casting in Solidworks

Once the casting with a gating system was constructed, a mold was designed. This mold was made to contain a filter so that any debris in the molten metal was removed before the molten metal reached the actual part. This mold was designed in solidworks. The mold contained a cope, drag and a cheek. These molds were designs with three components for easily cleanout of the mold so that the cavity was clean of any loose sand. A design of one mold can be seen below in Figures 36, 37, 38 and 39. All the molds look similar except the cavity sits at different angles to adjust for the different print orientation angles.
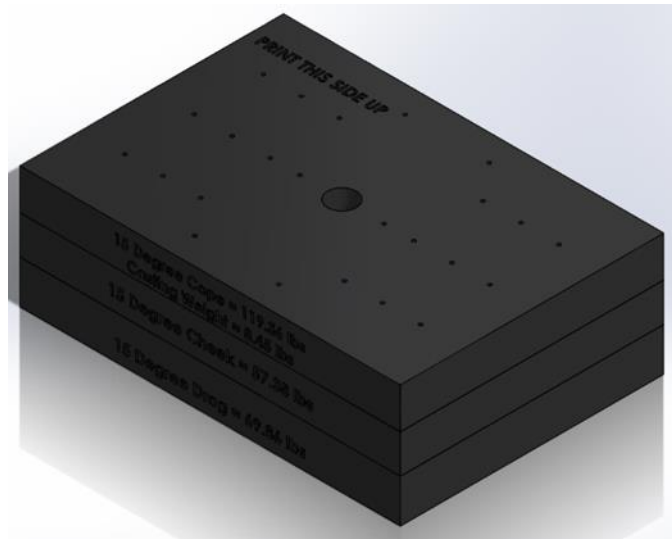
Figure 36: Sand Mold for Phase Two of Project
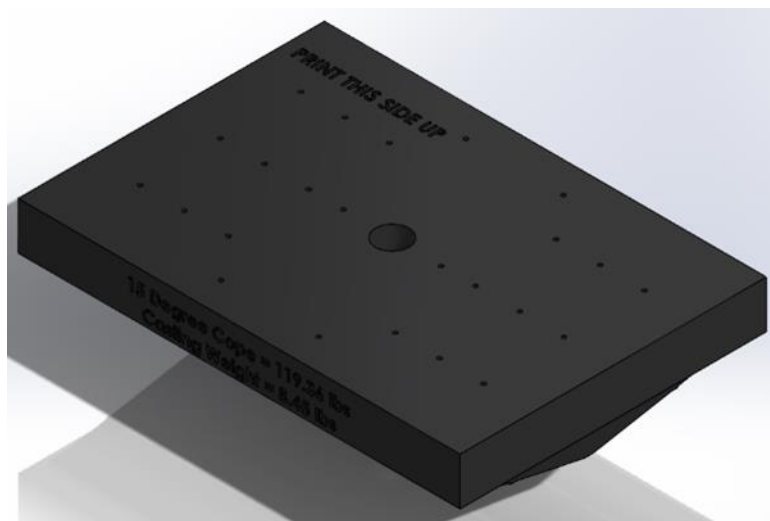
Figure 37: Cope from Sand Mold
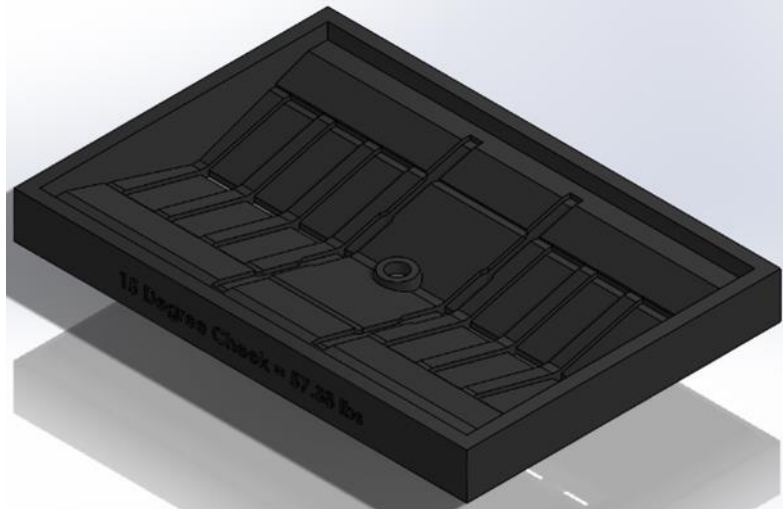
Figure 38: Cheek from Sand Mold
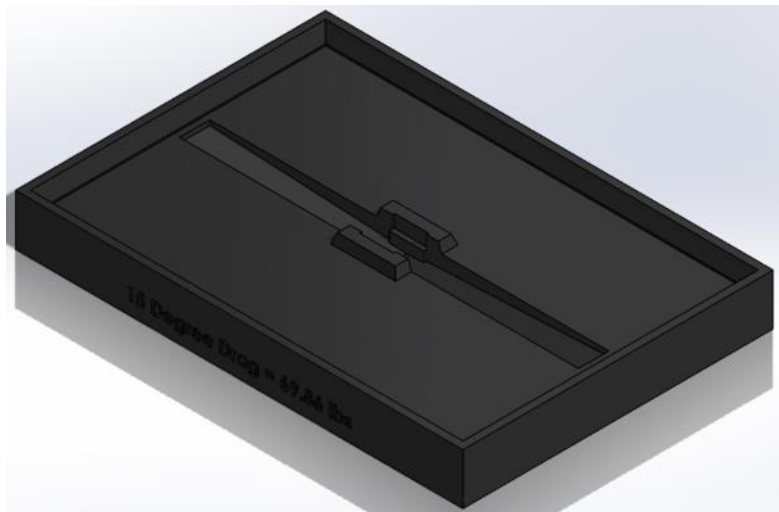
Figure 39: Drag from Sand Mold

MAGMA simulation was run on the four types of castings. The simulation did not show the mold but the casting with the gating system. The mold was formulated inside the MAGMA software. The vents were placed on the surface of each feeder in the MAGMA software geometry tab. This was to ensure that MAGMA would recognize the vents as vents when the simulation ran. A very coarse mesh was placed on the part so that it would run with accurate results. The minimum wall thickness in the casting contained at least

three mesh blocks to ensure that even the thinnest part of the casting ran properly. Below

in Figures 40, 41, 42, and 43 are the results of the MAGMA simulation for the four print

orientation angles.
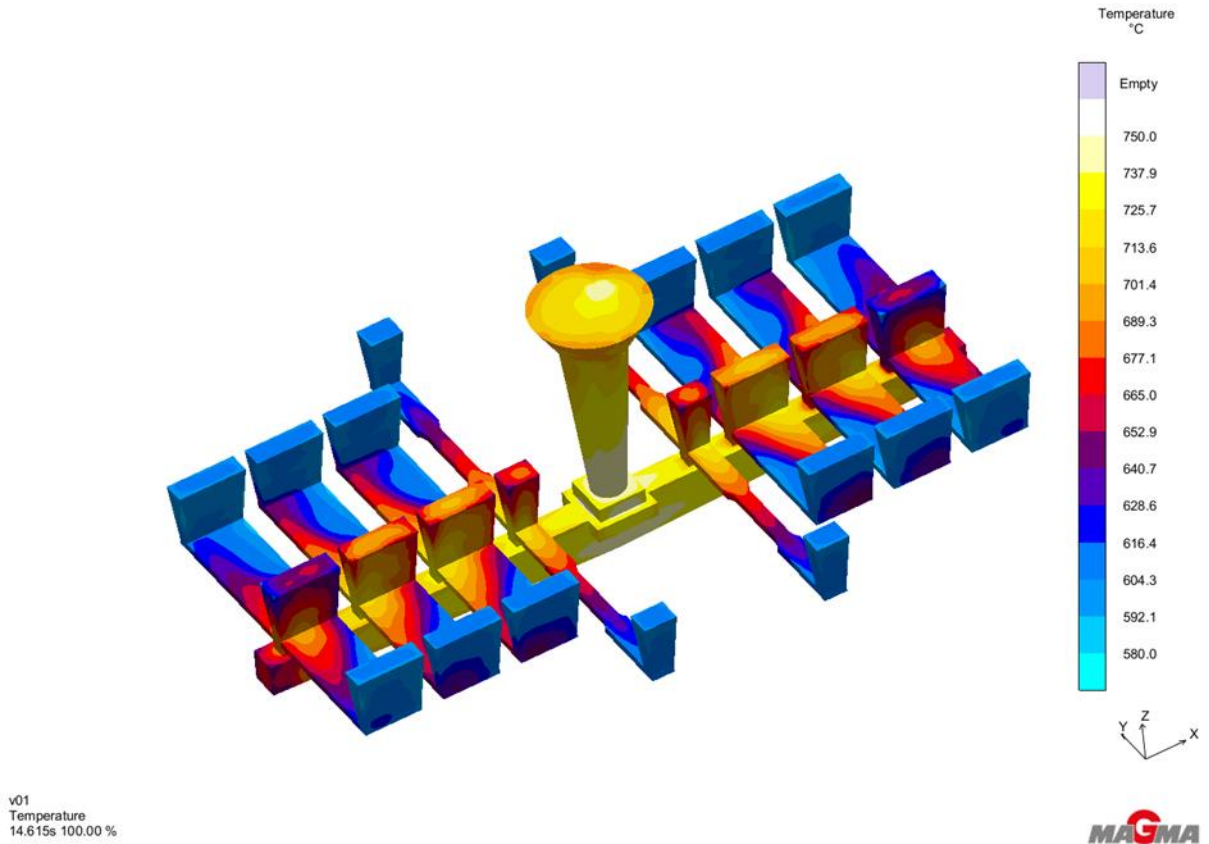
Figure 40: Pour Temperature 100% Filled on 0° Casting
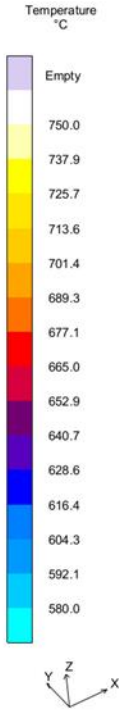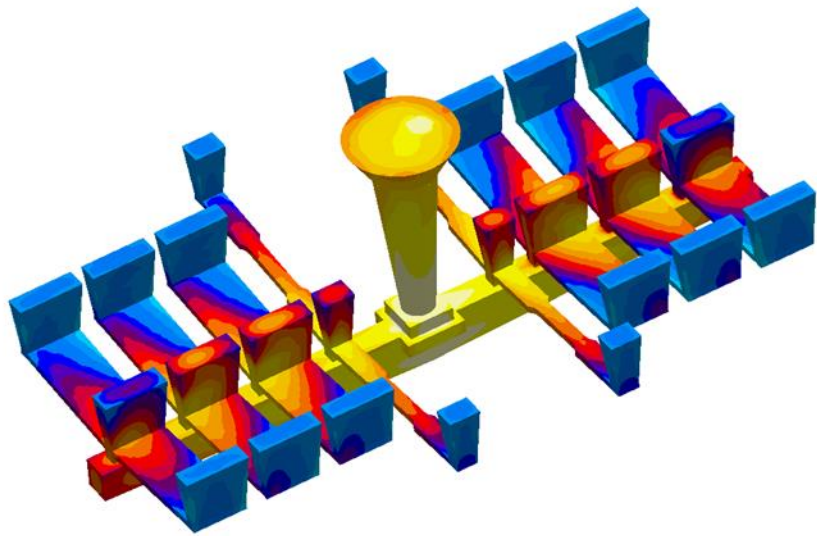
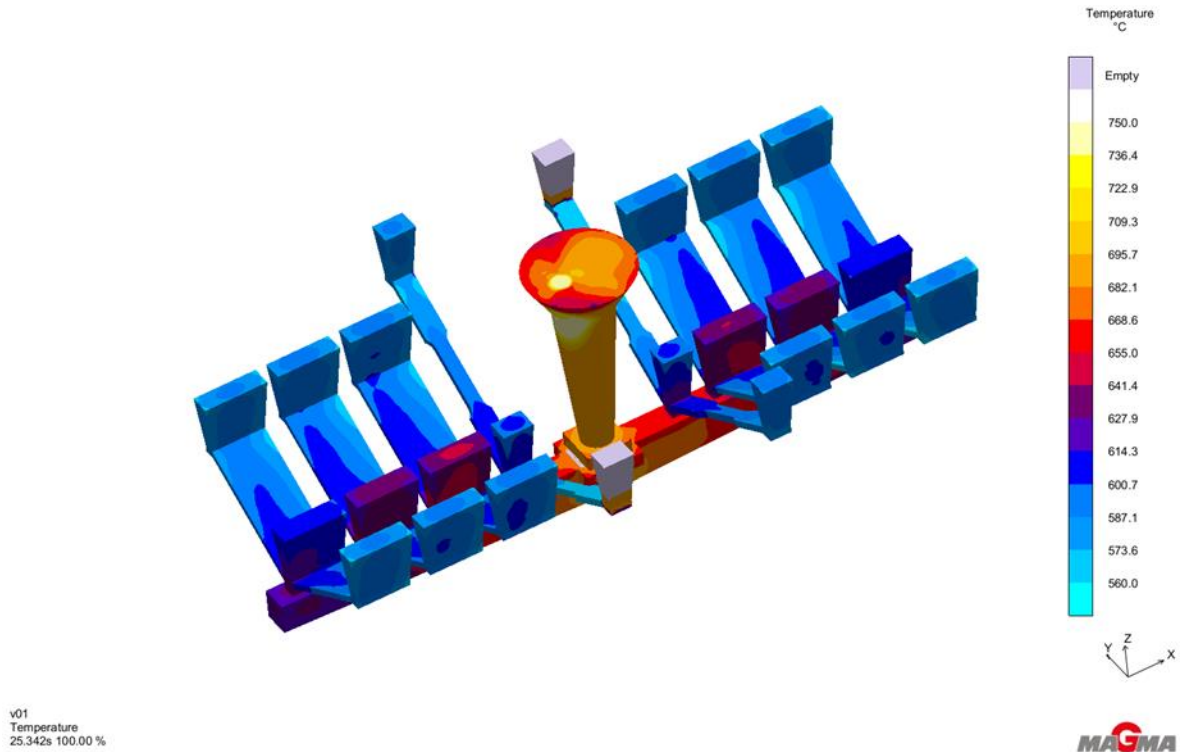*Figure 42: Pour Temperature 100% Filled 5° Casting*
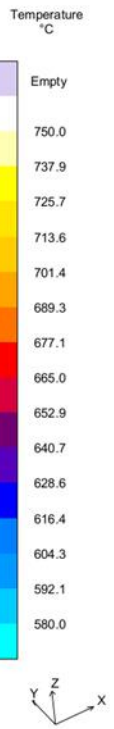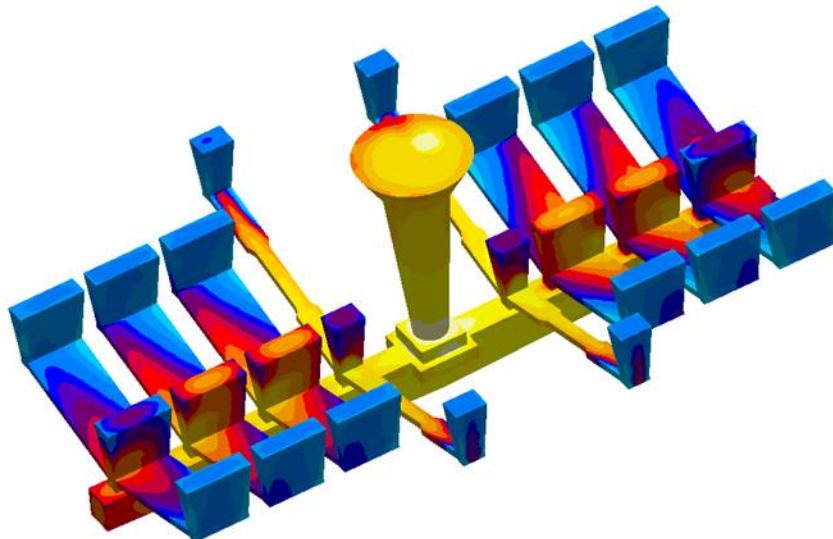
Figure 41: Pour Temperature 100% Filled 15° Casting

Figure 43: Pour Temperature 100% Filled 30° Casting

Above it can be seen the final pour temperature at 100% filled for the four castings. The feeders farthest from the runner are light blue in color which means they are already starting to solidify since they are the farthest away from the heat source of the molten metal and the ones directly on top of the runner are red and orange in color because they are still relatively hot from the pour. The molten metal when traveling through the cavity of the mold decreases in temperature as it flows since it has contacted with the atmosphere and caused it to cool down. The 30° casting simulation at 100% filled during the pour phase contained lower temperatures in the test specimens. This is because the test specimens were on an increased angle which caused an increase in the flow of the molten metal and caused the molten metal to cool down quicker.

The fraction solid result in MAGMA is extremely important in determining if this casting is going to completely pour. The blue section in the casting is the 0% fraction solid which means that most of this part is in liquid form. The feeders have already started to solidify but since the test specimens don't contain any unique colorful spots sporadically placed, then the casting can be physically poured. This can be seen in the 0°, 5° and 15° casting. However, the 30° casting has barely no liquid form except for in the runner and therefore will have a hard time filling. This can be seen in Figures 44, 45, 46, and 47.
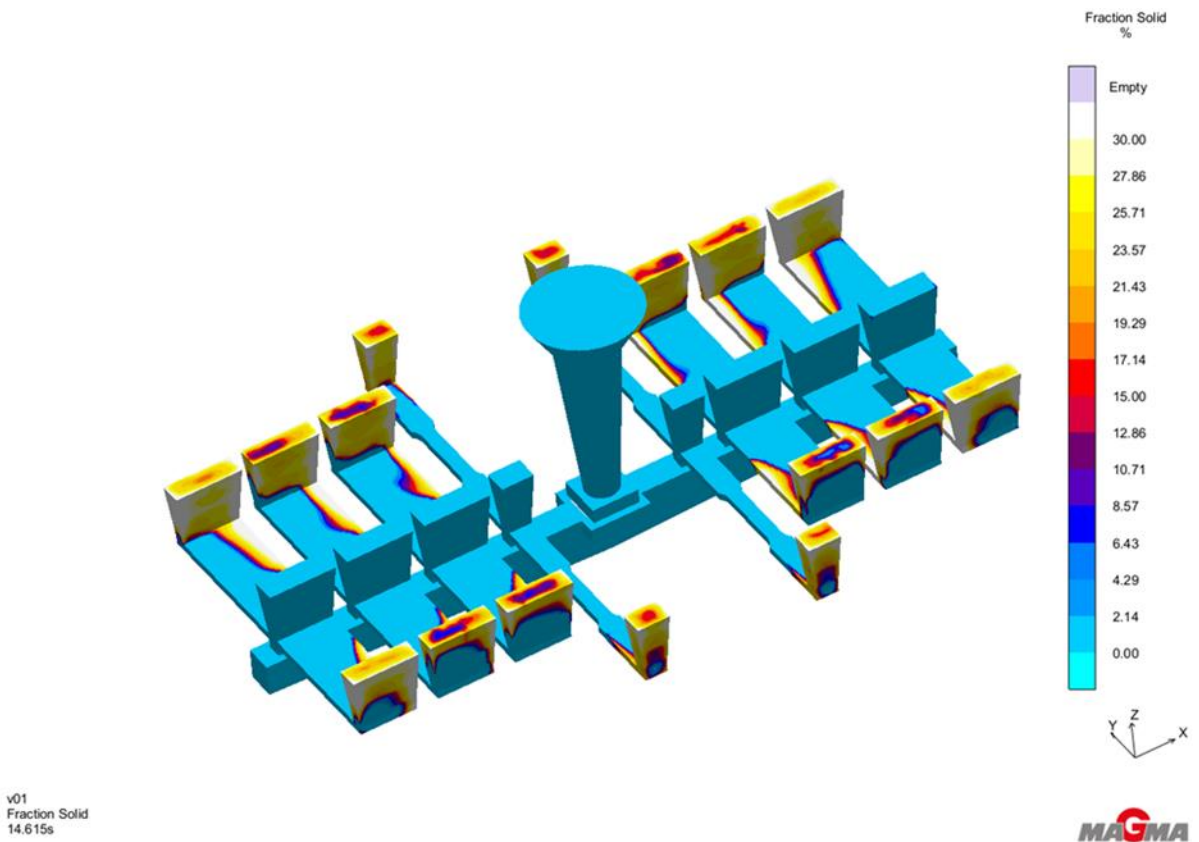
Figure 44: Pour Fraction Solid at 14.615 seconds 0° Casting
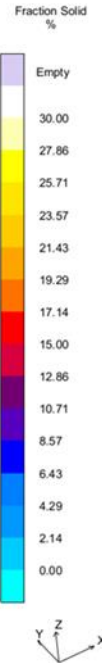
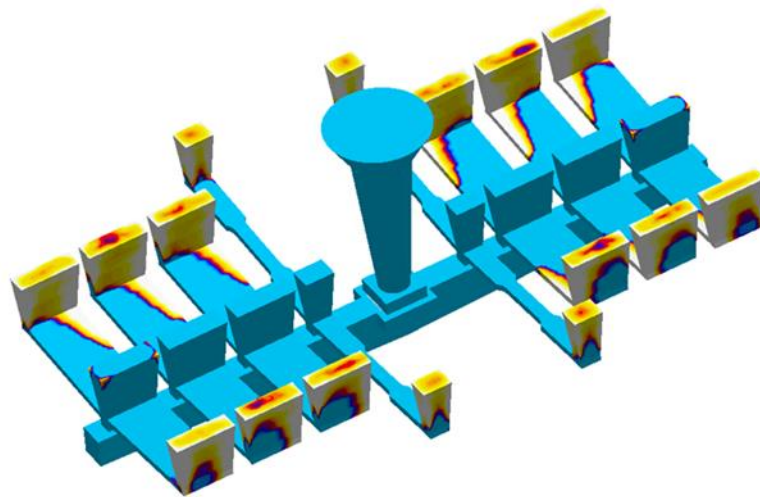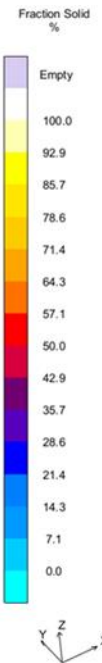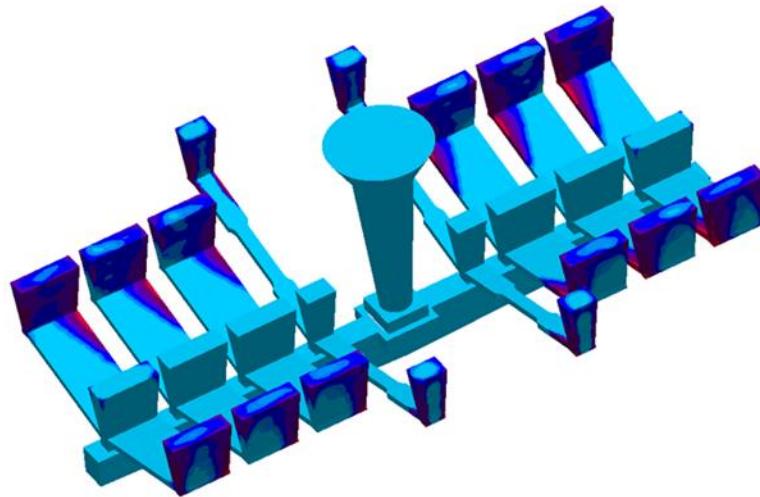*Figure 45: Pour Phase Fraction Solid at 14.606 seconds 5° Casting*

Figure 46: Pour Phase Fraction Solid at 15.014 seconds 15° Casting
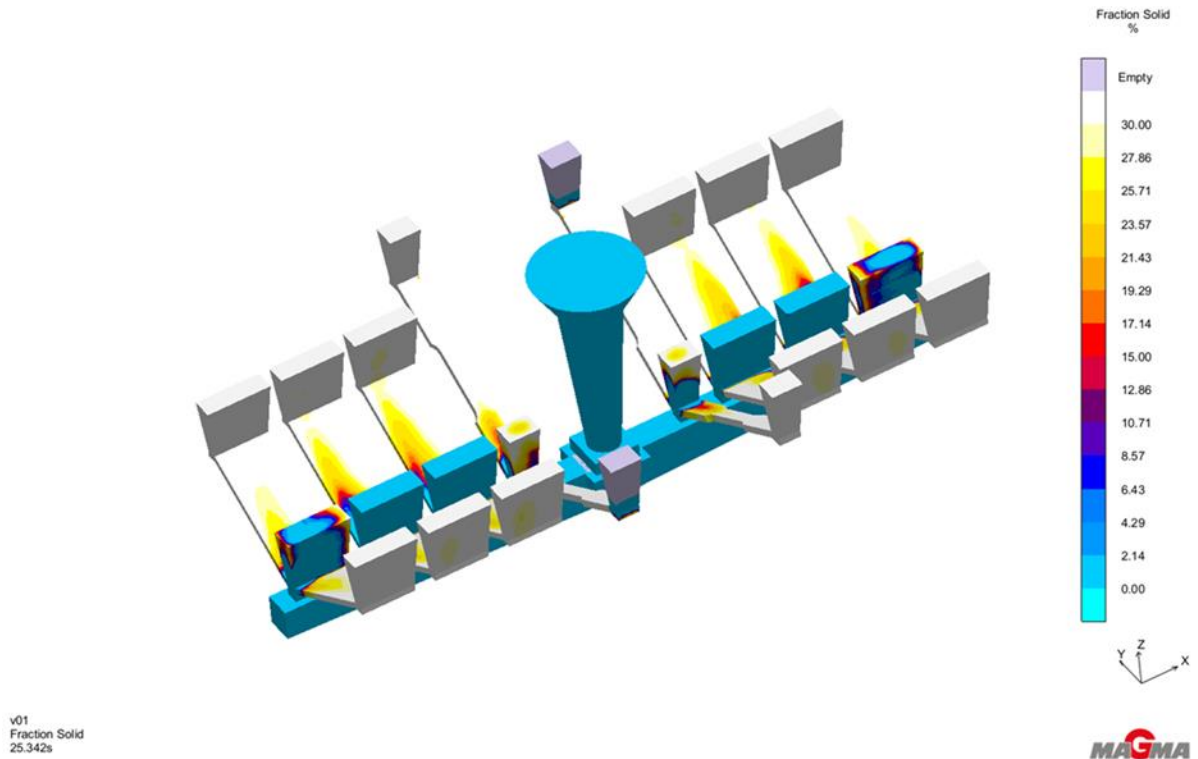
Figure 47: Pour Phase Fraction Solid at 23.342 seconds 30° Casting

Solidification took roughly two hours to simulate in MAGMA. MAGMA is set up to run until solidification is complete so therefore the results state that it will completely solidify until the temperature reaches room temperature.

Hot spots in casting is another concern that needs to be addressed before a physical pour takes place. In the figures below, these hot spots are contained in the feeders in which they should be located. This means that there is no porosity located in the part and there does not need to be additional design work to produce a good pour and casting. This can be seen in Figures 48, 49, 50 and 51.
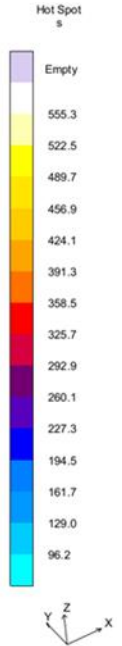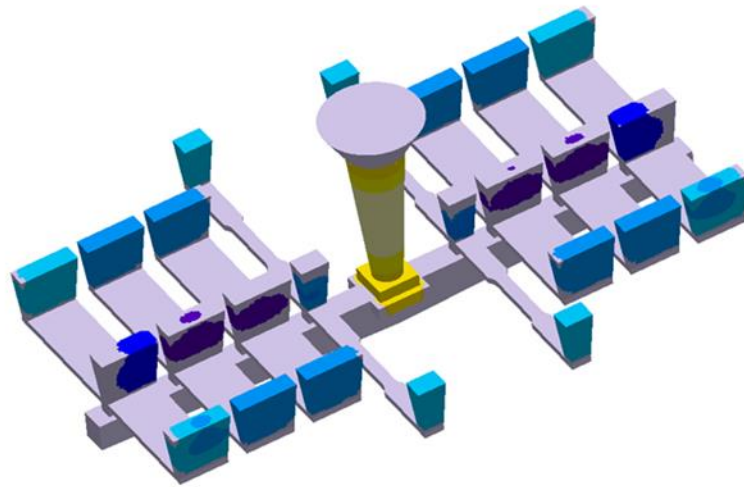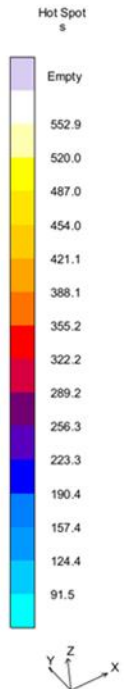
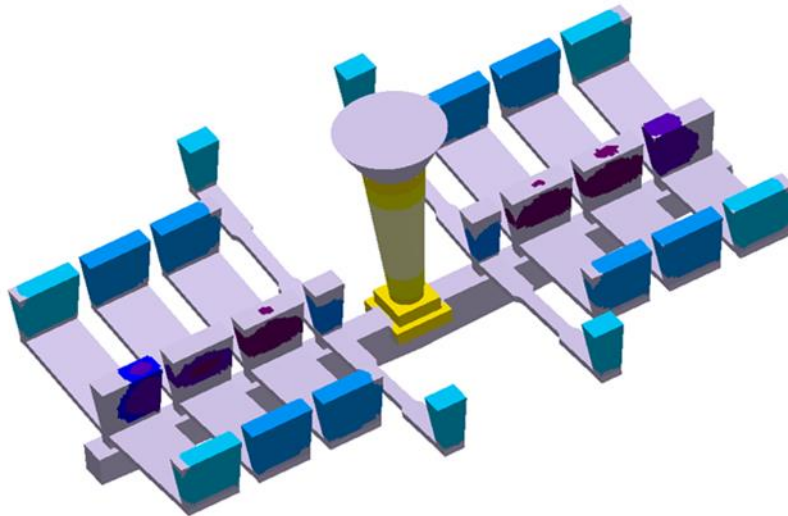*Figure 48: Hot Spots in 0° Casting*
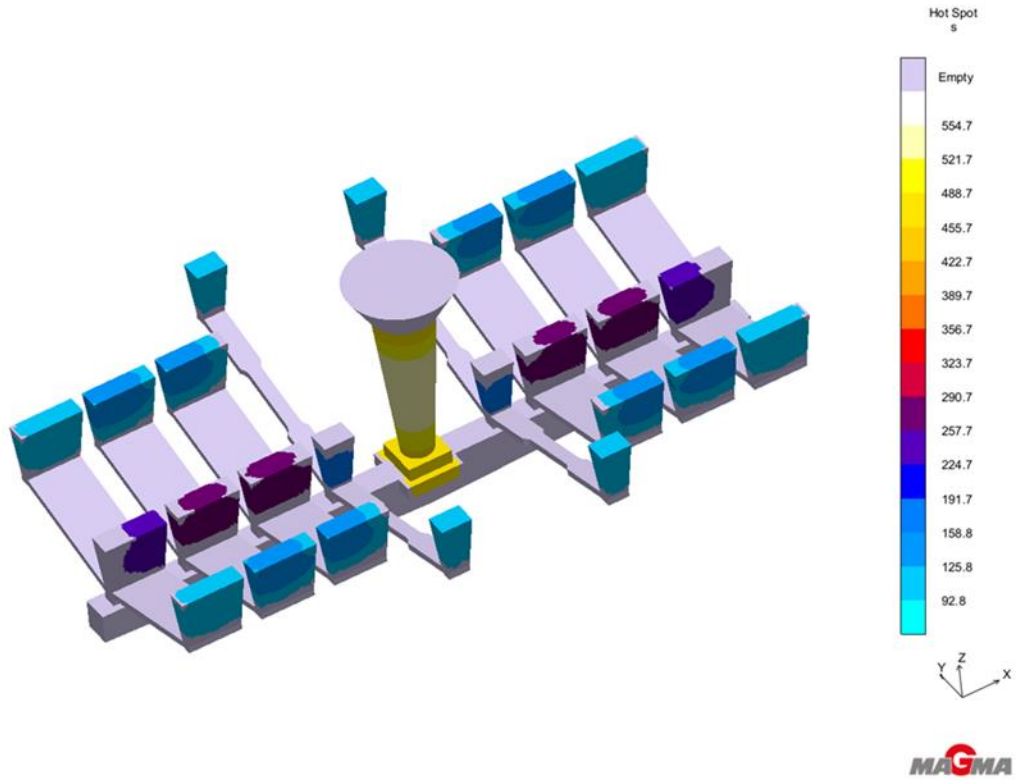

Figure 49: Hot Spots in 5° Casting

Figure 50: Hot Spots in 15° Casting
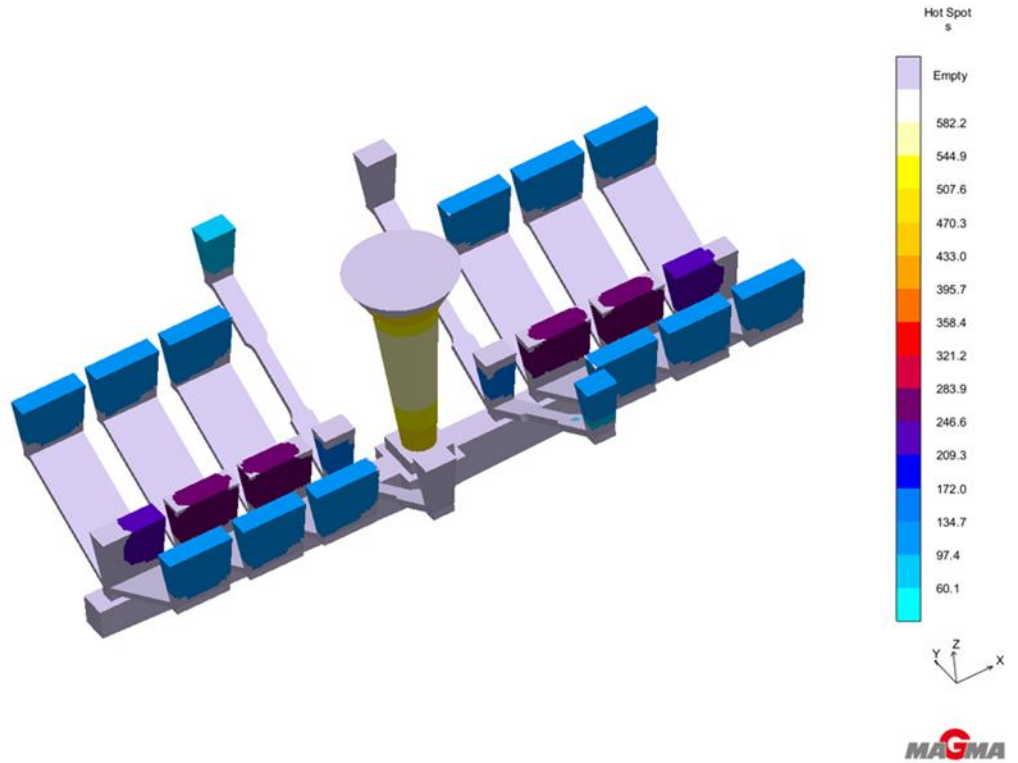
Figure 51: Hot Spots in 30° Casting

69

Once the design of the casting with gating system and molds were complete, the files were sent to Humtown in Leetonia, Ohio to be printed. These files consist of the molds that contained the cavity of the part. After the molds were finished, they were sent to Light Metals in Ravenna, Ohio to be poured using A356. The purpose to have the molds to be sent out to be poured was to establish an accurate pour to get good accurate results from the fatigue testing. However, in transportation from Leetonia to Ravenna, the cheek of mold 0° and mold 5° broke. This is due in fact that the smallest thickness of the cheek was only 0.33 inches. This can be seen below in Figure 52 and 53.
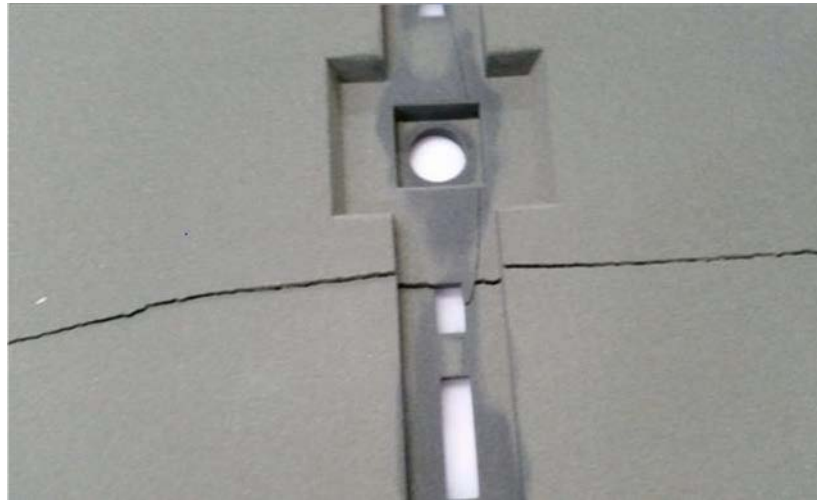
Figure 52: Breakage of 0° Cheek

Figure 53: Breakage of 5° Cheek

However, Light Metals was able to glue the cheek back together for the pour. The results

of the pour can be found below.

Figure 54: 0° Casting

Above in Figure 54 is the 0° casting. Not all feeders or vents filled. This could be

because the flat tensile bars were only a quarter inch thick that caused the molten metal to

solidify before it reached the feeders. But the flat tensile bars did fill completely since they

were the closest to the sprue and molten metal. Another possible cause of not a complete

fill was because the cheek of this mold broke towards one side of the sprue which may

have caused one sides issues over the other. Plus, the runner at the gates of the flat tensile

bars was at the maximum cross-sectional area.

Figure 55: 5° Casting

Above in figure 55 is the 5° casting. One side of the casting filled completed but not the

other. The one side that didn't fill was because this was where the crack of the cheek for

the mold happened when transporting. However, all the flat tensile and static bars were

filled which was the main concern. In this case, the vents do not need to be filled since the

main purpose is to push out the air bubbles in the casting during pour.

Figure 56: 15° Casting

Above in Figure 56 is the 15° casting. All but one set of flat static bars filled completely.

This was mainly since the entire mold was intact during assembly. There seems to be flash

between the cheek and cope which caused the distribution of metal off the flat bars. But all flat bars can be used in the fatigue testing.

Figure 57: 30° Casting

Above in Figure 57 is the 30° casting. This casting did not completely fill. The molten metal solidified before it it reached the entire flat tensile and static bars. The first two sets of flat static bars on each side of the sprue did completely fill but because of the runner being tapered it caused the last set to not completely fill. The tensile bars were too long and thin to finally fill before solidification set in on the molten A356 metal.

All four castings were completed, and the gating system was machined off. The flat bars that were still functional for tensile and fatigue testing was sent to Westmoreland Mechanical Testing and Research, Inc. The parameters for the 3-point bending fatigue is to perform 3-point bending fatigue on as-cast surface. Specimens were provided in four different conditions which are the four print orientation angles 0°, 5°, 15°, and 30°. There are 10 specimens provided for each test condition. The R-Ratio or the amplitude used is

73

0.1, the runout time is 1,000,000 cycles, the frequency is 10 hertz and the initial max test stresses are 170 and 190 MPa. The parameters for the tensile-flat bar fatigue testing are to test 12 flat, tensile specimens at room temperature.

The results of the fatigue data when sent back from Westmoreland Mechanical Testing and Research, Inc., consisted of a test log number, specimen number, measured width (inches), measured height (inches), maximum comp. stress (MPa), maximum comp. load (lbs.), minimum comp. stress (MPa), minimum comp. load (lbs.), frequency, test machine, cycles to failure and failure location. An average of all ten test specimens per angle condition was taken. Below in Figure 58 is a graph of the data.
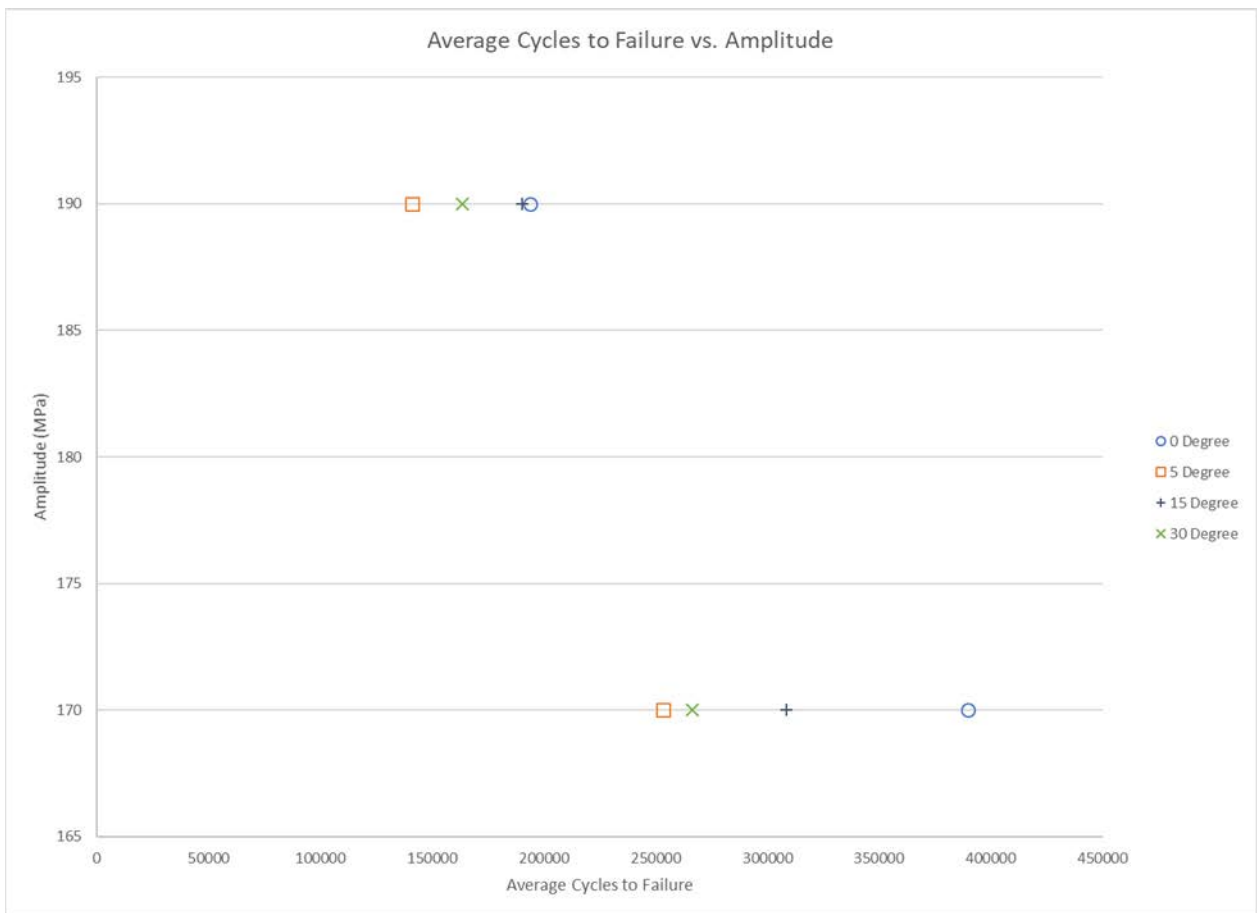

Figure 58: Average Cycles to Failure vs. Amplitude

Above, for both amplitudes 170 and 190 MPa, the 5° had the lowest number of cycles to failure. The highest number of cycles to failure for both amplitudes was 0° in which this was expected since the test specimens of 0° did not contain any stair step features.

Statistical analysis was run on the fatigue data. A simple T-Test was used and the results can be seen below in Tables 7 and 8.

Table 7: T-Test Results of 170MPa Fatigue Results

T-Test at 170MPa	t-value	p-value	Result	Significant/Not Significant
0°-5°	3.46973	0.004223	$p < 0.05$	Significant
0°-15°	1.6124	0.07277	$p < 0.05$	Not Significant
0°-30°	2.44656	0.020076	$p < 0.05$	Significant
5°-15°	-1.35758	0.105826	$p < 0.05$	Not Significant
5°-30°	-0.31794	0.379335	$p < 0.05$	Not Significant
15°-30°	0.82031	0.217898	$p < 0.05$	Not Significant

Table 8: T-Test Results of 190MPa Fatigue Results

T-Test at 190MPa	t-value	p-value	Result	Significant/Not Significant
0°-5°	1.78052	0.056431	$p < 0.05$	Not Significant
0°-15°	0.16379	0.43698	$p < 0.05$	Not Significant
0°-30°	1.67272	0.066461	$p < 0.05$	Not Significant
5°-15°	-1.80346	0.054488	$p < 0.05$	Not Significant
5°-30°	-0.92297	0.191509	$p < 0.05$	Not Significant
15°-30°	1.92147	0.045455	$p < 0.05$	Significant

After data from Westmoreland was analyzed, a scanning electron microscope (SEM) was used to review the facture surface of the test specimen. The microscope used was a JEOL Jib-4500 Multi Beam system. The use of this machine was to examine the initiation sites and striations for the cause of the crack on the surface which effect the failure of the specimen. The initiation sites and striations were investigated to determine if the stair step feature influenced the crack and fatigue of the test specimen. The two test specimens used for SEM was a 5° and a 15° test specimen. Each of these specimens were

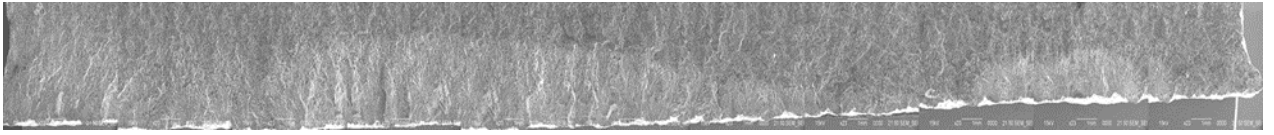conducted under an amplitude of 170MPaBelow is a view of the test specimen during SEM testing.

Figure 59: SEM Testing of 5° Fatigue Test Specimen

Above in Figure 59, is the SEM image of the fracture surface of the 5° flat bar test specimen. Two different shades are gray is present is this image. The two different shades represent where the specimen started to crack and cause failure. Towards the right side of the image, a light gray fan can be seen which demonstrates an initiation site. An initiation site is where the test specimen originally started to crack, and then multiple cracks begin to spread in a fan like feature around this site to form the light discoloration and cause the part to fail. Below in Figure 60 is this point of interest in better view.
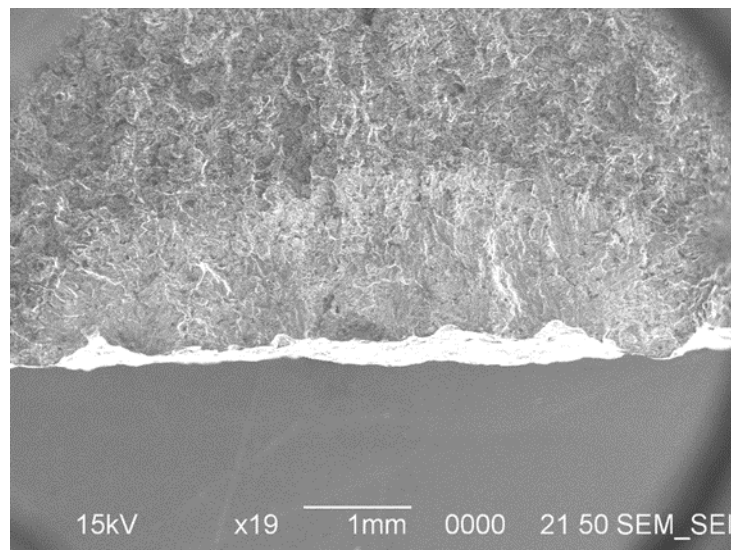

Figure 60: An Initiation Site on 5° Fatigue Test Specimen

It can be seen a few peaks that are bright white in color that are the initiation sites. There were two initiation sites that merged together to form one site of the start of failure.
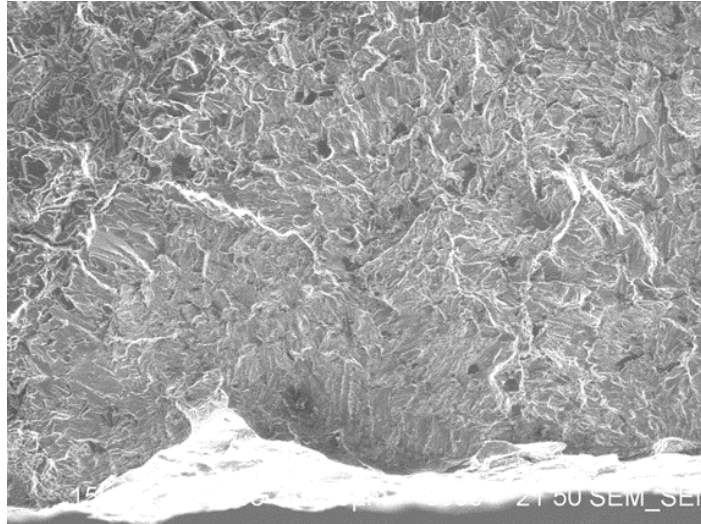
Figure 61: Spider Vein Cracks Expanding from Initiation Site on 5° Fatigue Test Specimen

Above in Figure 61, demonstrates the cracks that form from the initiation site. These are the spider veins in bright white color. These spider veins continue to grow until a crack is initiated and failure occurs within the specimen.
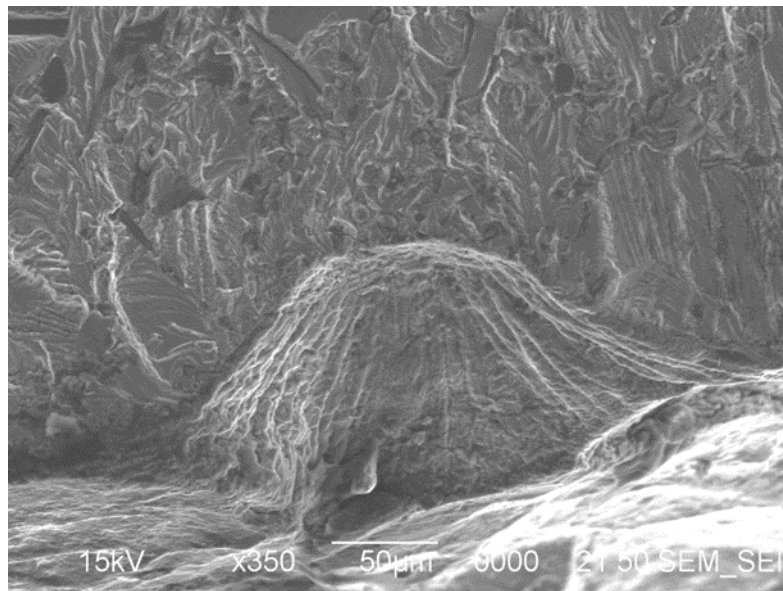

Figure 62: Striations found in 5° Fatigue Test Specimen

The striations found in the 5° fatigue test specimen can be seen above in Figure 62. The striations are the groups of lines at different orientations. The bright white in color on

the right-hand side of Figure 48 constitutes a peak present in Figure 46, therefore, it can be seen how small these striations are and how they form per grain of a material. It can be concluded that the initiation sites did occur on the stair step feature.

The same effect occurs in the 15° fatigue test specimen. Below, it one of the initiation sites found on the fracture surface of this test specimen.
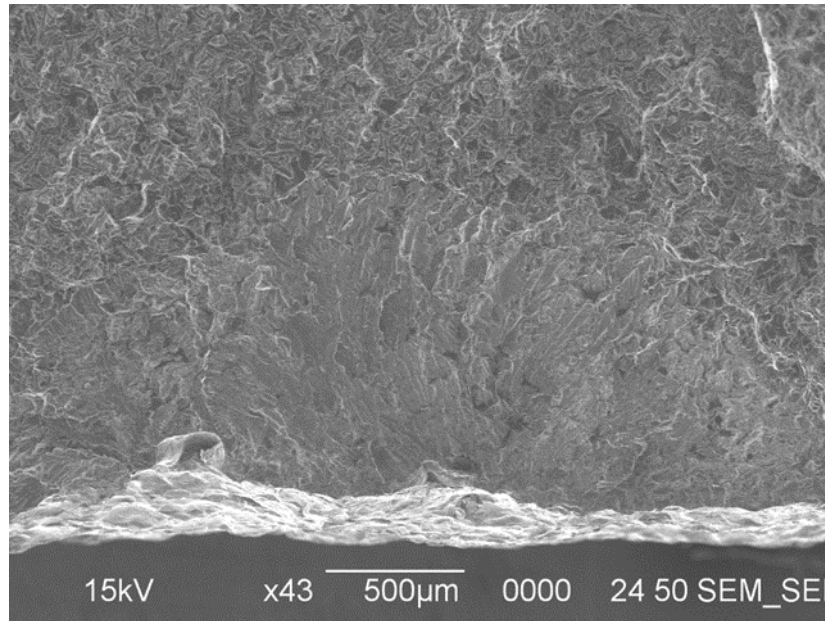
Figure 63: Initiation site for 15° Fatigue Test Specimen

The difference in the shade of grays resembles that an initiation site has occurred since a fan like feature can be seen in Figure 63.

With a more magnified view, the striation can be seen in Figure 64.

Figure 64: Striations found in 15° Fatigue Test Specimen

These striation patterns are along the crack path that occurred from the initiation site.

Below in Figure 65 demonstrates a sand particle that got displaced into the metal during the pour of A356.
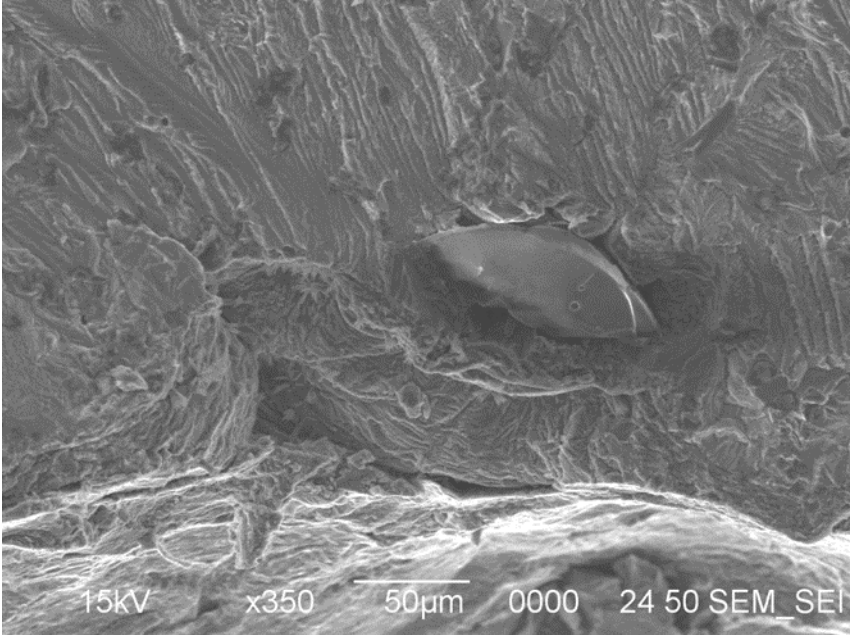
Figure 65: Debris Particle found in 15° Fatigue Test Specimen

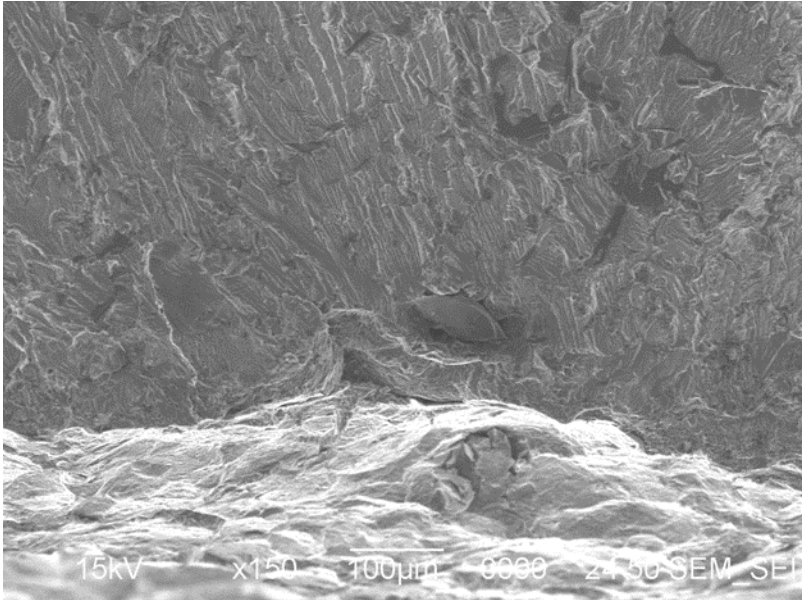This debris particle has a circular shape and is very close to the initiation site meaning that it or the pore next to it could be the source of fatigue crack initiation. . X-Ray energy dispersive spectroscopy (EDS) was performed on this image during testing. Below in Figure 66 are the results of the chemical composition of this debris particle.
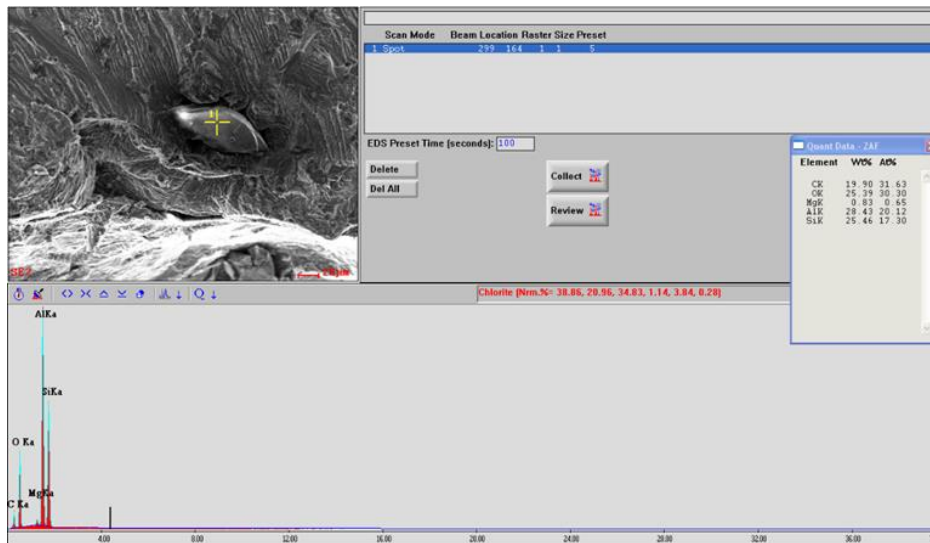
Figure 66: EDS Testing on Debris Particle

The chemical composition of this particle can be seen below in Figure 67.

Element	Wt%	At%
CK	19.90	31.63
OK	25.39	30.30
MgK	0.83	0.65
AlK	28.43	20.12
SiK	25.46	17.30

Figure 67: Chemical Composition of Debris Particle

This debris particle was high in Carbon and Oxygen for atomic percent. This confirms this particle is a sand grain from the additively manufactured sand mold. It is

assumed that during the pour of A356, sand particles broke off and got lodged into the molten metal. When it solidified, the particles were trapped and could not escape.

After SEM was tested on the fatigue parts, profilometry testing was conducted on them as well to compare the results to the Keyence and hand calculation results. A KLA-Tencor D-100 profilometer was used for measurements. A profilometer is a contact senor to measure the roughness of a part unlike the Keyence which contains no contact on the test specimen. A profilometer measures the change in height while it is being drug across the surface of a part. This measurement is a profile of the entire surface finish. A small force is applied to the surface so that no damage occurs to the measurement tip. Measurement took place on each of the angles which includes 0°, 5°, 15°, and 30°. One specimen from each group was selected to get an idea of the surface roughness at each angle. Two different tests were performed on each specimens' top surface and bottom surface. The first was vertical that of the stair step feature seen below in Figure 68.
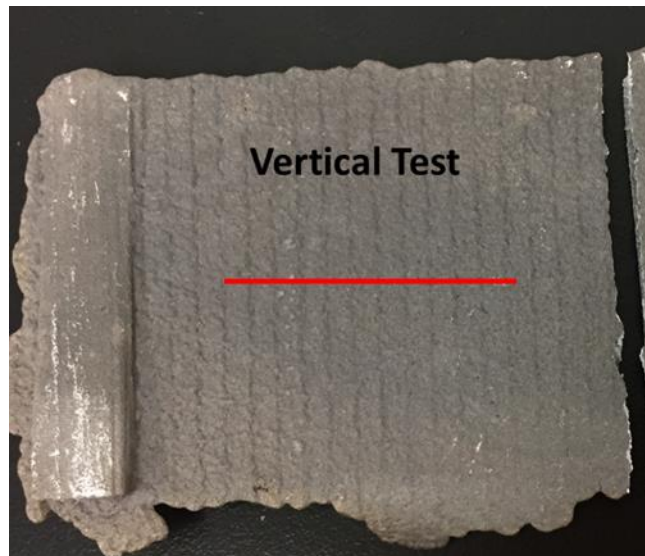
Figure 68: Vertical Test for the Profilometer

This testing demonstrated the profile across the stair step feature in which to compare to the Keyence Microscope results.

The second testing was horizontal to the stair step feature seen below in Figure 69.
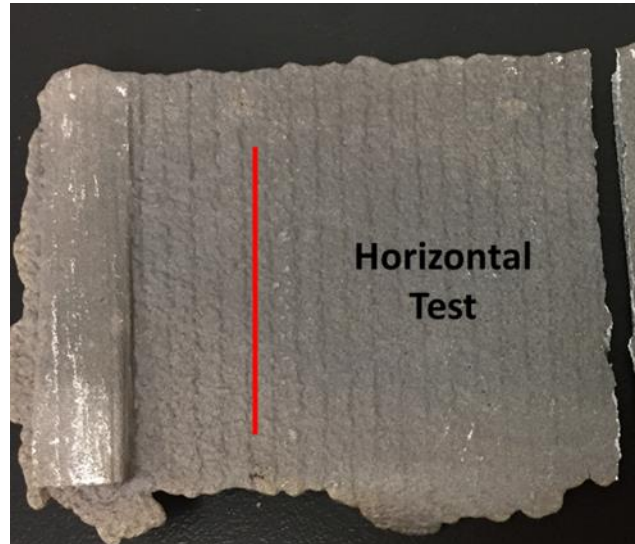
Figure 69: Horizontal Test for the Profilometer

This testing occurred on a stair step feature to determine the difference between each stair step feature.

The results of this testing can be seen below in Figure 70.
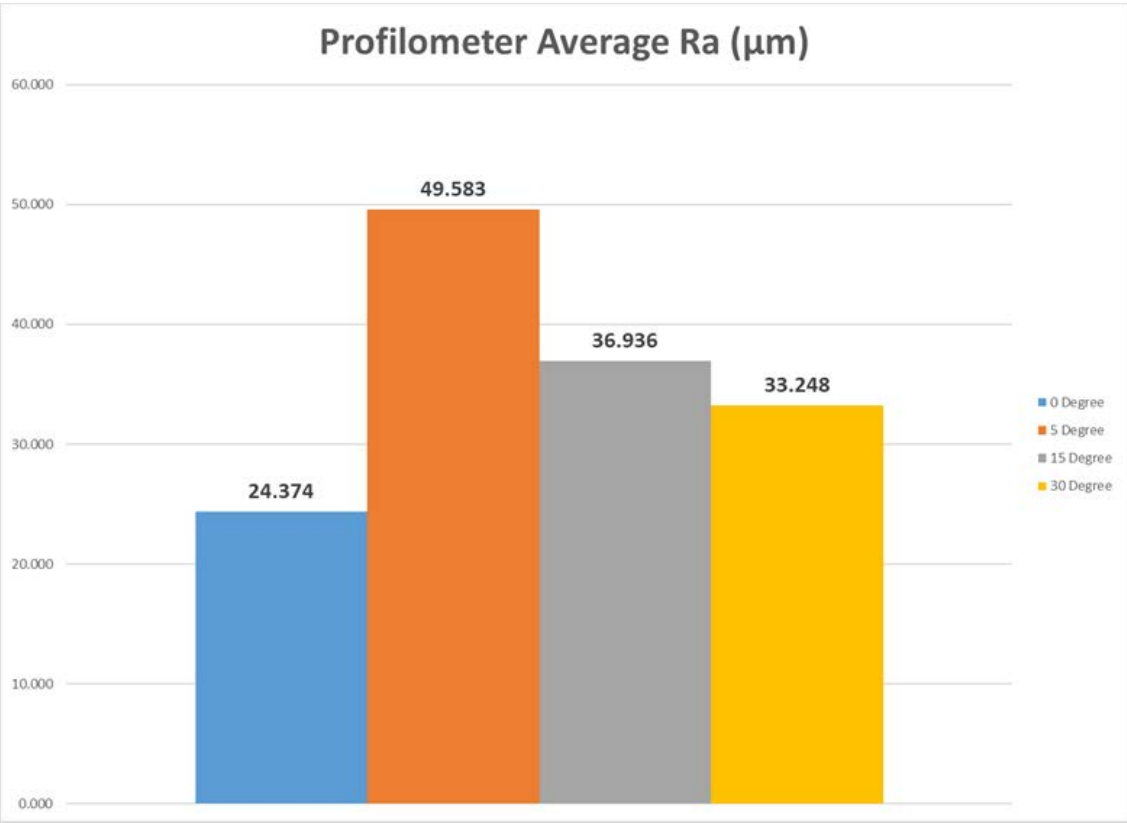
Figure 70: Profilometer Average Ra (μm)

The average of the profilometer reading at vertical and horizontal down as well as vertical and horizontal up were compiled. From these results, 5° has the highest surface roughness which is expected since it has the most visible of the stair step features. The average R_q values have the same pattern as the average Ra for the given angles and can be seen below in Figure 71.
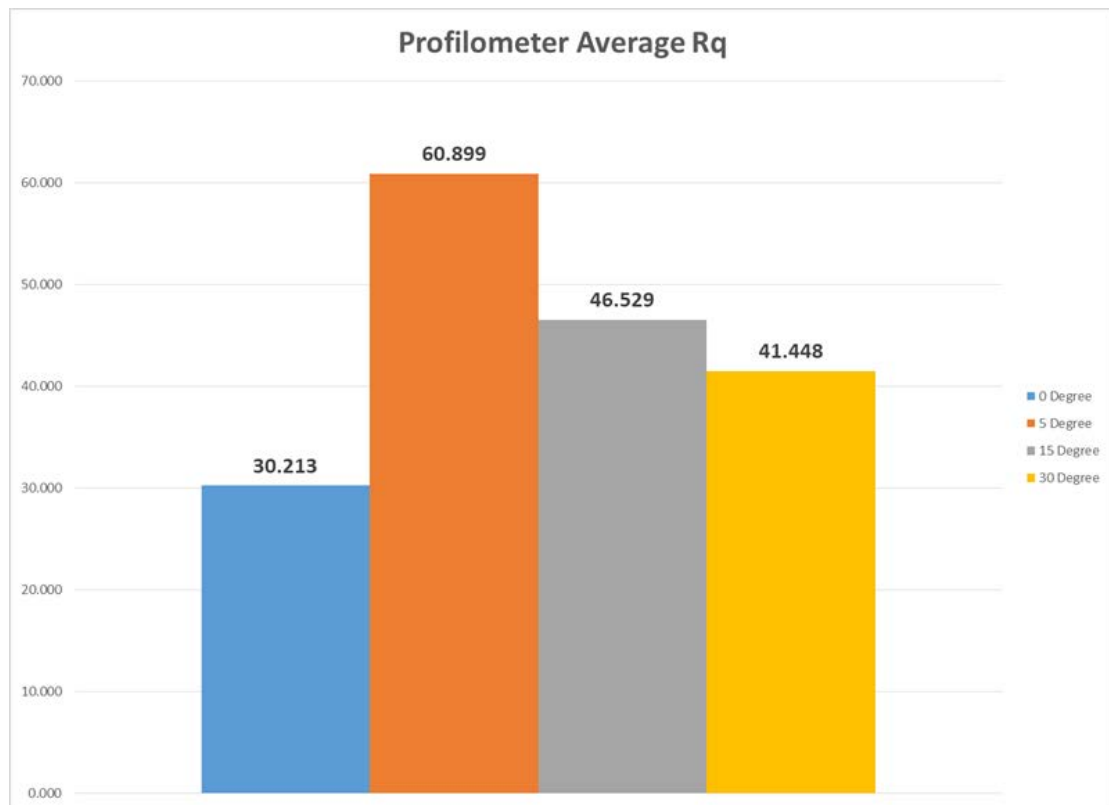
Figure 71: Profilometer Testing Average R_q (μm)

Below in Figures 72, 73, 74 and 75 is a comparison of the Keyence Data with the Profilometer testing per given angle of the two different parameters, non-coated up and non-coated down.
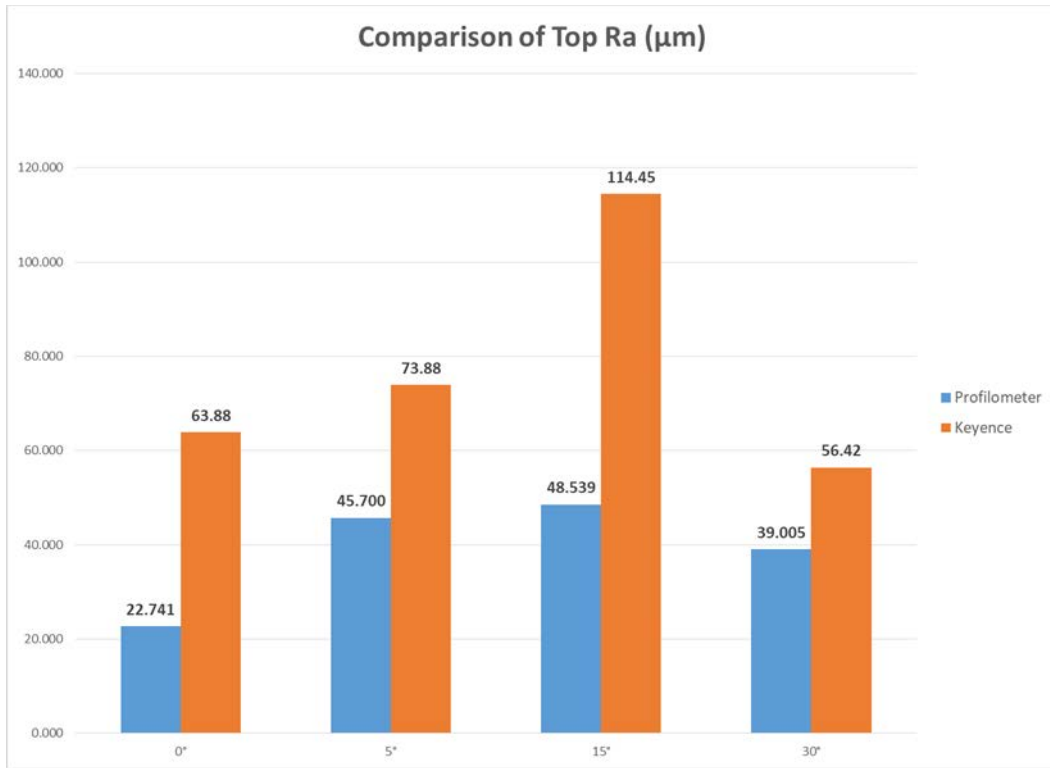
Figure 73: Comparison of Top R_a (µm)
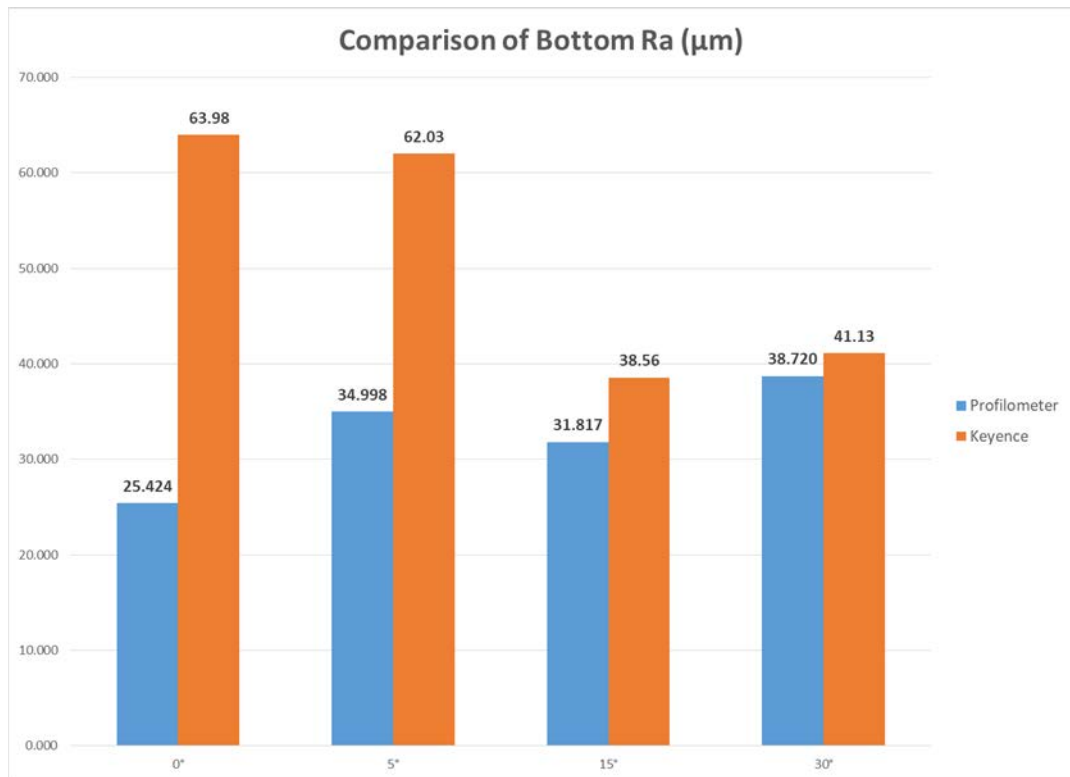
Figure 72: Comparison of Bottom R_a (µm)

85
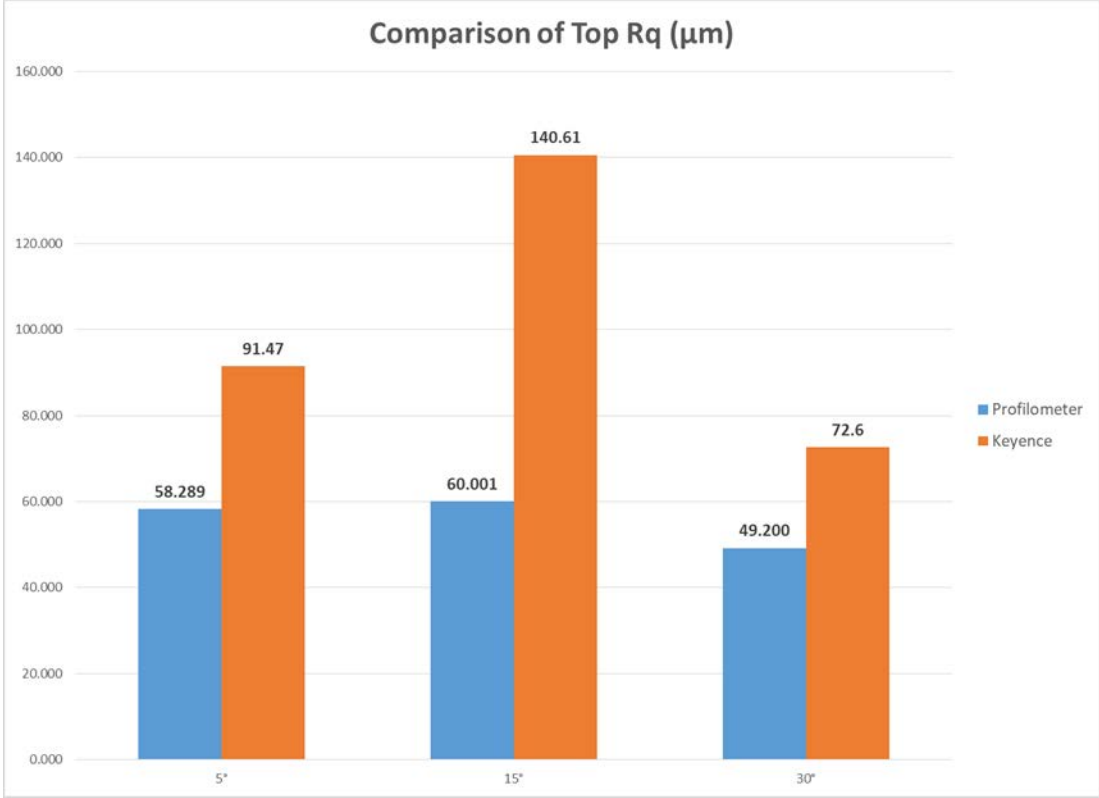
Figure 75: Comparison of Top R_q (µm)
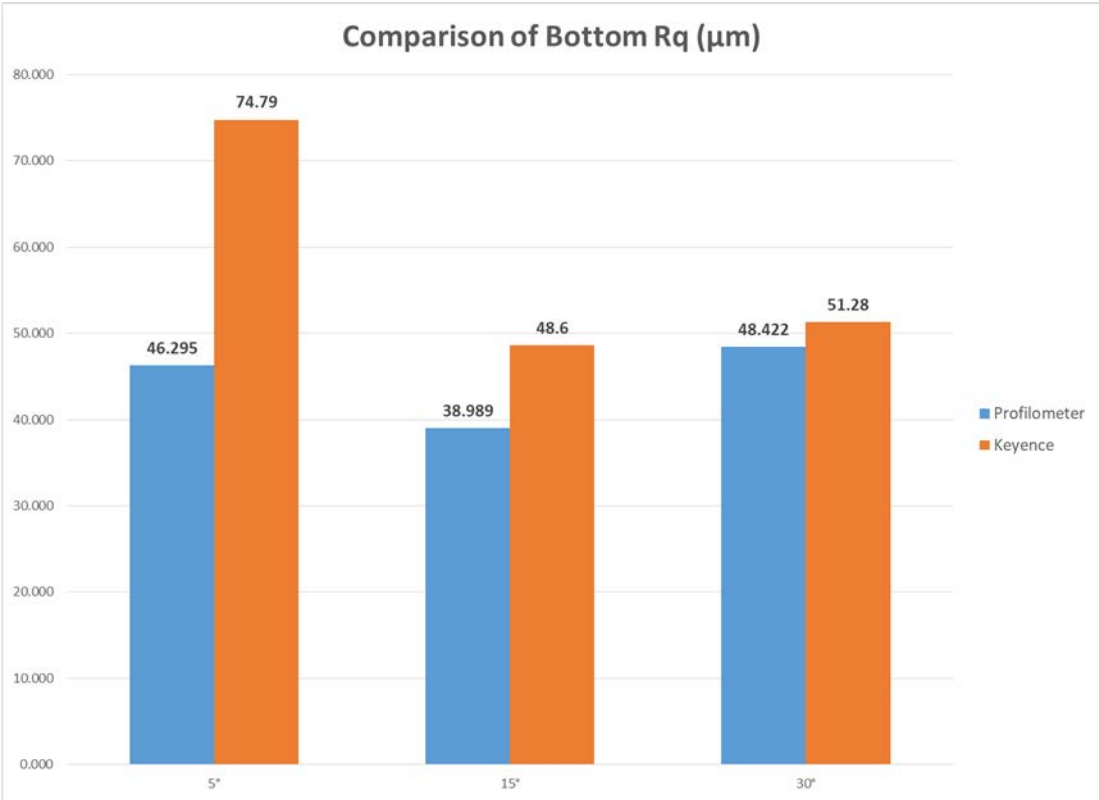
Figure 74: Comparison of Bottom R_q (µm)

From the above results, the Keyence data is higher than the profilometer data. This is due in part that the Keyence data was taken with a non-contact probe to where the profilometer was taken with a contact probe which is much accurate since the surface quality is very rough. Also, the bottom Ra and Rq was lower than the top Ra and Rq. This is because when additively manufacturing a sand mold, the bottom parts build up more pressure on the surface of the benchmark casting and resulted in a smoother finish. The bottom parts also had more time to cure with the binder that resulted in less particles falling off and causing an uneven surface finish.

These results are now compared to the hand calculations done in phase 1 of this project. They can be seen below in Figures 75 and 76.
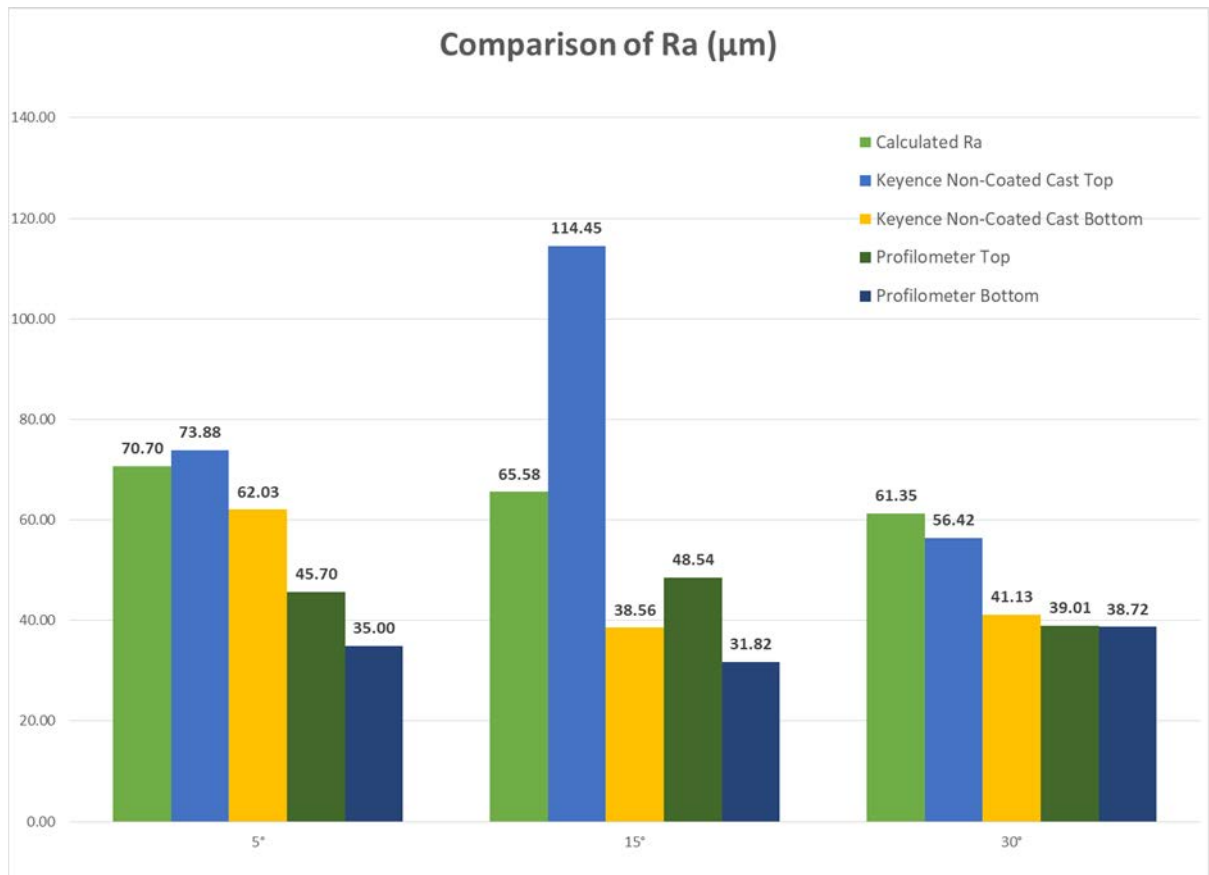
Figure 76: Comparison of all Methods of R_a (μm)
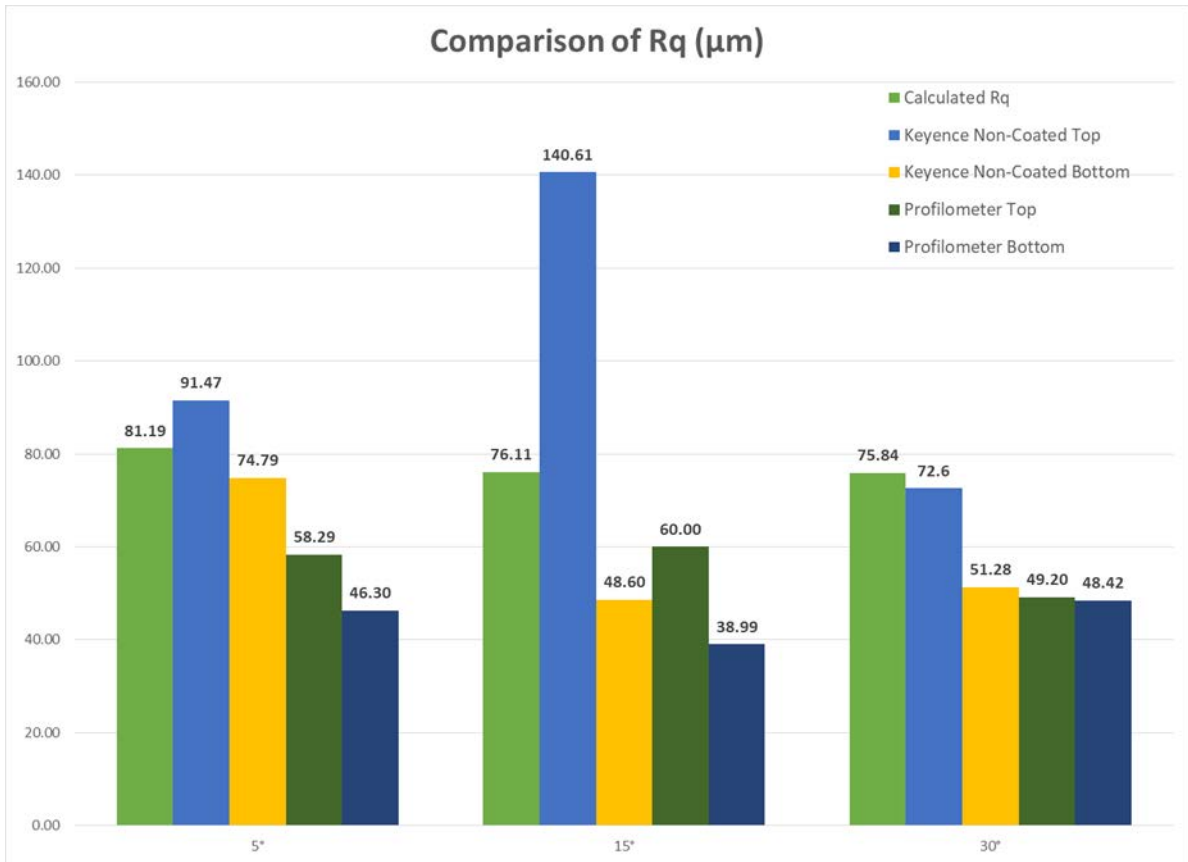
Figure 77: Comparison of all Methods of R_q (µm)

Above in Figures 76 and 77, can be seen all methods: hand calculation, Keyence data and Profilometer data compile into one table to do a comparison of all methods to receive an accurate resemblance of the surface quality of the parts when using additively manufacutred sand molds. The hand calculations are high when compared to both the Keyence and the Profilometer. However, the Keyence non-coated top is the highest in the 5° and the 15° and this can be due that both of these angles contain a visible stair step feature. The profilometer data has the lowest values in Ra and Rq when tested on the bottom of the part. The profilometer testing is then considered the most accurate since it has a contact probe to test the surface quality and no human errors can be made in the process.

Next, fractography was conducted on the fatigue test specimens. One parts was used per each degree to compare the surface quality to that of a comparitive plate. A cast Microfinish Comparator C-9 plate was used for this testing as seen in Figure 78.

Figure 78: Comparative Plate

Next, each angle was compared to this plate by feel and vision.

Figure 79: 0° Fatigue Test Specimen for Fractography

Above in Figure 79, is a 0° plated used to compare with the comparative plate. After vision and feel testing, this had an RMS as of 420. The additive manufactured mold causes the cast part to have surface roughness due to the grain finess of the sand.

Below in Figure 80, is the 5° fatigue test specimen that is compared to the comparative plates for fractography.
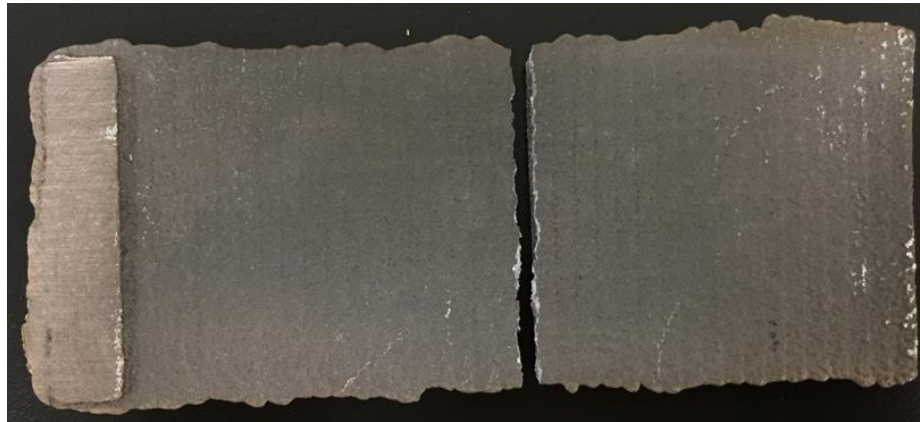
Figure 80: 5° Fatigue Test Specimen for Fractography

This 5° fatigue test specimen has an RMS of 720 when compared to the comparative plate.

The 15° fatigue test specimen has an RMS of 720 when compared to the comparative plate and can be seen below in Figure 81.
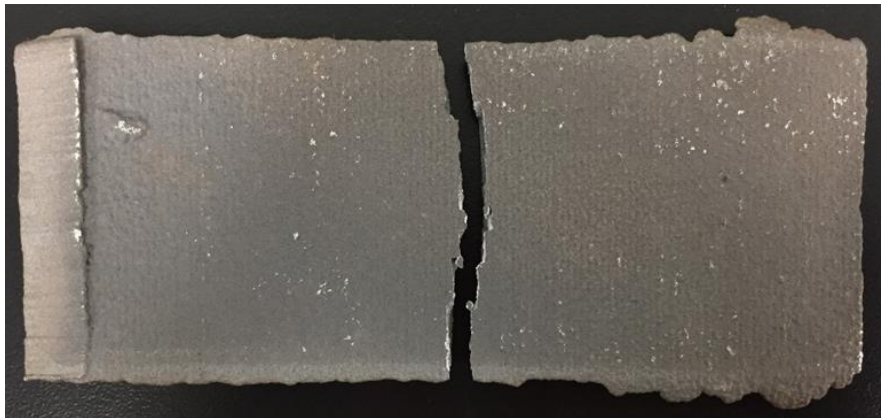
Figure 81: 15° Fatigue Test Specimen for Fractography

Lastly, the 30° fatigue test specimen has an RMS of 560 when compared to the comparative plate and can be seen below in Figure 82.

Not all forty fatigue test specimens were compared to the comparative for fractography since each angle group had the same surface finish. There are no stair step
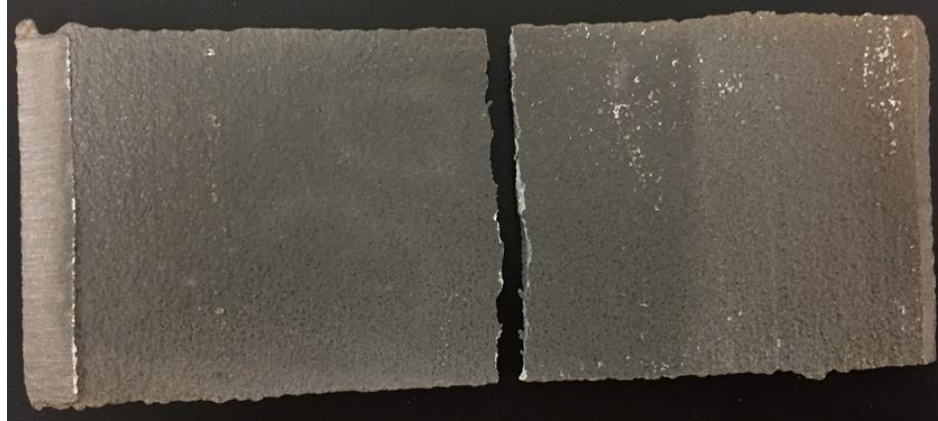
Figure 82: 30° Fatigue Test Specimen for Fractography

features demonstrated in the comparative plates which hinders the vision portion for fractography. Most of determining the RMS value was strictly by feel.

4.3 Phase 3 – Fluorescent Penetrant Inspection Testing Results

The third phase of this project was to perform fluorescent penetrant inspection testing on a redesign casting with gating system and mold. This can be seen below in Figure 83.
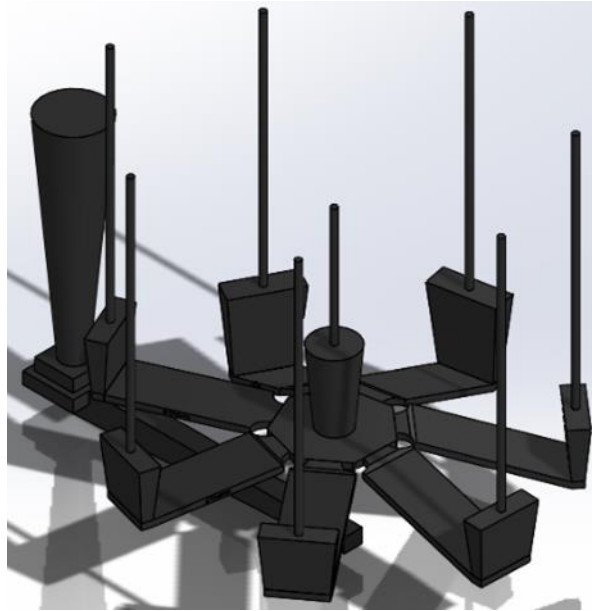
Figure 83: Drawing of Fluorescent Penetrant Inspection Casting in Solidworks

The first calculation is to determine the pour rate of the molten metal.

$$R = b\sqrt{W}$$

$$R = the\ pour\ rate$$

$$b = dependent\ on\ the\ wall\ thickness\ (Constant)$$

$$W = weight\ of\ casting$$

The value of b is dependent on the wall thickness of the casting. In this project, it is 0.25 inches. From the Principles of Foundry Technology, the value of b is 0.87 by interpolation. Therefore,

$$R = 0.87\sqrt{4.85kg} = 1.29\ kg/s$$

Next, the adjusted pour rate is calculated.

$$Ra = \frac{R}{k * c}$$

$$Ra = adjusted\ pour\ rate$$

$$k = metal\ fluidity$$

$$c = constant\ depending\ upon\ straight\ or\ tapered\ sprue$$

The value of R can be found from the first calculation. The value of the metal fluidity is taken as unity since this project isn't cast iron. The value of c which is the friction in the gating system is dependent on a straight or tapered sprue. In this case, a taper sprue is used. Therefore,

$$Ra = \frac{1.29\ kg/s}{1 * 0.9} = 1.43\ kg/s$$

After the pour rate and adjusted pour rate are calculated, the area of the sprue can be calculated. This calculation is important since it the determining factor for the gating ratio. This equation can be found below.

$$As = \frac{Ra}{\rho\sqrt{2gH}}$$

$$As = area\ of\ sprue\ base$$

$$\rho = density\ of\ the\ molten\ metal$$

$$g = gravity$$

$$H = height\ of\ sprue\ which\ is\ assumed\ 10\ inches$$

Everything in this equation is already given above or a set value.

$$As = \frac{1.29}{2700\sqrt{2 * 9.81 * 0.254}} = 2.38\ x\ 10^{-4}\ m^2$$

93

The area at the base of the sprue is $2.38 \ x \ 10^{-4} m^2$. Therefore, the radius of the circle at the base of the sprue is

$$As = \pi r^2$$
$$2.38 \ x \ 10^{-4} = \pi r^2$$
$$r = \sqrt{\frac{2.38 \ x \ 10^{-4}}{\pi}}$$
$$r = 0.0087 \ meters$$

Since all values are found that is needed, a gating ratio is used to find the cross section for the gates and the runner. The gating ratio used in this project is 1:3:3. This is demonstrated below.

$$1 : 3 : 3$$

$$238mm^2 \ x \ (3 * 238mm^2) \ x \ (3 * 238mm^2)$$

$$355 \ x \ 714 \ x \ 714 \ mm^2$$

Once the casting with gating system was completed, a mold with this as a cavity was designed. Three components of the mold were constructed to enhance easy cleanout of the mold and cavity. This is to ensure that no loose sand got into the molten metal when poured and cause an inaccurate reading. Below is the mold as seen in Figure 84, 85 and 86.
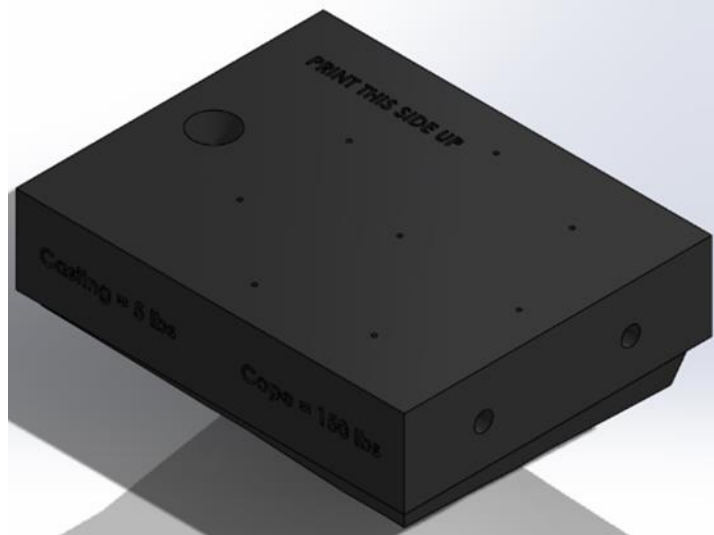
Figure 84: Drawing of Cope for Fluorescent Penetrant Inspection Testing
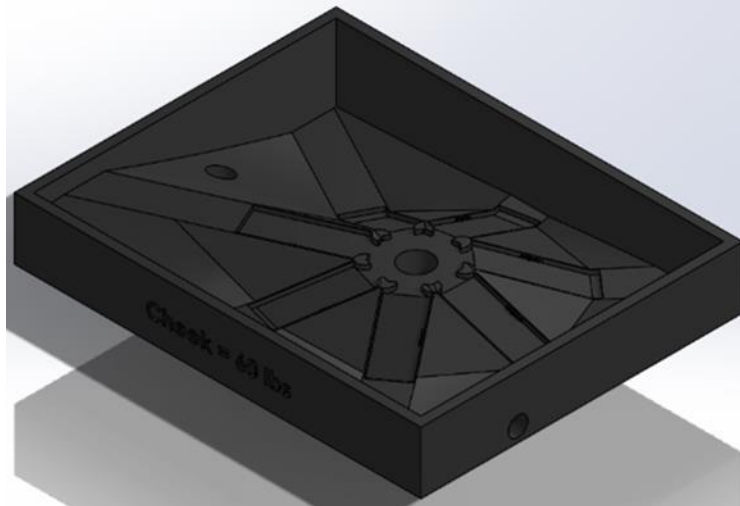
Figure 85: Drawing of Cheek for Fluorescent Penetrant Inspection Testing
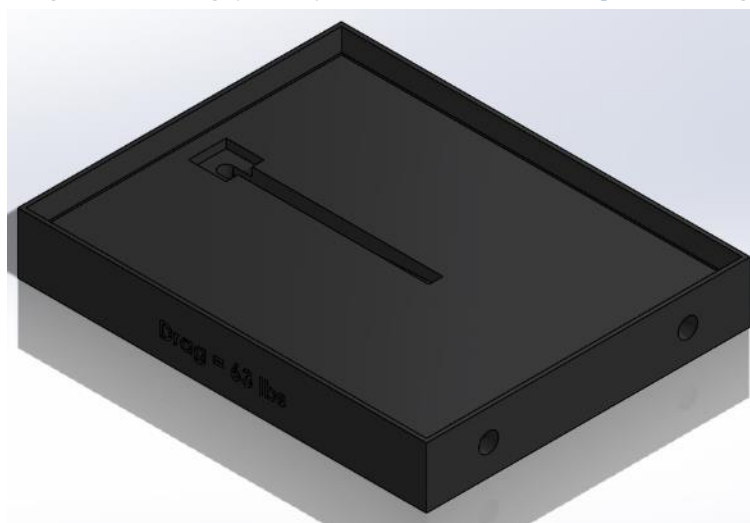
Figure 86: Drawing of Drag for Fluorescent Penetrant Inspection Testing

95

The casting with gating system was completed and the mold was constructed. MAGMA simulation was run on the casting with gating system. MAGMA results were formulated and pour temperature, pour fraction solid, solidification temperature and solidification fraction solid were analyzed. The pour temperature is the temperature the molten metal was during the pour before solidification takes place. The pour fraction solid is at what percentage of the casting is solid and what is liquid. The solidification temperature and solidification fraction solid have the same function as in the pour but in the solidification stage. These results can be found below in Figure 87.
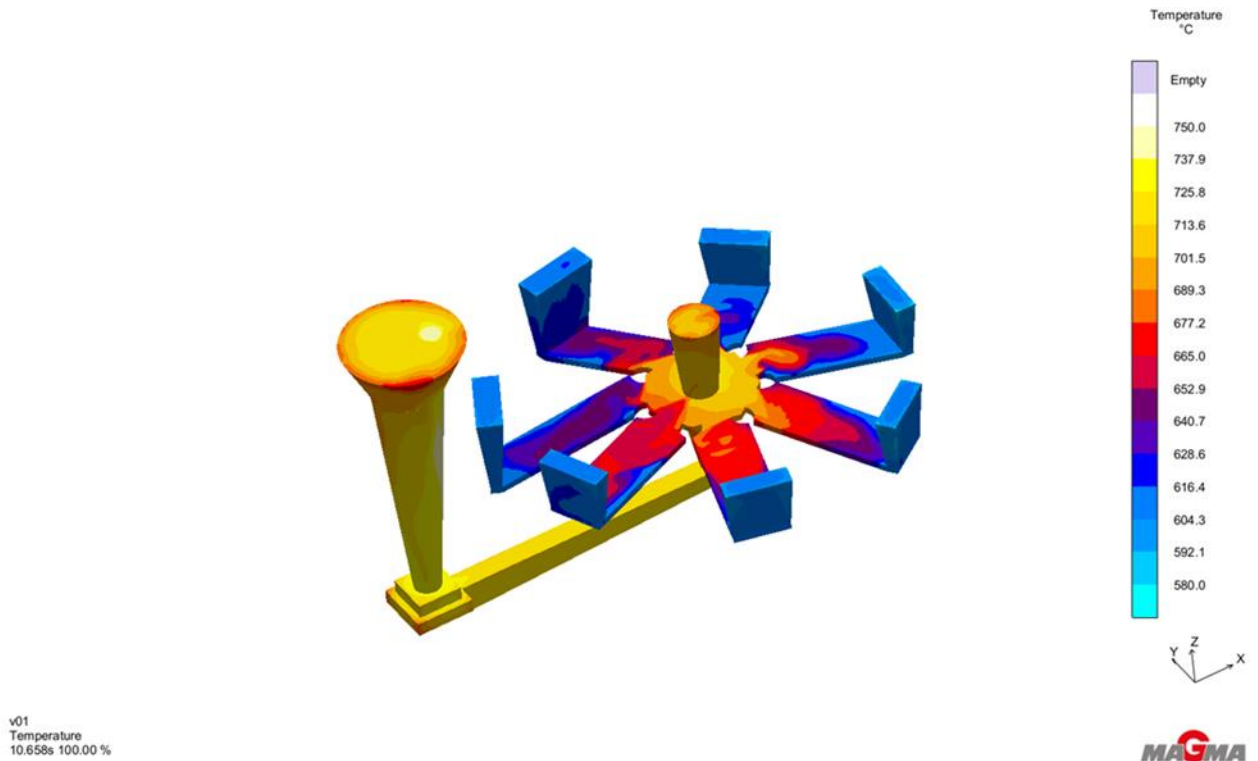
Figure 87: Pour Temperature 100% Filled on Circular Part for Fluorescent Penetrant Inspection Testing

Above is the pour temperature once the casting is 100% filled. The pour basin, sprue, filter, and runner are still high in temperature. However, the cast parts have started to cool down. The feeders have the lowest temperature since they are place the farthest

away from the flow of the molten metal and because the cavity of the part is narrow which causes the molten metal to cool down.
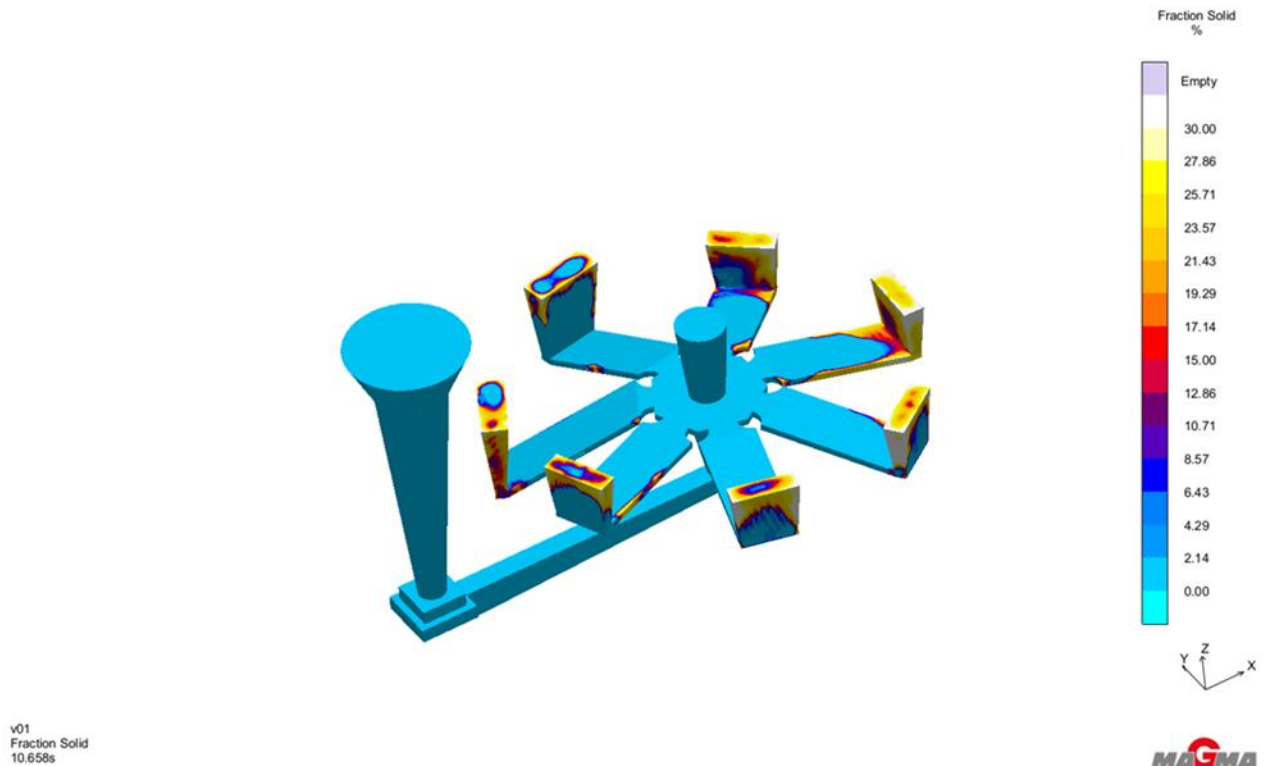
Figure 88: Pour Phase Fraction Solid at 10.658 seconds

Above in Figure 88, it can be seen the fraction solid during the pour phase. The pour took 10.658 seconds to complete. The light blue in color is all liquid. The vents and a little part of the casting have already started to solidify.

The solidification process in MAGMA is simulated to have complete solidification. This means that the casting will be completely solid and will decrease in temperature until it reaches room temperature.

However, hotspots are very important in the casting process since hotspots guarantee if the casting will completely fill without complications. The hotspots for this

casting in Figure 89 lie in the vents of the casting. Therefore, no additional change in the design is needed since MAGMA simulated a good complete pour.
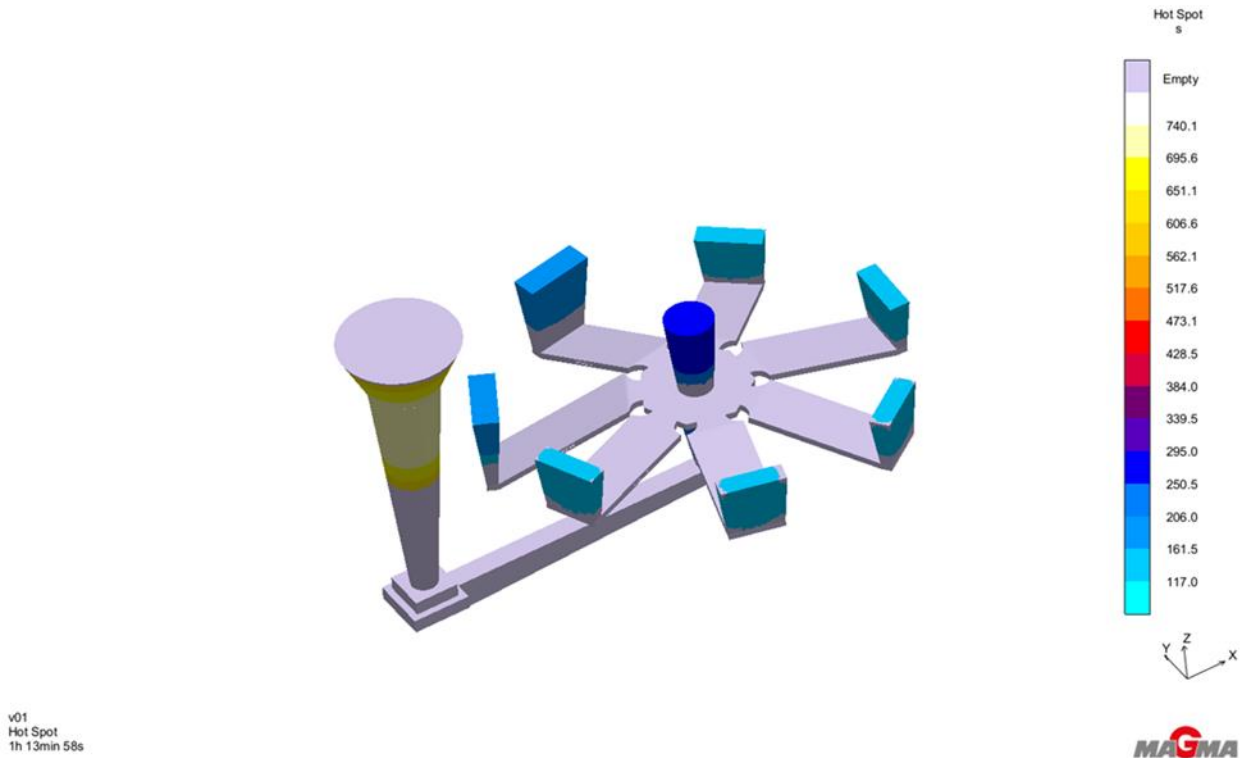
Figure 89: Hot Spots in Fluorescent Penetrant Inspection Testing Casting

After the MAGMA simulations were complete, the molds were printed at Humtown Products in Leetonia, Ohio. There were three of the same molds printed and cleaned out before shipped to Light Metals in Ravenna, Ohio to be poured using A356. Each mold contained a ceramic filter that was placed at the bottom of the sprue and inserted before the mold was assembled. This can be seen below in Figures 90 and 91.

Figure 90: Drag without Ceramic Filter

Figure 91: Drag with Ceramic Filter

During assembly of molds, it concluded that since a filter was added that the cross section of the runner was not wide enough for the molten metal to flow properly. Therefore, on one of the molds, the cross-sectional area was milled out and the filter was placed so that the molten metal could flow through the cavity without problem. This milled filter base can be seen below in Figure 92.

Figure 92: Milled Out Filter Base at Bottom of Sprue

Also, during the assembly of the molds, one of the molds did not fully fit together and left a gap between the cheek and the cope. This is an issue since during design and fabrication of the molds this gap is accounted for. This gap will cause the molten metal to seep out through the mold and if not sealed properly will cause damage. The mold was sealed with a putty so that the molten metal did not get onto the floor and didn't cause damage to the foundry or the mold itself. This can be seen below in Figure 93 and 94.

Figure 93: Mold before Seal
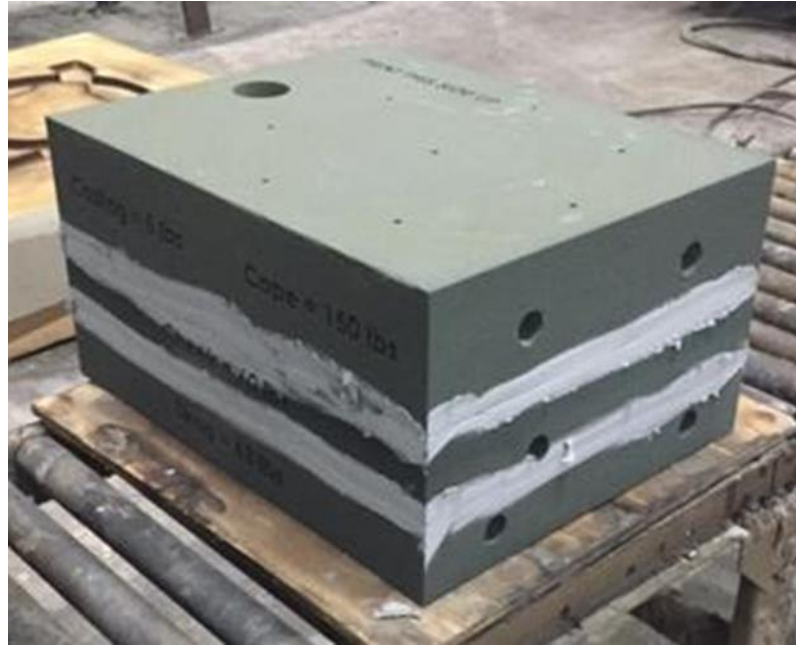
Figure 94: Mold after Seal

All three molds were then assembled. One mold was assembled correctly without any problems, the second mold contained the seal in which to help with the molten metal from spreading and the third mold contained the milled-out filter base at the bottom of the sprue. The results of each of these molds can be found below.

Figure 95: Casting that contained Mold with Seal

Above in Figure 95 it can be seen all the flash that arose around the casting. However, all the flat bar did get filled. But for this casting, more post processing is needed to remove the flash on the flat bar for the fluorescent penetrant inspection.

Below it can be seen the two different castings. The casting containing a mold that was assembled without any complications and the other casting that contained the mold that had the filter base milled out for the filter to be placed for better molten metal flow. The mold that didn't contain any change had relatively no flash around the cast part compared to the mold that had a larger opening for the molten metal to flow through. There will be less post processing of the casting with no needed assistance compared to that of the casting with the milled-out filter base. This can be seen in Figure 96.

Figure 96: Casting with No Needed Assistance and Casting with Milled Out Filter Base

As seen above in all three casting, each contain the stair step effect. This was assumed from the benchmark casting but with the fluorescent penetrant inspection testing the flat bars can be tested to determine if the stair step contains defects on the surface of the casting.

Fluorescent Penetrant Inspection (FPI) testing was conducted on the above flat A356-T6 cast bars. The group of twenty-one test specimens were broken into two groups. This was to ensure an accurate reading since time can be allotted individual to each flat bar rather than all twenty-one parts at once. The parts underwent a preclean to alleviate the parts from any debris that could still be on the cast surface. The preclean consisted of the parts being dipped in fresh acetone and then preceded to be dried off using clean, lint-free paper towels. Next, the parts were inserted into a recirculating dryer at 135 °F for five minutes to dry the parts of any unwanted acetone. Then the parts were removed from the dryer and cooled to room temperature which was roughly 105 °F.

Once the cast parts were cool to touch, they were coated with the penetrant fluid. The penetrant used in this testing was type 1, method A, sensitivity level 1, Brent P131E Penetrant which can be seen below in Figure 97 and 98.
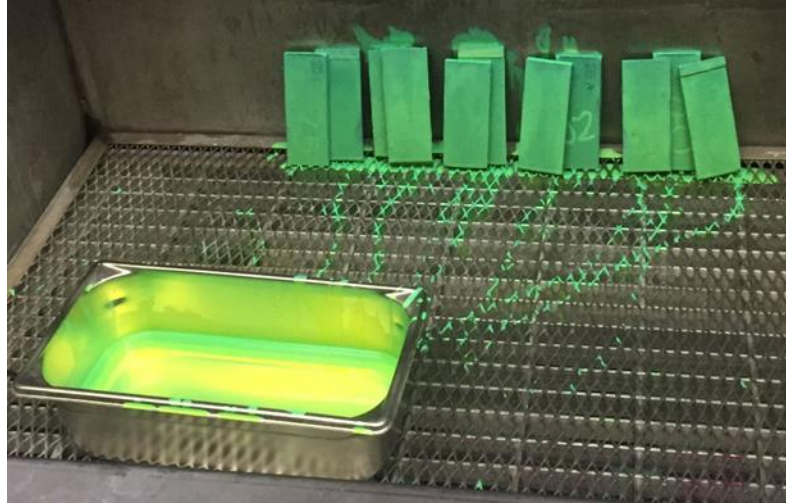
Figure 97: FPI Test Specimens under normal light
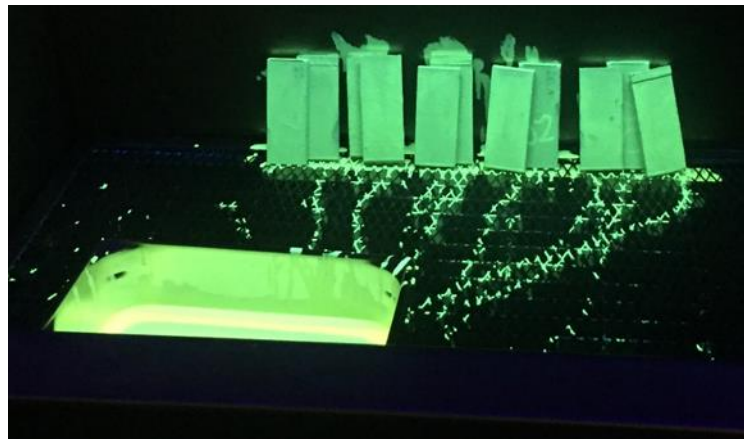
Figure 98: FPI Test Specimen under black light

Any extra penetrant was drained in a rinse station before placing the parts to dwell. A dwell time of fifteen minutes was allotted for this testing. After the fluorescent penetrant sat on the parts for fifteen minutes, it was removed using a hand-held hose that sprayed tap water at 70 °F and a pressure of 25 psi. A hand-held device was used to ensure that only the excess penetrant was removed and rinsed from the cast parts. This process was

implemented at a rinse station under a fluorescent UV lamp fixture. After the parts were rinsed, they were placed back in the recirculating dryer at 135 °F for five minutes. Once the cast parts were dry, they underwent the inspection of defects on the cast surface. The inspection was performed with REL Nomad LED UV inspection lamp and overhead Tiede Metal Halide UV flood lamps.

Below are the results of the FPI Testing.
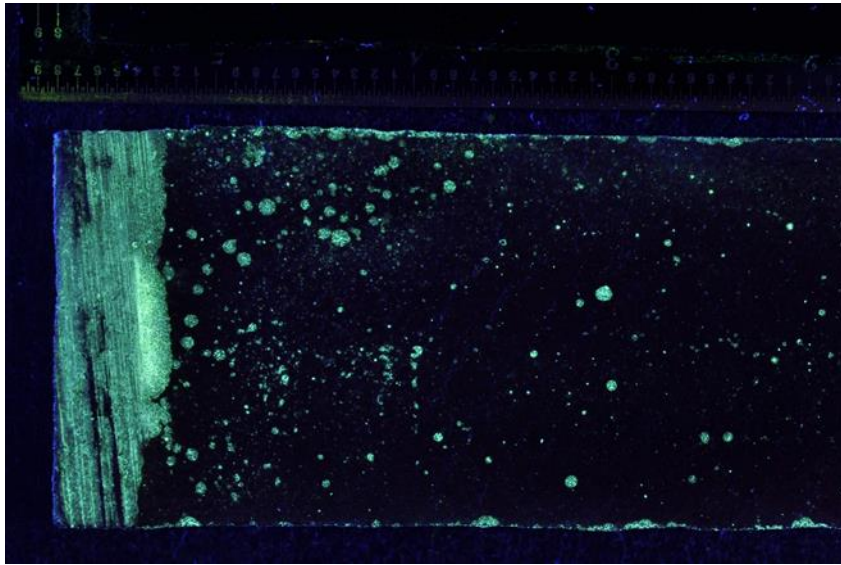
Figure 99: 0° Bottom (2) FPI Test Specimen
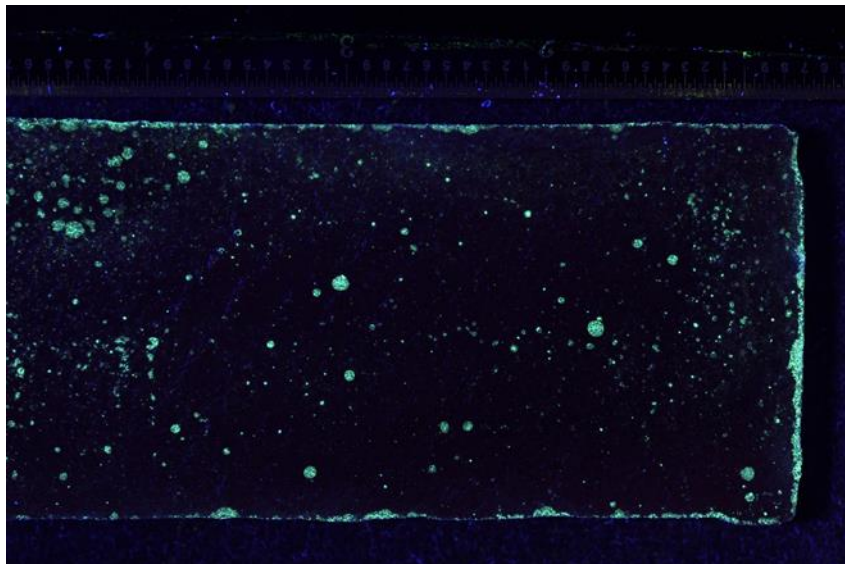
Figure 100: 0° Bottom (3) FPI Test Specimen

It can be seen above in Figures 99 and 100 the 0° FPI flat bar test specimens. In accordance with the safety specifications in the Air Force, this part would pass classes C and D. This means that it has small specs that may cause flight damage, but if it isn't used for a major part on the plane, it passes all specifications to still be used for less critical items.
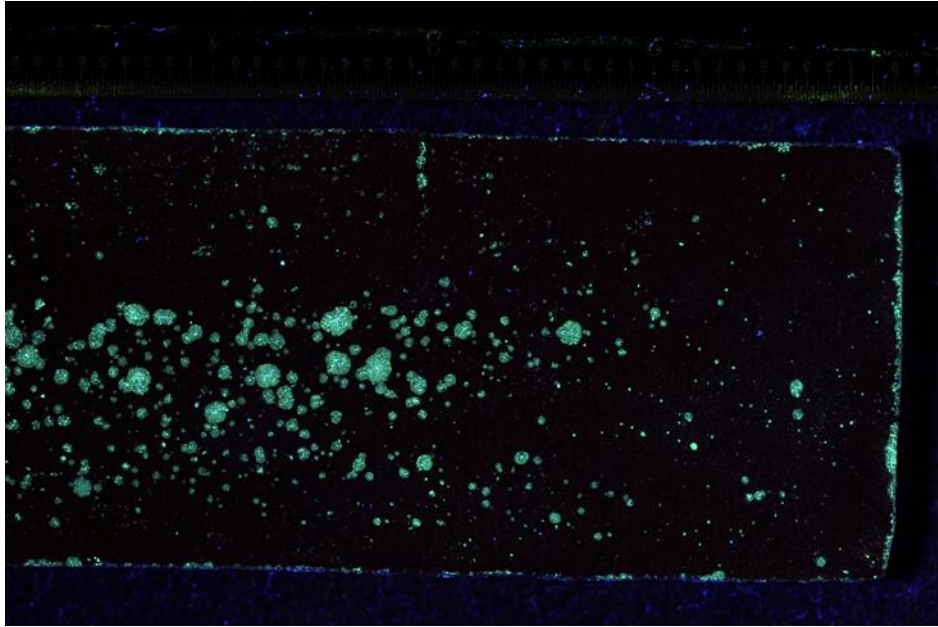
Figure 101: 15° Top (1) FPI Test Specimen
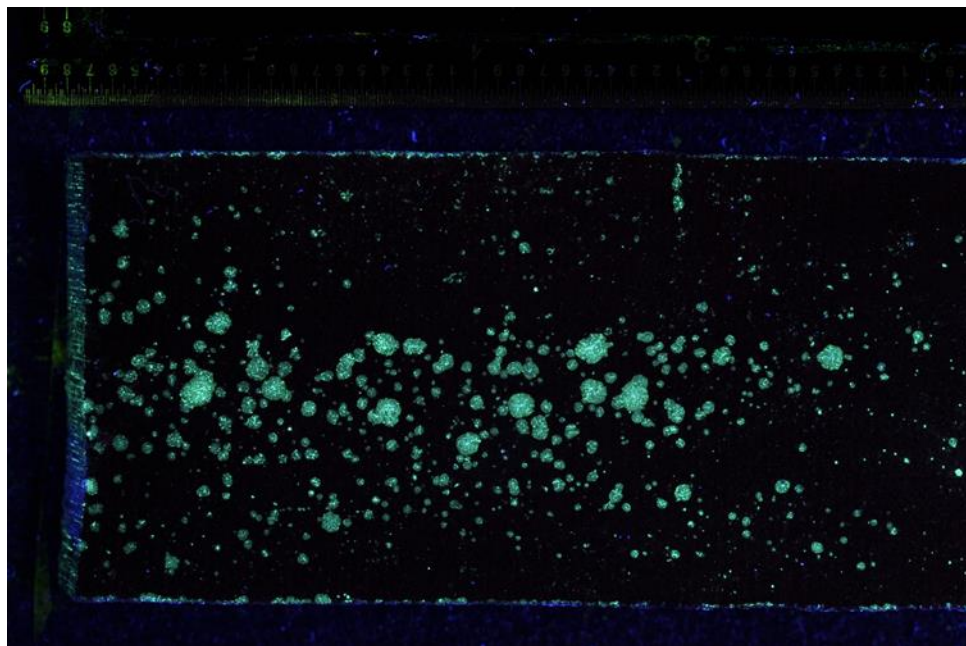
Figure 102: 15° Top (2) FPI Test Specimen

Above in Figures 101 and 102, these cast parts at 15° would not pass class C or D due to porosity proximity. The fluorescent specs are too big and they can cause fracture during flight. These parts will not be able to be on a plane due to their high stress concentration factors.
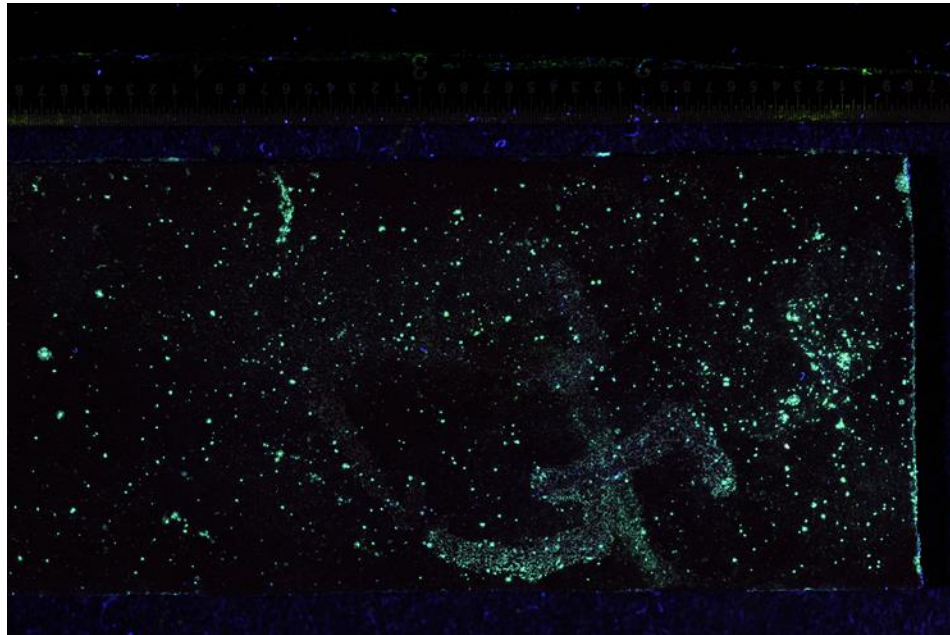
Figure 103: 25° Bottom (7) FPI Test Specimen
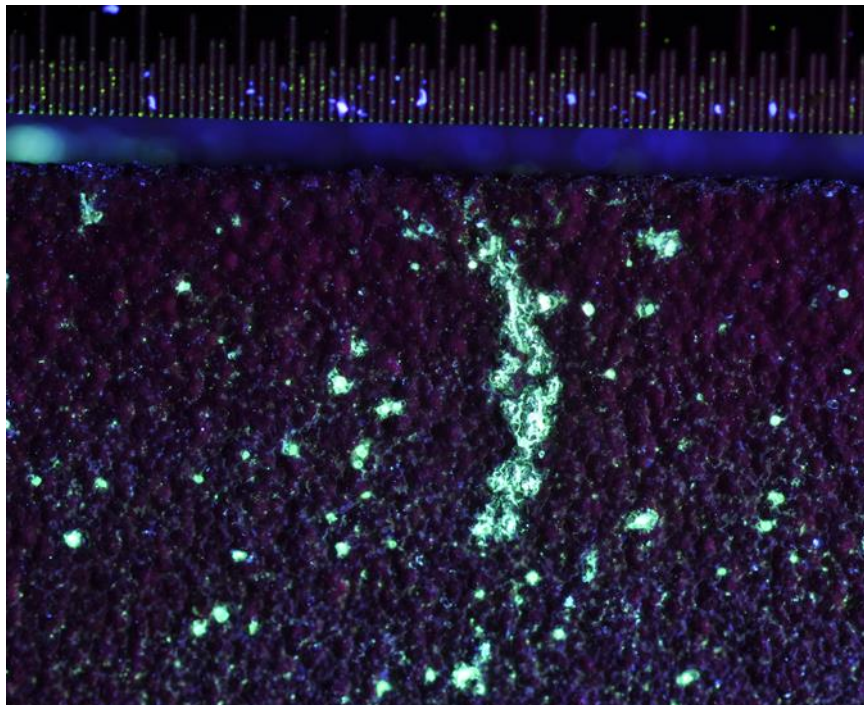
Figure 104: 25° Bottom (7) FPI Test Specimen Zoomed In

Above in Figures 103 and 104, test cast parts at 25° would not pass classes C or D due to linear indication exceeding 0.25 inches. This linear indication can initate a crack and cause failure of a part.

5.0 Conclusion

This project consists of three different phases to determine the surface quality of a cast part using an additive manufactured sand mold. The first phase was the design, manufacture, and testing of a benchmark casting. The benchmark casting consists of six print orientation angles to compare their surface roughness and surface finish. It was concluded that printing at different angles gave a stair step effect and inconsistent trends for Ra and Rq using the Keyence Microscope. The second phase of the project consisted of static tensile and fatigue testing of flat and tensile bars. A design of the casting was constructed with a gating system. This gating system was formulated using calculations to best fit the casting. A mold was designed with the cavity of the casting with gating system. MAGMA was run on the casting with the gating system included. The sand mold and vents were constructed in MAGMA. The molds were then printed out at Humtown Products in Leetonia, Ohio and poured at Light Metals in Ravenna, Ohio. Then they were sent to Westmoreland for static tensile and fatigue testing. To look closer into the stair step effect, fluorescent penetrant inspection testing was the third phase of the project. This was used to determine if the stair step effect contain any defects along the surface of a flat bar. A design with gating system and mold was constructed. These files were sent to Humtown Products to be printed and to Light Metals to be poured.

6.0 Future Work

The future work that will correlate to this project is to manufacture different sand molds with various sands to determine surface quality for comparison. These different sands will contain different GFN numbers to then be compared to these parts in this project that has a GFN number of 83.

A second part to this project is to elaborate on phase 1 with the coating on the surface to enhance the surface quality. Multiple coatings can be tested to see how they enhance the surface roughness of a cast part.

7.0 Works Cited

1. Conner BP, Manogharan GP, Martof AN, Rodomsky LM, Rodomsky CM, Jordan DC, et al. Making sense of 3-D printing: Creating a map of additive manufacturing products and services. Additive Manufacturing. 2014;1-4: 64–76.

2. 7_families_print_version.pdf. Available: https://www.additivemanufacturing.media/cdn/cms/7_families_print_version.pdf

3. Binder Jetting | Additive Manufacturing Research Group | Loughborough University [Internet]. [cited 10 Dec 2017]. Available: http://www.lboro.ac.uk/research/amrg/about/the7categoriesofadditivemanufacturing/binderjetting/

4. grain fineness number. In: TheFreeDictionary.com [Internet]. [cited 5 Mar 2018]. Available: https://encyclopedia2.thefreedictionary.com/grain+fineness+number

5. Forecast •. U. S. • State of North American Metalcasting. Available: http://www.globalcastingmagazine.com/wp-content/uploads/2013/08/IFF_2014_NorthAmerica.pdf

6. Modern Casting December 2017 [Internet]. [cited 5 Mar 2018]. Available: http://content.digitalpub.blue-soho.com/web/y5b2/0A1snzj/ModernCastingDec2017/html/index.html?page=26

7. Gating System and Types [Internet]. [cited 30 Nov 2017]. Available: http://www.themetalcasting.com/gating-system-types.html

8. Sand Casting Terminology [Internet]. [cited 19 Dec 2017]. Available: http://www.jlcastings.com/no-bake-sand-casting/sand-casting-terminology

9. Function I. The riser is a reservoir in the mold that serves as a source of liquid metal for the casting to compensate for shrinkage during solidification. The riser must be designed to freeze after the main casting in order to satisfy. Available: https://uotechnology.edu.iq/dep-materials/lecture/fourthclass/CastingTechnology03.pdf

10. Features CV. Die Cast Chill Vents. Available: https://na.dmecompany.com/MoreInformation/Catalogs/DC/ChillVents.pdf

11. Carlstedt T. Cope & Drag of a Sand Casting Pattern [Internet]. [cited 30 Nov 2017]. Available: http://info.cpm-industries.com/blog/bid/178196/Cope-Drag-of-a-Sand-Casting-Pattern

12. Sand Casting Process, Defects, Design [Internet]. [cited 30 Nov 2017]. Available: http://www.custompartnet.com/wu/SandCasting

13. 2_casting.pdf. Available:
https://www.ielm.ust.hk/dfaculty/ajay/courses/ieem215/lecs/2_casting.pdf

14. Cores' Role in Casting Design | AFS [Internet]. [cited 14 Mar 2018]. Available:
http://www.afsinc.org/content.cfm?ItemNumber=6926

15. Richards A. An overview of sand core making in casting. In: Haworth Castings
[Internet]. [cited 17 Apr 2018]. Available:
https://www.haworthcastings.co.uk/news/an-overview-of-sand-core-making-in-
casting

16. S-Max 3D Printer | ExOne [Internet]. [cited 7 Dec 2017]. Available:
http://www.exone.com/Systems/Production-Printers/S-Max

17. Aluminum Alloys. The American Foundry Society Technical Dept. 2006;
Available: http://www.afsinc.org/files/images/aluminum.pdf

18. Properties T. Density. 2.685 g/cm_ (0.097 lb/in_) at 20∘C (68∘F). Available:
http://www.hadleighcastings.com/uploads/A356.0%20Alloy%20Detail.pdf

19. Primary Metallic Crystalline Structures [Internet]. [cited 30 Nov 2017]. Available:
https://www.nde-
ed.org/EducationResources/CommunityCollege/Materials/Structure/metallic_stru
ctures.htm

20. Primary Metallic Crystalline Structures [Internet]. [cited 30 Nov 2017]. Available:
https://www.nde-
ed.org/EducationResources/CommunityCollege/Materials/Structure/metallic_stru
ctures.htm

21. Analysis of Aluminum Cast Component - Thomas Chludzinski ePortfolio
[Internet]. [cited 7 Dec 2017]. Available:
https://sites.google.com/site/thomaschludzinskiportfolio/fextural-testing-of-
composites

22. 1984_Surf_Roughness_PG.pdf. Available: http://www.mitutoyo.com/wp-
content/uploads/2012/11/1984_Surf_Roughness_PG.pdf

23. Möller H, Govender G, Stumpf WE. The T6 Heat Treatment of Semi-Solid Metal
Processed Alloy A356. The Open Materials Science Journal. 2008;2: 6–10.

24. Wang QG, Apelian D, Lados DA. Fatigue behavior of A356-T6 aluminum cast
alloys. Part I. Effect of casting defects. J Light Met. 2001;1: 73–84.

25. Tajiri A, Uematsu Y, Kakiuchi T, Tozaki Y, Suzuki Y, Afrinaldi A. Effect of
friction stir processing conditions on fatigue behavior and texture development in
A356-T6 cast aluminum alloy. Int J Fatigue. 2015;80: 192–202.

26. Zhang, Chen, Poirier. Effect of solidification cooling rate on the fatigue life of A356.2-T6 cast aluminium alloy. Fatigue Fract Eng Mater Struct. Blackwell Science Ltd; 2000;23: 417–423.

27. Tajiri A, Uematsu Y, Kakiuchi T, Suzuki Y. Fatigue crack paths and properties in A356-T6 aluminum alloy microstructurally modified by friction stir processing under different conditions. Fracture and Structural Integrity. 2015;0. doi:10.3221/IGF-ESIS.34.38

28. Avalle M, Belingardi G, Cavatorta MP, Doglione R. Casting defects and fatigue strength of a die cast aluminium alloy: a comparison between standard specimens and production components. Int J Fatigue. 2002/1;24: 1–9.

29. Yadollahi A, Shamsaei N. Additive manufacturing of fatigue resistant materials: Challenges and opportunities. Int J Fatigue. Elsevier; 2017/5;98: 14–31.

30. Wang J, Zhang Y, Sun Q, Liu S, Shi B, Lu H. Giga-fatigue life prediction of FV520B-I with surface roughness. Mater Des. 2016;89: 1028–1034.

31. Yi JZ, Lee PD, Lindley TC, Fukui T. Statistical modeling of microstructure and defect population effects on the fatigue performance of cast A356-T6 automotive components. Materials Science and Engineering: A. 2006;432: 59–68.

32. Beretta S, Romano S. A comparison of fatigue strength sensitivity to defects for materials manufactured by AM or traditional processes. Int J Fatigue. 2017/1;94, Part 2: 178–191.

33. Gao YX, Yi JZ, Lee PD, Lindley TC. The effect of porosity on the fatigue life of cast aluminium-silicon alloys.

34. Roy M, Nadot Y, Maijer DM, Benoit G. Multiaxial fatigue behaviour of A356-T6. Fatigue Fract Eng Mater Struct. Blackwell Publishing Ltd; 2012;35: 1148–1159.

35. Spangenberger AG, Lados DA. Integrated Experimental, Analytical, and Computational Design for Fatigue Crack Growth Resistance in Cast Aluminum Alloys. Procedia Engineering. 2015;133: 399–409.

36. VK-X250 Brochure.pdf.

37. VK-X100K/X200K Analysis Application Reference Manual. Keyence Corporation; 2012.

38. Durakote 4482.pdf.

39. Calculating your grain fineness number. - Free Online Library [Internet]. [cited 5 Mar 2018]. Available: https://www.thefreelibrary.com/Calculating+your+grain+fineness+number.-a0215115858

8.0 Appendix

Below in Figures 105 and 106 contain all the data extracted from the bending

fatigue testing in phase 2 of this project. Figure 107 contains all the data extracted from

the static tensile fatigue testing in phase 2 of this project.

Testlog Number	Specimen Number	Measured Width (inches)	Measured Height (inches)	Maximum Comp. Stress (MPa)	Maximum Comp. Stress (ksi)	Maximum Comp. Load (lbs)	Minimum Comp. Stress (MPa)	Minimum Comp. Stress (ksi)	Minimum Comp. Load (lbs)	Frequency	Test Machine	Cycles to Failure	Failure Location
0404PH	FAT-0 (6)	1.9560	0.2603	170	24.656	726	17	2.466	73	10	H139	360803	Test Section
0405PH	FAT-0 (7)	1.9765	0.2610	170		738			74			499959	
0406PH	FAT-0 (8)	1.9745	0.2581	170		721			72			338944	
0407PH	FAT-0 (9)	1.9880	0.2558	170		713			71			437922	
0408PH	FAT-0 (10)	1.9675	0.2625	170		743			74			310722	
Average		1.9725	0.2595			728.2000			72.8000			389670	
Standard Deviation		0.0106	0.0023			10.9800			1.1662			69471.05368	
0414PH	FAT-5 (6)	1.9900	0.2668	170		776			78			265232	
0415PH	FAT-5 (7)	1.9815	0.2718	170		802			80			234739	
0416PH	FAT-5 (8)	1.9675	0.2668	170	24.656	767	17	2.466	77	10	H139	264134	Test Section
0417PH	FAT-5 (9)	1.9800	0.2668	170		772			77			196293	
0418PH	FAT-5 (10)	1.9705	0.2692	170		782			78			306717	
Average		1.9779	0.2683			779.8000			78.0000			253423	
Standard Deviation		0.0081	0.0020			12.1392			1.0954			36626.1032	
0424PH	FAT-15 (6)	1.9765	0.2551	170		705			70			290807	
0425PH	FAT-15 (7)	1.9720	0.2600	170		708			71			212727	
0426PH	FAT-15 (8)	1.9675	0.2616	170	24.656	738	17	2.466	74	10	H139	302890	Test Section
0427PH	FAT-15 (9)	1.9660	0.2647	170		755			75			298786	
0428PH	FAT-15 (10)	1.9655	0.2508	170		677			68			437990	
Average		1.9695	0.2584			716.6000			71.6000			308640	
Standard Deviation		0.0042	0.0049			27.2367			2.5768			72634.5727	
0434PH	FAT-30 (6)	1.9745	0.2360	170		603			60			173026	
0435PH	FAT-30 (7)	1.9695	0.2268	170		555			56			262571	
0436PH	FAT-30 (8)	1.9735	0.2195	170	24.656	521	17	2.466	52	10	H139	300761	Test Section
0437PH	FAT-30 (9)	1.9775	0.2206	170		527			53			383704	
0438PH	FAT-30 (10)	1.9700	0.2231	170		537			54			211964	
Average		1.9730	0.2252			548.6000			55.0000			266405.2	
Standard Deviation		0.0030	0.0060			29.5405			2.8284			72989.7936	

Figure 105: 170 MPa Data from Fatigue Testing

114

Testlog Number	Specimen Number	Measured Width (Inches)	Measured Height (Inches)	Maximum Comp. Stress (MPa)	Maximum Comp. Stress (ksi)	Maximum Comp. Load (lbs)	Minimum Comp. Stress (MPa)	Minimum Comp. Stress (ksi)	Minimum Comp. Load (lbs)	Frequency	Test Machine	Cycles to Failure	Failure Location
0399PH	FAT-0 (1)	1.9605	0.2581	190		800	19		80			179565	
0400PH	FAT-0 (2)	1.9715	0.2668	190		859			86			159452	
0401PH	FAT-0 (3)	1.9765	0.2574	190	27.557	802		2.756	80	10	H139	159155	Test Section
0402PH	FAT-0 (4)	1.9675	0.2594	190		811			81			235447	
0403PH	FAT-0 (5)	1.9690	0.2600	190		815			82			235830	
Average		1.9690	0.2603			817.4000			81.8000			193889.8	
Standard Deviation		0.0052	0.0034			21.5277			2.2271			34881.65576	
0409PH	FAT-5 (1)	1.9810	0.2698	190		883			88			96149	
0410PH	FAT-5 (2)	1.9670	0.2682	190		866			87			122505	
0411PH	FAT-5 (3)	1.9815	0.2710	190	27.557	891	19	2.756	89	10	H139	152571	Test Section
0412PH	FAT-5 (4)	1.9845	0.2676	190		870			87			228921	
0413PH	FAT-5 (5)	1.9880	0.2830	190		975			98			105498	
Average		1.9804	0.2719			897.0000			89.8000			141128.8	
Standard Deviation		0.0072	0.0057			40.0150			4.1665			47912.3712	
0419PH	FAT-15 (1)	1.9735	0.2556	190		790			79			157089	
0420PH	FAT-15 (2)	1.9680	0.2610	190		821			82			210673	
0421PH	FAT-15 (3)	1.9690	0.2491	190	27.557	748	19	2.756	75	10	H139	207377	Test Section
0422PH	FAT-15 (4)	1.9705	0.2572	190		798			80			216389	
0423PH	FAT-15 (5)	1.9690	0.2631	190		835			83			160085	
Average		1.9700	0.2572			798.4000			79.8000			190322.6	
Standard Deviation		0.0019	0.0048			29.8704			2.7857			26089.2053	
0429PH	FAT-30 (1)	1.9700	0.2234	190		602			60			168741	
0430PH	FAT-30 (2)	1.9740	0.2234	190		603			60			168758	
0431PH	FAT-30 (3)	1.9790	0.2332	190	27.557	659	19	2.759	66	10	H139	155914	Test Section
0432PH	FAT-30 (4)	1.9945	0.2294	190		943			64			149582	
0433PG	FAT-30 (5)	1.9625	0.2203	190		583			58			175331	
Average		1.9760	0.2259			678.0000			61.6000			163665.2	
Standard Deviation		0.0107	0.0047			134.9163			2.9394			9446.7864	

Figure 106: 190 MPa Data from Fatigue Testing

115

Sample ID	Test Log Number	Temp.	UTS (ksi)	0.2% YS (ksi)	Elong (%)	Modulus	Codes	Ult. Load (lbf)	0.2% YLD. (lbf)	Orig. Width (in.)	Orig. Thick (in.)	4D Orig. GL (in.)	4D Final GL (in.)	Orig. Area (sq. in.)	Machine Number	A\U\R
TEN-0 (1)	0439PH	Room	42.1	36.3	4.0	10.0	H	2472	2133	0.2518	0.2334	1.00	1.04	0.05877012	R1	R
TEN-0 (2)	0440PH	Room	40.7	33.2	4.0	11.4		2397	1956	0.2518	0.2336	1.00	1.04	0.05882048	R1	R
TEN-0 (3)	0441PH	Room	41.6	33.0	4.0	10.9		2447	1948	0.2522	0.2331	1.00	1.04	0.05878782	R1	R
TEN-5 (1)	0442PH	Room	41.3	34.2	3.0	11.1	H	2438	2019	0.2526	0.2336	1.00	1.03	0.05900736	R1	R
TEN-5 (2)	0443PH	Room	42.5	33.0	5.0	9.9		2493	1939	0.2520	0.2330	1.00	1.05	0.05871600	R1	R
TEN-5 (3)	0444PH	Room	42.9	32.8	6.0	8.7	D	2526	1927	0.2518	0.2336	1.00	1.06	0.05882048	R1	R
TEN-15 (2)	0446PH	Room	43.0	33.1	7.0	11.0		2535	1951	0.2522	0.2336	1.00	1.07	0.05891392	R1	R
TEN-15 (3)	0447PH	Room	43.5	32.5	7.0	10.0		2558	1907	0.2520	0.2332	1.00	1.07	0.05876640	R1	R
TEN-30(1)	0448PH	Room	44.2	34.1	9.0	11.8		2593	1997	0.2522	0.2324	1.00	1.09	0.05861128	R1	R

Figure 107: Tensile Data

116